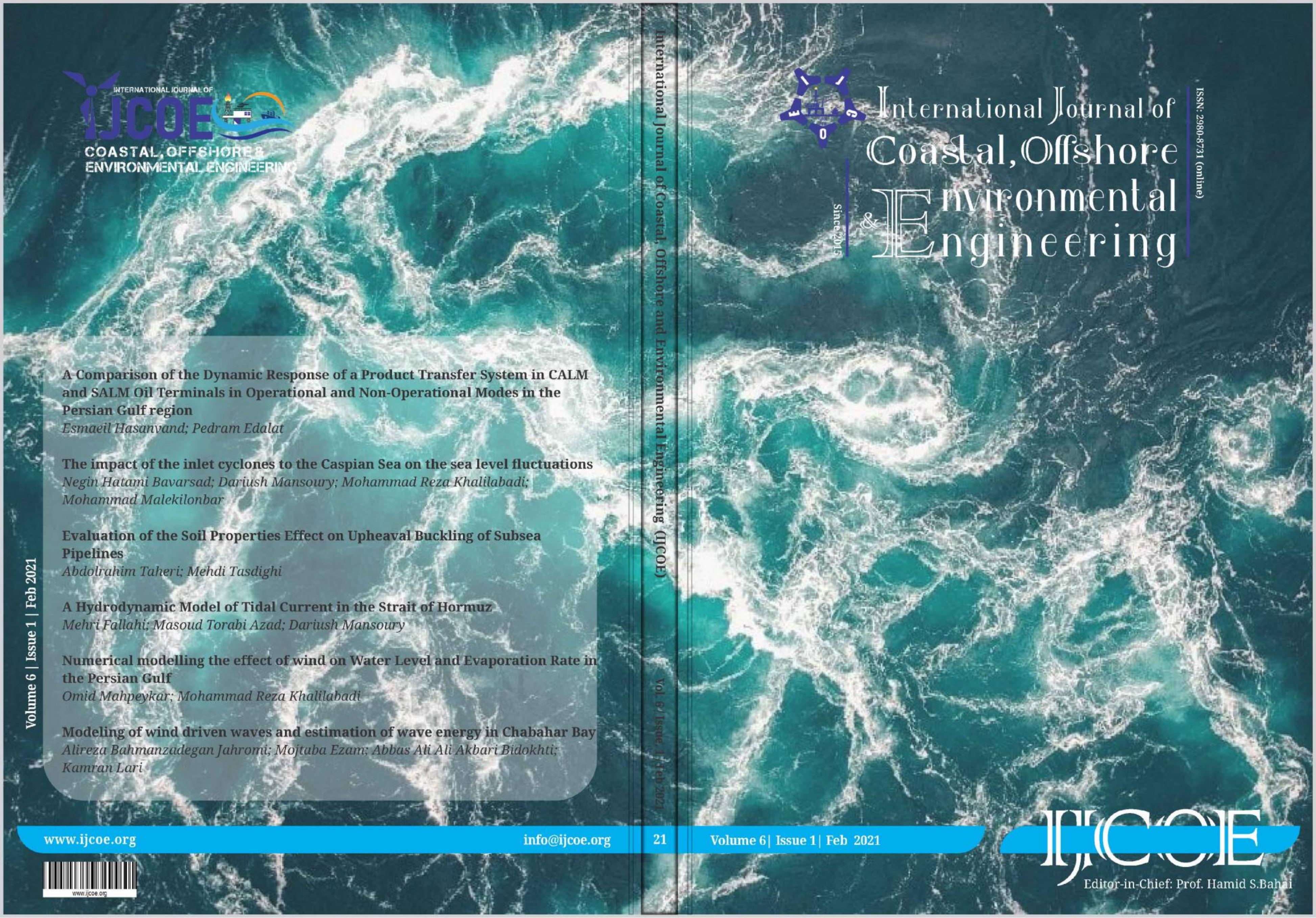

INTERNATIONAL JOURNAL OF
IJCOE
COASTAL, OFFSHORE &
ENVIRONMENTAL ENGINEERING

A Comparison of the Dynamic Response of a Product Transfer System in CALM and SALM Oil Terminals in Operational and Non-Operational Modes in the Persian Gulf region
Esmaeil Hasanvand; Pedram Edalat

The impact of the inlet cyclones to the Caspian Sea on the sea level fluctuations
Negin Hatami Bavarsad; Dariush Mansoury; Mohammad Reza Khalilabadi; Mohammad Malekilonbar

Evaluation of the Soil Properties Effect on Upheaval Buckling of Subsea Pipelines
Abdolrahim Taheri; Mehdi Tasdighi

A Hydrodynamic Model of Tidal Current in the Strait of Hormuz
Mehri Fallahi; Masoud Torabi Azad; Dariush Mansoury

Numerical modelling the effect of wind on Water Level and Evaporation Rate in the Persian Gulf
Omid Mahpeykar; Mohammad Reza Khalilabadi

Modeling of wind driven waves and estimation of wave energy in Chabahar Bay
Alireza Bahmanzadegan Jahromi; Mojtaba Ezam; Abbas Ali Ali Akbari Bidokhti; Kamran Lari

Volume 6 | Issue 1 | Feb 2021

www.ijcoe.org **info@ijcoe.org**

www.ijcoe.org

International Journal of Coastal, Offshore and Environmental Engineering (IJCOE)
Vol. 6 / Issue 1 / Feb 2021
21

ISSN: 2980-8731 (online)

Since 2015

International Journal of Coastal, Offshore & Environmental Engineering

Volume 6| Issue 1| Feb 2021

IJCOE

Editor-in-Chief: Prof. Hamid S.Bahai

International Journal of
Coastal, Offshore
& Environmental
Engineering
ISSN: 2980-8731 (online)
Since 2015

In The Name of God

Message from the Editor-in-Chief

The IJCOE journal office was established in 2015,and its first issue was published in 2016. TheIJCOE covers a wide range of research in thefields of oceanography & ocean technology, aswell as marine industries & marine engineering.The editorial board of IJCOE consists of nearly130 of the greatest scientists and researchersfrom over 30 countries worldwide, and thejournal's review board comprises 1,000 membersfrom all five continents. The membership andapplication process for joining the editorial andreview boards of this journal is ongoing. IJCOE isa research-academic quarterly journal that haspublication and distribution permissions fromthe Press Organization and permission topublish scientific-research articles from theMinistry of Science, Research, and Technology(MSRT) with an "A" rating. It also holds a "Q1"rating from the ISC institute with an impactfactor (IF) of approximately 0.43 and isconsidered a "core journal" (prestigious andoutstanding journal). IJCOE is an open-accessjournal and allows the download and receipt ofaccepted articles in full text for free. It respectsand adheres to copyright and COPE regulations.The journal's office operates 24/7, providingservices to researchers. In addition to publishinga regular quarterly journal, IJCOE has 16 specialissues on specific topics in preparation. It alsoprovides conditions for publishing specializedbooks, references, and handbooks. Moreover, itis ready to cooperate with the secretariats ofreputable international conferences to publishtheir selected and outstanding articles. IJCOEevaluates, appraises, and publishes books,articles, and the scientific achievements andfindings of esteemed researchers and scientistsworldwide who are innovating and conductingin-depth research in the "important and strategicfield of the maritime technology & Oceanengineering." It welcomes any form of jointcooperation with universities, research institutes,and related research centers at the national,regional, and international levels, and extends ahand for collaboration.

Classification of Editorial Board in IJCOE

Editor-in-Chief
Director-in-Chief
Deputy Editor
Executive Managers
English Text Editor
Technical Editor
International Editorial Board
National Editorial Board
Editorial Board Associate
Editorial Board Assistant
Guest Editorial Board
Advisory Board
Administrative Coordinator
Honorary Board Member
Methodology Advisor

Author Benefits

Open Access
Rapid Publication
Thorough Peer-Review
No Copyright Constraints
Coverage by Leading Indexing Services
Discounts On Article Processing Charges (APC)
No Space Constraints, No restriction on the maximum length of the papers, number of figures or colors

INTERNATIONAL JOURNAL OF
IJCOE
COASTAL, OFFSHORE &
ENVIRONMENTAL ENGINEERING

Aims of IJCOE

Hydrodynamics

Marine equipment

Structural mechanics

Ocean environmental predictions

Stochastic calculations Experimental

Automatic Control of Marine Systems

Scope of IJCOE

Marine Hazards

Ocean Acoustics

Naval Architecture

Ocean Engineering

Coastal Engineering

Marine Meteorology

Marine Earth Sciences

Underwater Technology

Marine Renewable Energy

Polar & Arctic Engineering

Marine Renewable Energy

Marine Geography & Geodesy

Marine Environmental Engineering

Automatic Control of Marine Systems

Hydro Physics & Physical Oceanography

Type of papers

- Case Studies
- Book Reviews
- Review Article
- Letters to the Editor
- Methodology Papers
- Editorials and Commentaries
- Response or Rejoinder Papers
- Perspective or Opinion Papers
- Conceptual or Theoretical Papers
- Meta-Analysis and Systematic Reviews
- Short Communications or Brief Reports
- Research Articles (Original Research Papers)

Scientific Research Journal

Ministry of Science, Research And Technology (MSRT)

Jurnal Ranking 2023: A

Ministry Of Science, Research And Technology (ISC)
Citation Impact 2022: 0.429
Quartile 2022 : Q1
Core Collection

IJCOE is a Member of

CIVILICA We Respect the Science
Google Scholar
Jouroscope
COPE 20TH ANNIVERSARY 1997-2017
ISC
JREF.IR Journals Reference
DOAJ DIRECTORY OF OPEN ACCESS JOURNALS
ISSN INTERNATIONAL STANDARD SERIAL NUMBER INTERNATIONAL CENTRE
Researcher.Life
doi Crossref mEDRA
iThenticate
magiran
OPEN ACCESS
pistotn
ResearchGate
Regional Information Center for Science and Technology RICEST
ScienceGate
Scilit
SID
website.informer.com
WEBrate

Cantact Us

Office 1 | Research Institute of Meteorology and Atmospheric Science
Address | Tehran, Shahid Kharrazi Highway, Pajoohesh Blvd, Research Institute of Meteorology and Atmospheric Science, Sand and Dust Storm International Research Center (SDS-IRC), No. 13, 1st floor.
Phone | +982144787652
Postal code | 13611-14977
website | www.rimac.ac.ir

Office 2 | Iranian National Institute for Oceanography and Atmospheric Science
Address | Tehran, Dr. Fatemi Gharbi St., Shahid Etemadzade St., No. 3, third floor.
Phone | +982166944873
Postal code | 13389 – 14118
website | www.inio.ac.ir

Email | Info@ijcoe.org
Website | www.ijcoe.org

Follow Us

www.ijcoe.org

INTERNATIONAL JOURNAL OF
IJCOE
COASTAL, OFFSHORE & ENVIRONMENTAL ENGINEERING

Volume & Issue:

Volume 6, Issue 1, February 2021

Number of Articles: 6

Content

INTERNATIONAL JOURNAL OF
COASTAL & OFFSHORE ENGINEERING

IJCOE Vol.6/No. 1/Winter 2021 (1-14)

Available online at: www. Ijcoe.org

A Comparison of the Dynamic Response of a Product Transfer System in CALM and SALM Oil Terminals in Operational and Non-Operational Modes in the Persian Gulf region

Esmaeil Hasanvand[1], Pedram Edalat [2*]

[1] M.Sc. Offshore Structure Engineering Department, Petroleum University of Technology, Abadan, Iran; E.hasanvand@mnc.put.ac.ir
[2*] Assistant Professor, Mechanical Engineering Department, Petroleum University of Technology, Abadan; Edalat@put.ac.ir

ARTICLE INFO

Article History:
Received: 07 Dec. 2020
Accepted: 24 Feb. 2021

Keywords:
Offshore oil terminal
CALM
SALM
dynamic analysis
Flexible pipeline

ABSTRACT

Offshore oil terminals are a cheaper and safer solution than conventional shore terminals for unloading and loading tankers. There are several types of offshore terminals, including Catenary Anchor Leg Mooring (CALM) and Single Anchor Leg Mooring (SALM). Product transfer systems, including floating and underwater pipes, are the most important components of these terminals. The present study aims to compare the dynamic response of a product transfer system in these two models of offshore oil terminals. To obtain structural responses, including forces created in floating and underwater pipes, a simulation in Orcaflex software is used considering wind, current, and wave forces in different sea states. The curvature and tension in the pipes are considered a criterion for evaluating the failure modes. The results show that under operating conditions, the curvature and effective tension of the pipes in the SALM terminal are 5% and 93% lower than those in similar operating and environmental conditions in the CALM terminal, respectively. As the environmental conditions increase up to Sea State 8, when the tanker is not connected to the terminal, the SALM terminal pipes will have more structural stability and usability, while the CALM terminal pipes will only have stability up to Sea State 6. The tensions generated in the pipeline end manifold (PLEM) of the SALM terminal are also lower than those in the CALM terminal. It is also observed that the critical point for the CALM terminal pipes is the connection point to the terminal buoy, while it is the connection point to the seabed for SALM terminal pipes, which should be considered in designing a product transfer system for this type of terminals.

1. Introduction

One of the most important components of the production and supply chain of hydrocarbon products in the oil industry is the transfer of these products. This type of transfer is generally performed by two pipelines to the consumption points, as well as by oil terminals and loading tankers (Shuttle Tankers). Oil terminals are also divided into shore and offshore groups[1]. In shore oil terminals, the tanker must be moored at the shore for loading and unloading operations. However, in offshore terminals, petroleum products are transported to a safe area far from the shore using pipelines, and after transferring these products to offshore terminals, the tanker is loaded. So, this system does not need complex mooring compared to the shore terminals. Therefore, the tendency has increased towards the use of offshore terminals due to the high costs of the construction and maintenance of shore terminals, including dredging operations, on the one hand and the risks of unloading and loading operations (due to the possibility of the proximity of these terminals with industrial centers or some residential on the beach) on the other hand. The use of offshore terminals with the possibility of unloading and loading oil tanker in places far from the shore and close to the oil field will reduce the cost of piping at sea over long distances. It will also be safer as the high-risk operations of transporting petroleum products to tankers are transferred to points far from the shoreline, residential areas, and facilities located on the shore.

Offshore oil terminals are divided into different types according to how the tanker is controlled and how petroleum products are transferred, so choosing the best option for these types of oil terminals should be commensurate with the water depth, tanker dimensions and tonnage, the product to be transferred, dynamic interaction behavior of buoy and tanker, and other operational considerations. This paper investigates two common types of these terminals, including CALM and SALM. One of the most important parts of these terminals is the transmission system, which is responsible for transporting the product from the seabed to the tanker and must be designed in such a way that the transfer is provided safely and in accordance with the rule. Therefore, recognizing the effective parameters and examining the intensity of their impact on the transmission system is of particular importance in the study and design of these two common offshore terminals. Investigating and comparing the structural response of product transfer systems in these terminals is one of the most important criteria for selecting the appropriate type of oil terminal.

Several research studies have been done to investigate the product transfer system in oil terminals. The first flexible pipes (Known as hoses) for oil terminal were used in Libya in 1969. Accordingly, researchers began to study the behavior of hose systems. The hose of CALM oil terminals was studied by Ziccardi [2]. In this study, two riser configuration models including Chinese lantern and Lazy-S configuration were investigated. Brady and et al. examined the forces generated in the hoses using a statistical method that led to the further study of the hoses connected to the CALM terminal in the following years [3]. In 2013, Eiken addressed different configurations of underwater cravings (Lazy-S and free-hanging) with different diameters and showed what criteria and challenges should be met in designing these structures [4]. Qi and et al. examined the skirt (bottom of the terminal) of a CALM structure and performed a feasibility study on a riser with a Chinese lantern configuration. They showed that by increasing the diameter of this body, the mass was increased in the direction of heave and roll, which reduced the displacement of the structure in the heave direction. The feasibility of using this type of riser configuration for specific areas of the installation of this terminal has also been subject to studies[5]. Amaechi and et al. explored the resistance of a CALM riser with a Chinese lantern configuration connected to a tanker under different environmental conditions. In this study, Ansys Aqwa software was used for the hydrodynamic analysis of the CALM buoy, and Orcaflex software was used for the analysis of the riser. The study aimed to determine the effect of flow angle parameters on the behavior of the riser structures, such as curvature, effective tension, and bending moment[6]. The interaction between the mooring system and the riser in vessels is an important parameter that has been subject to extensive research in recent years[7]–[9]. Karegar explored different types of flexible riser configurations for shallow water. Dynamic modeling and analysis were performed using the OrcaFlex software package to obtain the structural responses The paper enumerates the main challenges for shallow water with harsh environments for flexible ridges, including MBR, large vessel offset, clearance, and Marin growth [10]. In 2014, Pecher examined two types of mooring system configurations, including CALM and SALM connected to a wave energy converter and studied the effect of stiffness and size of mooring lines on the displacement of the structure, as well as the effect on the tension of these mooring lines [11].

According to previous studies, the amount of tension and bending force in these systems is one of the most important criteria for examining and comparing different cases. Since the main component of oil terminals is the product transfer system, the comparison of these systems helps in choosing the right oil terminal. This study models the floating and underwater hoses of two terminals including the CALM and SALM with relevant specifications under the environmental conditions of the Persian Gulf and compares their responses. Also, to check the stability of these systems, they are examined with increasing environmental conditions when the tanker is not connected. Also, according to previous studies, the product transfer system of these terminals has not been examined for general analysis under real operating conditions.

1.1 Transfer product system in CALM and SALM oil terminals

One of the most common types of offshore terminals is the CALM structure, which consists of a cylindrical body connected to the seabed by 4 to 6 mooring lines. This buoy consists of two parts, an upper and a lower part. The lower part is in the water. The buoyancy of the buoy is created by the buoyant force on this part, which is restrained to the seabed by a mooring line. The upper part of the buoy is connected to the lower part by a bearing system, which allows 360-degree rotation. The tanker is connected to the top of the buoy with a hawser, which allows the tanker to rotate. This type of terminal whose application dates back to 1959 is the most commonly used system for the transfer of oil products compared to other offshore terminals.

According to Figure 1, to transfer the product from the seabed to the tankers in this system, the products are first transferred to a buoy by underwater pipes. Then, floating pipes are used to transfer them to the tanker. The underwater pipes in this type of terminal are the boundary between PLEM on the seabed and the hang-off point in the buoy, which are divided into three configurations, including a Chinese lantern, lazy S, and steep S. In these configurations, buoyancy modules are used to gain the appropriate shape. The floating pipes are connected to the underwater pipes using a SWIVEL system located in the buoy. The SWIVEL system allows these pipes to rotate relative to each other. Before unloading and loading, the floating pipes are afloat on the surface of the water, but then after the tanker is moored, the end of these pipes is connected to the tanker manifold by a crane. The floating pipes and underwater pipes are made of smaller parts, which are usually made in lengths of 9.1 meters, 10.7 meters, and 12.2 meters. So, these smaller parts are connected to each other to get the required length.

The SALM structure is connected to the seabed only by one mooring line as shown in Figure 1. Due to the universal connections in the mooring line of this structure, the tanker can rotate 360 degrees around this buoy. When the hawser (the connection cable between the tanker and the buoy) is under high stress, the buoy can go underwater or when it hits the tanker, it can go under the tanker without any problem. One or two hawsers are used to connect the tanker to the terminal, and unlike the previous structure in which petroleum products are transported from the seabed first to the terminal and then to the tanker, in this case, the products are directly transferred from the seabed to the tanker. One of the most important components of this structure is the swivel system located on the seabed. Due to the fact that the swivel system of the SALM terminal is located on the seabed, less force is applied to it than the swivel terminal CALM, which is located inside the buoy and on the surface of the water. The SALM terminal was first used in 1969 and is the second most used system after CALM in the transport of petroleum products from the seabed to tankers in offshore operations.

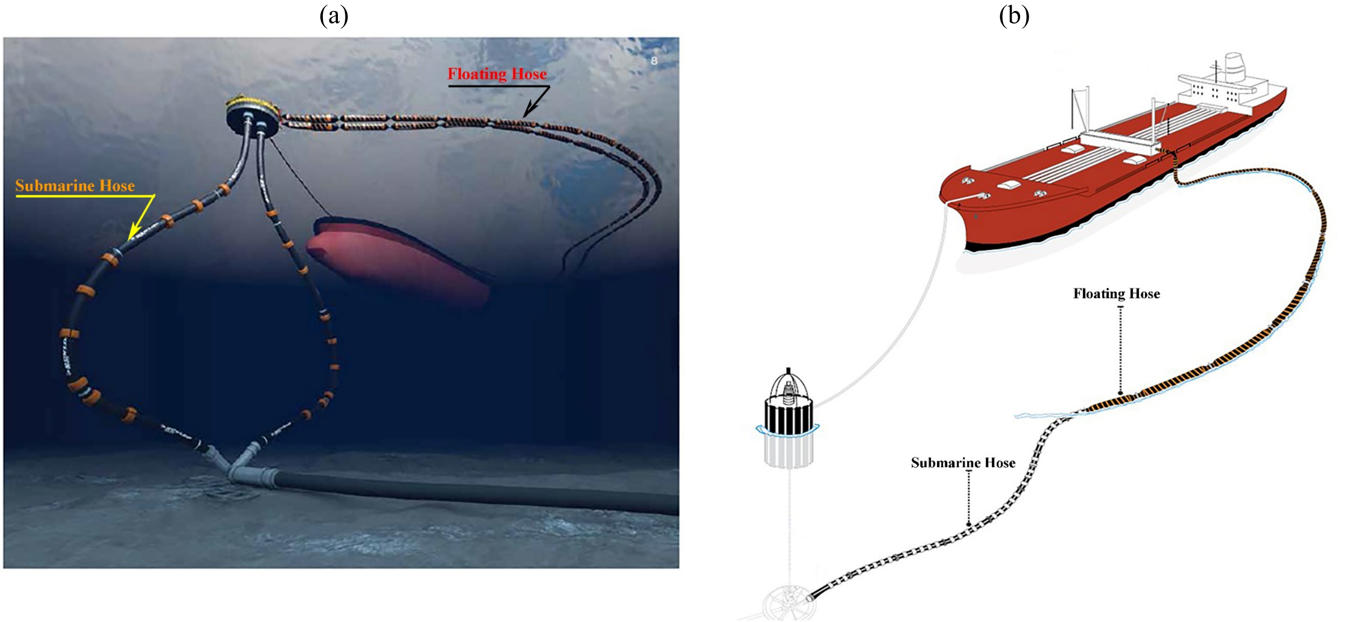

Figure 1. A schematic view of the product transfer;
(a): SALM terminal, (b): CALM Terminal

1.2 Hose material

Flexible pipes generally combine low bending stiffness with high axial stiffness, which is achieved by making the pipe in different layers. Flexible pipes are composed of different layers. Each of these layers is responsible for withstanding a specific force (tension, bending, torsion, etc.). The connection of these layers by a vulcanization process to form a single pipe is basically called a hose or bonded pipe and is used in oil terminals as shown in Fig. 2. The other alternative is the Unbonded pipe, which is used to transfer the product in structures such as FSU, FPSO, etc.

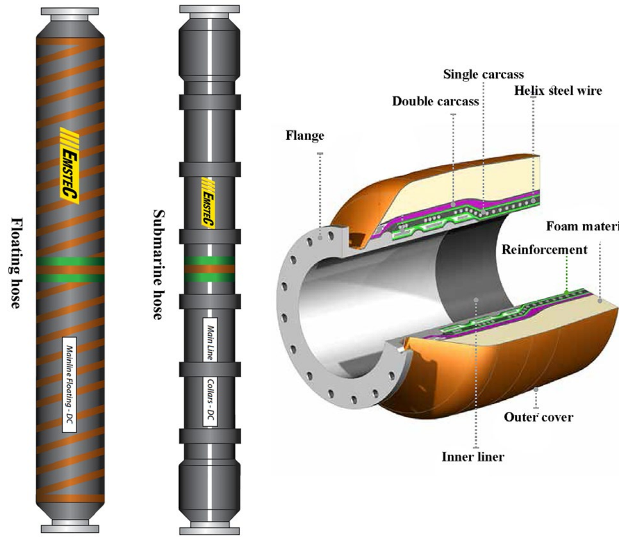

Figure 2. Double carcass hose dimensions and main components.

Hoses are essentially made in lengths of 9.1, 10.7, and 12.2 meters, which should be connected to each other to achieve the required length. The two ends of a hose have a flange in that the different pipes are connected to each other by stud bolts and nuts. The innermost part of the pipe is made of NBR rubber, which is responsible for sealing and tightens the flanges to the pipe. Reinforcement is made of polyester and withstand the internal pressure of the pipe as well as excessive loads and stresses and are adjusted according to operating and environmental conditions. For better environmental conditions and better resistance to effective tension, high external pressure, or severe bending anchors, helix steel wire reinforcement is incorporated in the hose body structure. The carcass is an interconnected metal layer that provides resistance to pipe collapse. The double carcass is used for situations that require high burst resistance. Figure 3 shows a schematic view of this flexible pipe layer.

2. Numerical modelling

To investigate the dynamic response of the product transfer system in oil terminals under the operating conditions of unloading and loading, as well as the environmental conditions, the numerical model of the terminal structure in interaction with the tanker was used in Ansys Aqwa and OrcaFlex software packages. The modeling process is presented in Figure 4. According to this process, the geometry of the terminal and the tanker connected to it should be first simulated in Ansys Aqwa software and then, the outputs should be fed into Orcaflex software to analyze the interaction of the terminal and the tankers in real operating conditions.

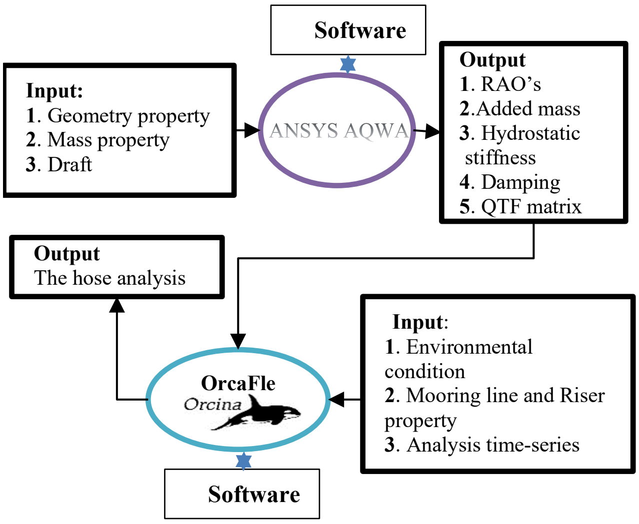

Figure 3. The designing process in the software.

As shown in Figure 4, the inputs of Ansys Aqwa include water depth and the geometrical specifications, mass characteristics, and draft of the terminal and the tanker. The outputs include RAO, mass matrix, Hydrostatic stiffness matrix, Damping and QTF matrix in each vessel. These outputs are transferred to Orcaflex software. The structural responses of each structure are calculated by creating coupled models from each terminal as a connection to the tanker and according to the type of mooring system and environmental conditions. The equation of motion of each object on the horizontal plane is described in Equation 1.

$$[M]\{\ddot{X}\}+[C]\{\dot{X}\}+[K]\{X\}=\{F(t)\} \tag{1}$$

in which [M], [C] and [K] are the mass, damping, and stiffness matrices, respectively, {X} is the displacement vector, and F(t) is the force vector. The mass of the structure is assumed to be concentrated in any degree of freedom. The added mass due to the water surrounding the structural components is also considered to be Ma.

2.1 Finite Element Model

The finite element model in Orcaflex software [12] includes parameter modeling of pipe, mooring line, and vessel. OrcaFlex analyzes structures statically and dynamically including boundary conditions such as buoy, vessels, etc., and models the finite elements of lines. In this software, mooring lines and pipes are specified as lines. As shown in Figure 4 Orcaflex uses a finite element model for the lines. The lines are divided into a set of segments that are bounded by straight massless segments at each end of the node. The segment model only models the axial and torsional properties of the line. Other properties (mass, weight, buoyancy, etc.) are all focused on the nodes.

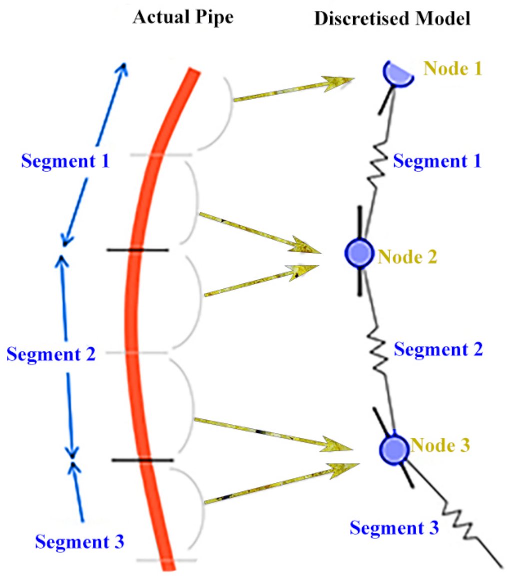

Figure 4. The OrcaFlex line element.

Models built in Orcaflex software for SALM and CALM are shown in Figure 5.

3. Case Study

3.1 Buoys

Geometric characteristics and effective parameters used in modeling the studied floating oil terminals and tankers in this paper are presented in Tables 1 and 2. The modeling process of these vessels, as shown in the flowchart diagram of Figure 1, begins with the mass, geometric and water characteristics of each vessel in ANSYS AQWA software, and the results of this analysis include the characteristics of static response and the dynamics of floating structures that are introduced in Orcaflex software as rigid body characteristics with six degrees of freedom as a terminal and tanker floating model. To compare the effect of offshore terminal type on the response of transport system structures, the paper calculates the characteristics of the CALM structure according to the actual sample of the terminal built in the Persian Gulf and the characteristics of SALM structure according to the structure built in the Gulf of Mexico for the highest tonnage of the tanker connected to it. The metacentric height is considered a criterion for evaluating the stability of the modeled buoys. For all these buoys, this parameter is greater than one, so both terminals will be stable. The buoy of the CALM terminal is composed of two components connected by a joint so that if the tanker rotates, the upper part of the terminal also rotates. A schematic view of the buoys is shown in Figure 6.

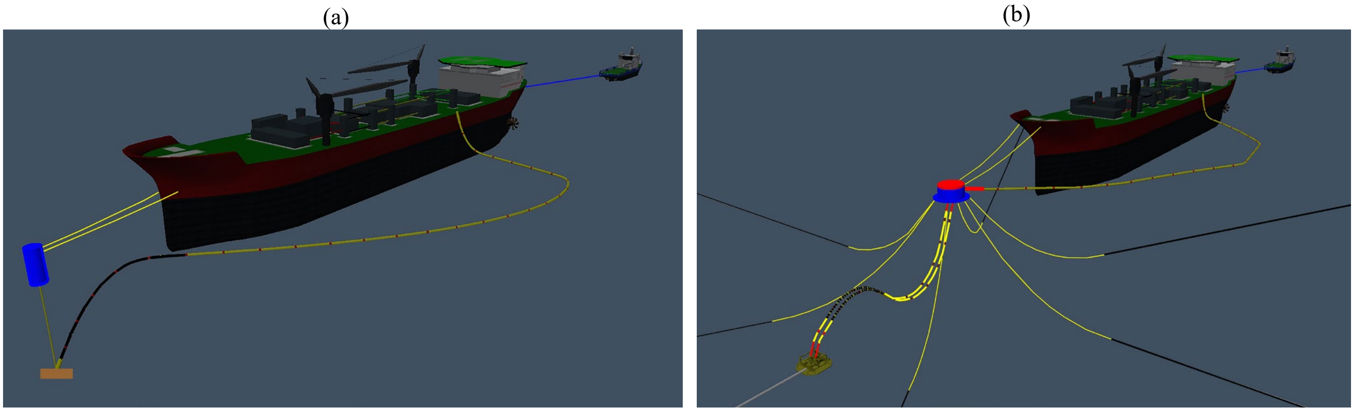
(a)
(b)

Figure 5. Modeling oil terminals in Orcaflex software; (a): SALM system, (b): CALM system

Table1. Specifications the vessels modelled in the study.

Parameters	**Unit**	**CALM**	**SALM**	**Tanker**
			Value	
Draft	m	3.266	9	22.6
Center of gravity (X-direction)	m	0	0	170.18
Center of gravity (Y-direction)	m	0	0	0
Center of gravity (Z-direction)	m	-0.766	6	17.3
Moment of inertia(X-direction)	$kg \cdot m2$	4840000	6244000	8.260E+10
Moment of inertia(X-direction)	$kg \cdot m2$	4840000	6244000	2.35E+12
Moment of inertia(X-direction)	$kg \cdot m2$	9350000	2890000	2.35E+12
Diameter	m	12.5	6.4	
Diameter of skirt	m	16.63	-	
Weight	ton	289.98	400	
Height	m	5.3	14	
Length between perpendicular, L_{BP}	[m]	-		320
Breadth molded, B	[m]	-		60
Depth, D	[m]	-		30.5
Windage area, A_L (longitudinal),surge area	[m^2]	29.53	32	1155.25
Windage area, A_T (Transverse),sway area	[m^2]	29.53	32	3693.81
Windage area, A_T*L_{BP},yaw area	[m^3]	369.12	204.8	1.182E6
Displacement	[kg]	-		3.6712E+08

3.2 Mooring line

To moor the buoy of the CALM terminal on the seabed, six moorings made of studless chains are modeled as linear elastics and their bending and torsional effects are assumed to be negligible. Each of these chains with a length of 380 meters is placed in a circular position on the periphery of the sea. The C_d and C_M coefficients are considered constant for all mooring lines during analysis and the amount of pretension in each morning is equal. In the SALM terminal, a stud mooring is used to control the buoy. This type of structure also makes the buoy rotatable due to the type of chain connections, which is a universal connection. To simulate this feature in Orcaflex software for two ends of the mooring, one in the seabed and the other connected to the buoy, zero bending stiffness and torsion are considered which allows free rotation at both ends of the mooring. General specifications and parameters required for the modeling of the mooring are given in Table 2.

Table 2. Specifications of the mooring line.

Parameters	**Unit**	**Value**	
		CALM	**SALM**
Diameter	**mm**	95	175
Length	**m**	380	38.8
Weight	**Kg/m**	180	671
Axial stiffness	**kN**	712000	3093000
Minimum breaking load	**kN**	8180	25173
C_d	**-**	1.2	1.2
C_M	**-**	1	1

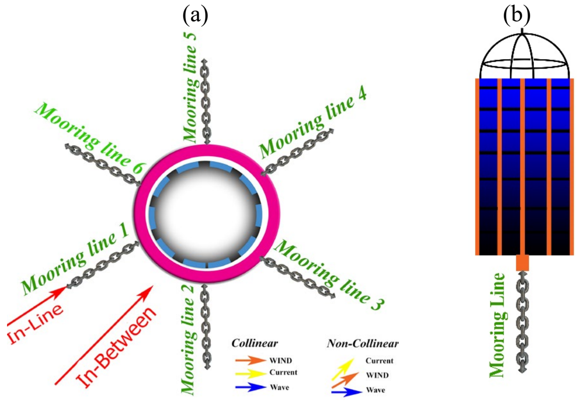

Figure 6. The arrangement of the mooring line; (a): CALM system, (b): SALM system

In this study, to connect the tanker to the terminal, two hawsers have been used for each terminal buoy, which is nonlinearly modeled in Figure 7. The length of these hawsers is 60.96 m and their maximum allowable tension (MBL) is 5800 kN

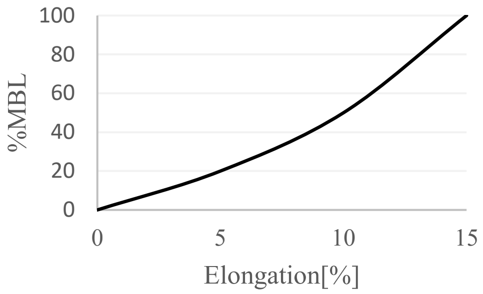

Figure 7. The non-linear axial stiffness in the hawser system.

3.3 Hose

In the CALM terminal, underwater hoses are created in the Lazy S configuration, as shown in Figure 8. These hoses are 117.7 m long, which are created by 11 parts of a 10.7 m hose section. The upper end of the pipe is fixed to the lower part of the buoy, and the lower end of the pipe is fixed to the seabed at a certain angle to the horizon. Bending stiffeners are used at both ends due to the high bending force that is created. Since both ends of each part have a flange made of steel, in models, both ends of the pipe section are assumed to be made of flanges made of steel according to the profile shown in Figure 4. To obtain the desired configuration shape, buoyancy modules are used along the length. The floating pipes in this terminal are modeled with 23 pipe sections with flanges at each end. One end of the pipe is connected to the tanker at a height of 15 m above the sea level, and the other end to the revolving part of the terminal (upper part of buoy).

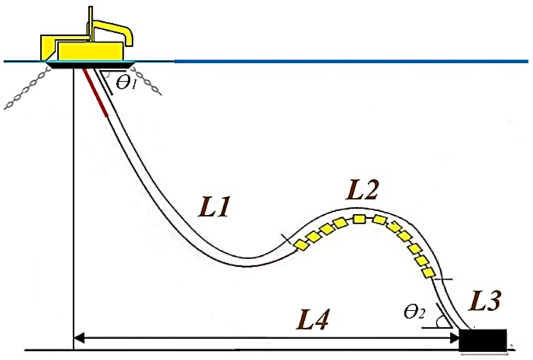

Figure 8. Submarine Hose Design Parameter.

The boundary conditions for the pipes used in the SALM terminal are such that the end connected to the seabed must rotate freely and the other end is fixed connected to the tanker. The pipe used consists of two parts, floating and underwater, which are connected to each other, each with a length of 362 meters, creating an integrated pipe. A buoyancy module is used to create a proper riser configuration. The specifications required for the design of floating and submarine pipes for each terminal are given in Table 3.

3.4 Loading

The first step in the analysis and design process is to determine the load and forces on the structures under study. The forces acting on these structures include forces from waves, winds, and currents. The combination of these forces also has a significant impact on the total incoming forces. Due to the wave phenomenon, two important forces of drag and inertia are created on the structure so that all the forces created by the wave are the result of these two forces. The drag force of F_D is affected by the velocity of the fluid, which depends on the shape and roughness of the body, the Reynolds number, and the intensity of the turbulence in the flow. The inertial force F_I is caused by the acceleration of the fluid particles (water). Due to the windage surface of the upper part of the tanker, the wind force is of great importance. This force is due to the change in pressure created in the free wind flow and is a function of wind speed, direction, surface, and shape of structural members. The current force also increases the drag and lifts force in the submerged parts of the structures, which is able to change the wave height and period in interaction with the wave(DNV-RP-C205, 2010).

Table 3. The physical and mechanical properties of the hose.

ITEM	**Transfer system for CALM terminal**		**Transfer system for SALM terminal**	
	Submarine hose	**Floating hose**	**Submarine hose**	**Floating hose**
Section length [m]	10.7	12.2	12.2	12.2
Inner diameter [mm]	500	0.609	609	609
Total length L [m]	118	298	48.8	314
Outside diameter [mm]	620	1117	1117	1117
Bend stiffness [kNm^2]	158	300	500	300
Tension stiffness [kN]	4325.866	4325.866	4325.866	4325.866
Weight (empty)[kg/m]	434	600	439	600
Minimum breaking tension [kN]	810	810	810	810
Fluid density [kg/m3]	725	725	725	725
Drag force coefficient, C_d	0.9	0.9	0.9	0.9
Added mass coefficient C_m	1	1	1	1
Water depth, [m]	47.8	47.8	47.8	47.8
MBR	4*ID	6*ID	4*ID	6*ID

Wave Load

Morrison equation is used to calculate the wave force in slender components, such as mooring and risers, and diffraction theory is used for components whose body dimensions are larger than the wavelength, such as buoys. The transverse and rotational displacements in the vessel are calculated by RAO using Equation 2 for each wave height and period[14].

$$X = A . RAO . \cos(\omega t + \psi) \qquad (2)$$

in which X is the response of the structure, A is the amplitude of the wave, and Ψ and ω are the angle of the frequency flow and the frequency of the wave, respectively. Given the research site, the wave spectrum used in this study is the modified Jonswap spectrum which is appropriate to the environmental conditions of the Persian Gulf. It is presented in Equation 3, (DNV-OS-E301, 2010).

$$S(\omega)=\frac{\alpha g^{2}\gamma^{\alpha}}{\omega^{5}}\exp\left(-\frac{5}{4}\frac{\omega_p^{4}}{\omega^{4}}\right) \qquad (3)$$

in which g is a gravitational constant, and the key parameters for defining this spectrum include the characteristic wave height Hs, spectral peak period, Tp, and the peak enhancement factor γ, which are presented in Table 5 for this study. To compare three terminals in the same conditions, a wave direction of 30 degrees relative to the direction of the tanker is considered.

Wind and Current

In addition to the force on the structure due to the wave phenomenon, the forces arising from the two phenomena of wind and current are also of special importance. The parameters used to calculate wind force and current are presented in Table 5. The direction of wind force and current parallel to the wave force used in calculating the most critical displacement of the tanker connected to the terminal is considered as per the profile of two wind forces and constant current in accordance with the OCIMF regulations[16].

This paper considers the environmental conditions including wave, current, and wind in accordance with the operating conditions of the Persian Gulf as expressed in Table 4 to investigate the dynamic behavior of floating structures and their impact on the pipe system. In all conditions, wind, wave, and current directions are considered to compare the response of these terminals.

Table 4. Environmental conditions.

Parameter				**value**	**unit**
Wave	JONSWAP	Operation	H_s	2.6	[m]
			T_p	7.5	[s]
			γ	1.4933	-
		Survival	H_s	3.9	[m]
			T_p	8.5	[s]
			γ	2.2261	-
Wind	Constant velocity	Operation		22	[m/s]
		Survival		26	[m/s]
	Air density			1.28	[kg/m^3]
Current	Triangular profile	Operation	surface	0.7	[m/s]
			seabed	0	[m/s]
		Survival	surface	0.8	[m/s]
			seabed	0	[m/s]
Sea	Water depth			47.8	[m]
	Water density			1025	[kg/m^3]

In order to evaluate the stability of floating and underwater desires hoses against the applied forces when the tanker is not connected and no operation is performed, in addition to the operating conditions of the Persian Gulf, four other environmental conditions are considered according to Table 5. These environmental conditions include waves with a characteristic height of 2 to 5.5 meters.

Table 5. Different types of sea states.

Sea state *i*	**H_s**	**T_p**	**γ**	**Wind velocity[m/s]**
Sea State 5	2	5.5	1.4933	10.28
Sea State 6	3	7	1.4933	13.37
Sea State 7	4	8.5	2.2261	16.69
Sea State 8	5.5	9.7	2.2261	20.57

The density of the Jonswap wave spectrum is calculated by Equation 3 and plotted in Figure 9 for different environmental conditions. Since for each environmental condition, the wind speed must be in accordance with its wave height, so in Table 5, the corresponding wind speed is also given for each wave height.

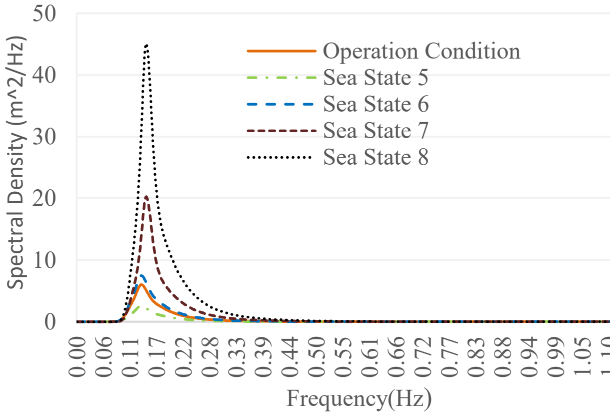

Figure 9. The spectral density for different sea states

4. Failure mode for Hose

Possible failure modes for pipes include tension failure, excessive bending, collision, and fatigue(API, 2008). This study omits the fatigue failure mode. For tension failure mode, the maximum tension should not exceed the allowable tension (F <Fmax) where F is the maximum tension created along the pipes and Fmax is the maximum allowable tension declared by the manufacturer. The critical location for this mode of failure usually occurs at the beginning and end of the pipes. Another mode of failure for the pipes is excessive bending, which is checked by the curvature and bending moment criteria. The amount of curvature and bending moment along the pipe should not exceed the allowed values. Permissible values are calculated by Eq. (4) and (5).

$$\text{Allowable curvature} = 1/\text{MBR} \qquad (4)$$

$$\text{Allowable Bending moment} = \frac{\text{Bend Stiffness}}{\text{MBR}} \qquad (5)$$

in which MBR is declared by the manufacturer, which is equal to 6 and 4 times the inner diameter of the pipe for floating and underwater pipes, respectively. Also, according to the collision criteria, the pipes should not have any contact with other facilities and the seabed.

It is certainly more useful to normalize the outputs and show curves of results for non-dimensional parameters. Therefore, to show the results related to tension and curvature, this results are normalized, so that these values are divided by their allowable value and are introduced as normalized tension and normalized curvature. Allowable values for tension and curvature for floating hoses are 810 kN and 0.27 rad/m, respectively. Also for submarine hoses the allowable tension and curvature are 810 kN and 0.33 rad/m, respectively.

5. Results

Product transfer systems in CALM and SALM terminals are considered the most important component of the terminal. Therefore, the amount of forces created in these systems can help a lot in choosing the best type of oil terminal in a certain area. This paper examined the product transfer system in two terminals, CALM and SALM. The results are as follows.

The amount of tension created in floating and underwater pipes is one of the most important failure criteria to study the behavior of pipe in CALM and SALM terminals as a variable. First, the environmental conditions are considered according to the operating conditions of the Persian Gulf. The results obtained in this step are shown in Figure 10.

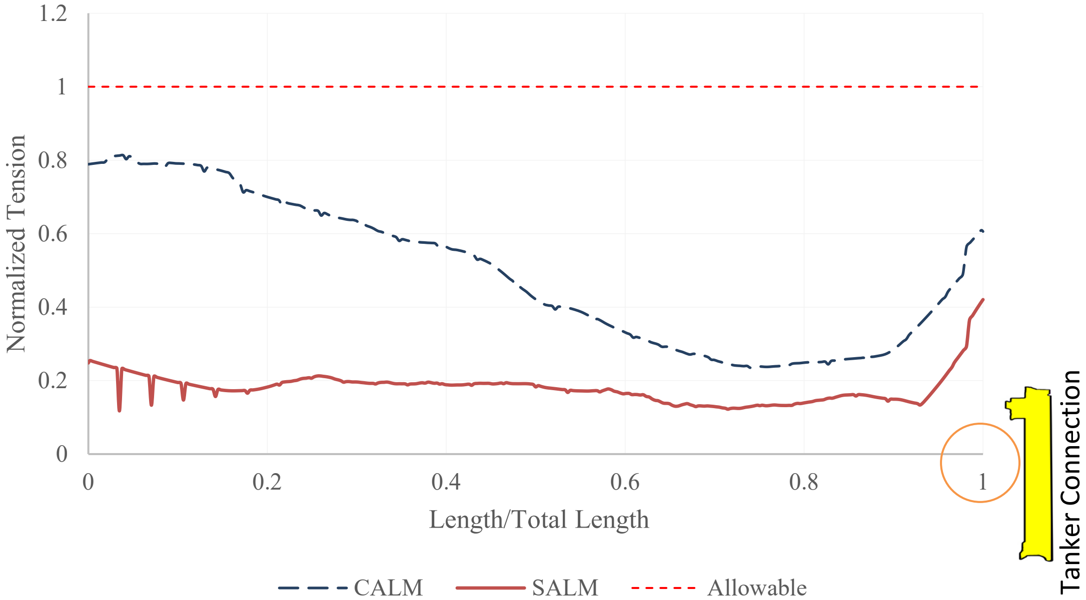

Figure 10. The effective tension in the hose of CALM and SALM oil terminals

The results show that in each terminal, the maximum amount of effective tension occurs at the beginning and end of the pipe. However, the effective tension under operating conditions does not exceed the allowable value in the two terminals. In the CALM terminal, the critical point for effective tension is the connection point of the pipe to the terminal buoy. But, in the SALM terminal, the maximum tension occurs at the connection point of the pipe to the tanker. The maximum effective tension for the CALM and SALM terminal pipe is 658 and 340 kN, respectively.

Another criterion of failure in examining pipe behavior is curvature. Figure 11 displays the amount of curvature along the pipe for the CALM and SALM terminals.

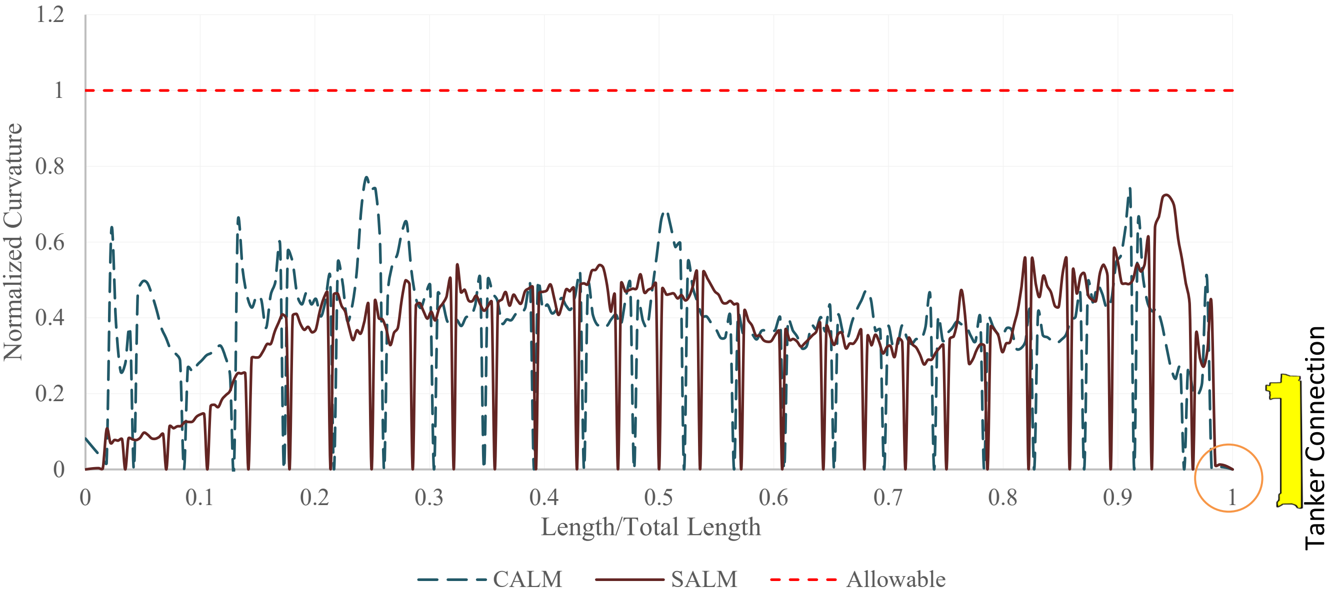

Figure 11. The curvature in the hose of CALM and SALM oil terminals, (a) CALM Terminal, (b) SALM Terminal.

The results show that the amount of curvature along the pipe for the two terminals did not exceed the allowable value. According to Figure 8, since the pipes are connected with different lengths and these different lengths are connected by a flange, the amount of curvature at these points is zero. In the SALM terminal pipe, the amount of curvature in the PLEM part is almost negligible, and the maximum value occurs near the connection to the tanker. In the SALM and CALM terminals, the maximum curvatures along the pipe are 0.21 and 0.2, respectively.

Another thing that should be considered to check the product transfer system in these terminals is the condition that the tanker is not connected and no operation is performed. It is, therefore, necessary to study the stability of these systems under different environmental conditions. In the CALM terminal, when the tanker is not connected, there are floating pipes on the water surface, one end of which is free and the other is connected to the terminal body. The ends of the underwater pipes in these terminals are also connected to the seabed and the buoy. The environmental conditions are increased up to Sea State 8 to determine how the behavior of these systems changes with increasing environmental conditions. The results obtained for the CALM terminal are shown in Figure 12.

(a)

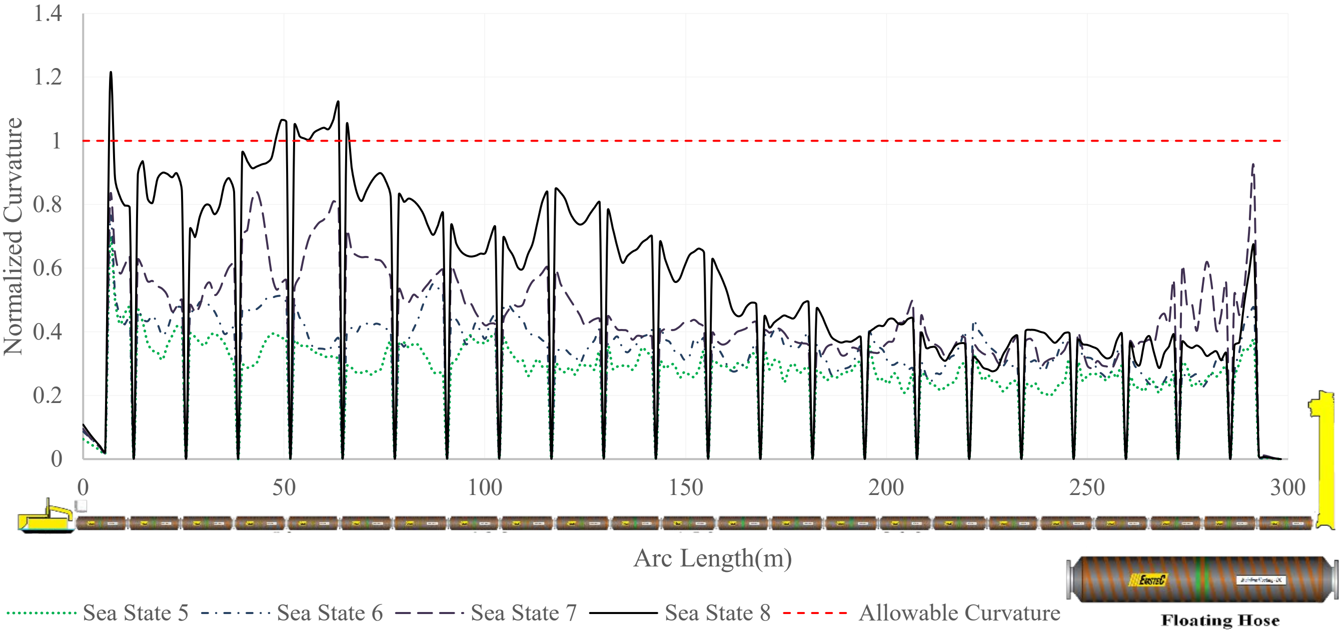

(b)

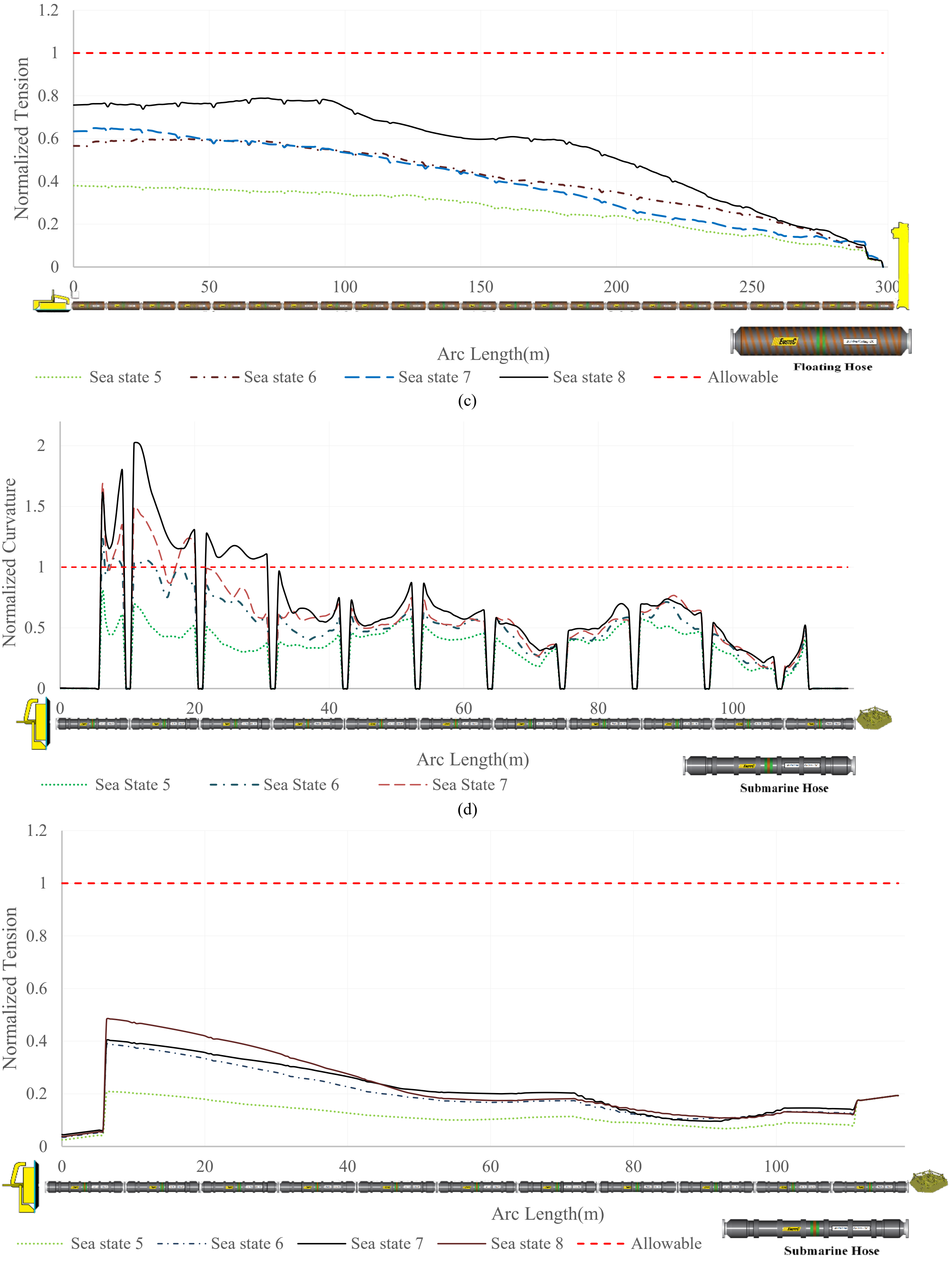

(c)

(d)

Figure 12. The curvature and effective tension generated in the CALM hose under different sea states; (a): The Curvature of floating hose, (b): The Curvature of submarine hose, (c): The Effective tension of floating hose, (d): The Effective tension of submarine hose.

The criterion for studying the response of marine terminal pipes is curvature and tension. The results show that by increasing the environmental conditions to Sea State 6, none of the mentioned criteria are violated, and the terminal can last until these environmental conditions without a tanker connected. But from Sea State 6 onward, the curvature criterion is violated, so it will not have the necessary stability. This is while the effective tension criterion has not exceeded the allowable value up to Sea State 8. It is also observed that the critical location in this terminal with the increase in environmental conditions is the point at which the pipe (floating and underwater) is connected to the buoy.

Unlike the CALM terminal that consists of two separate floating and submarine pipes, product transfer systems in the SALM terminal is composed of floating and submersible pipes that are connected to one another and a single pipe. As the environmental conditions increase to Sea State 8, results are obtained that are shown in Figure 13.

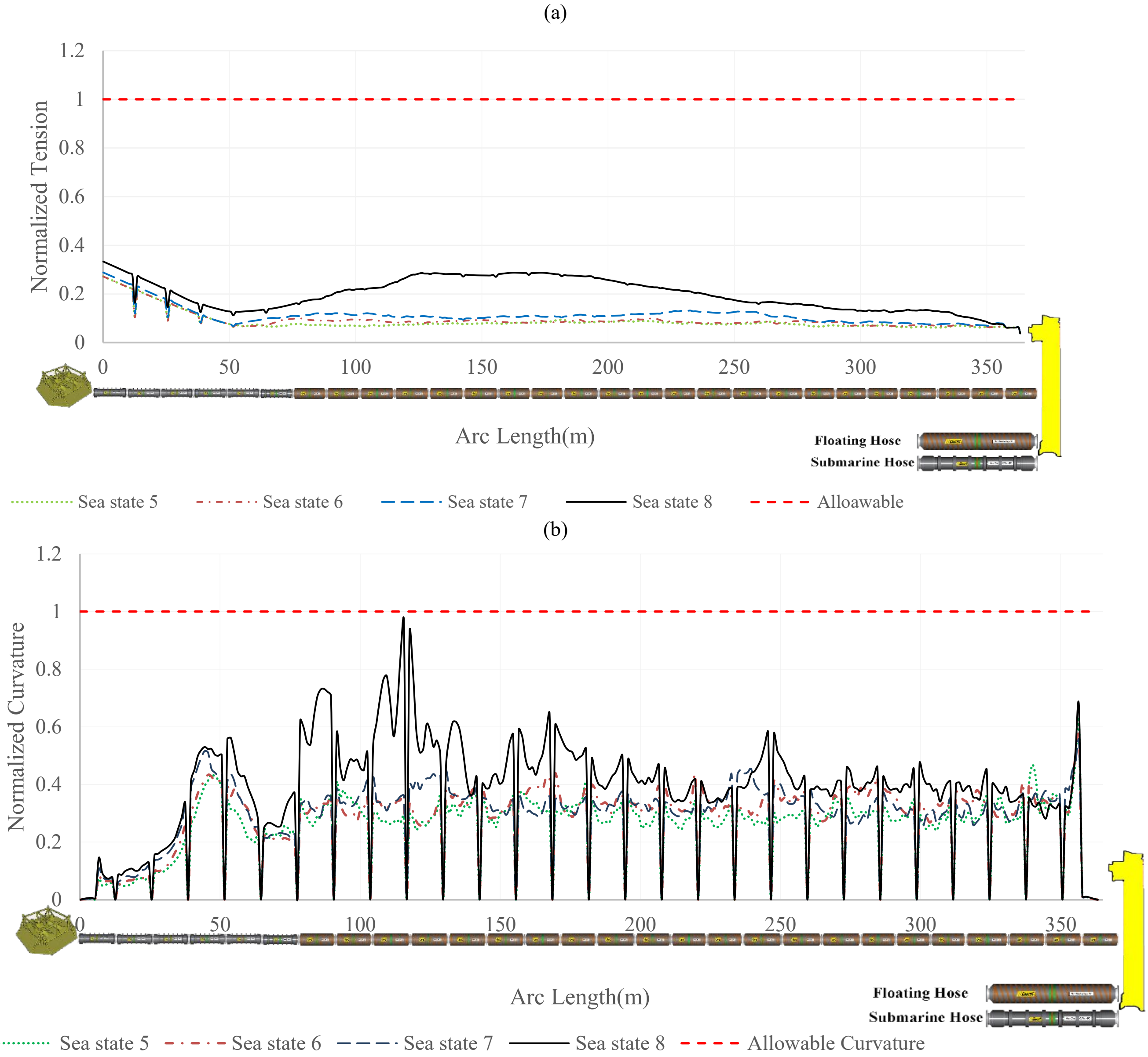

Figure 13. The curvature and effective tension generated in the SALM hose under different sea states; (a): Effective tension, (b): Curvature.

The results reveal that by increasing the environmental conditions to Sea State 8, none of the criteria of curvature and tension for the pipes of this terminal will be violated.

The forces created at the lower end of the pipes (PLEM), connected to the seabed, in the SALM and CALM terminals are of special importance due to the presence of facilities on the seabed. When the terminals are in operating conditions, the forces will be generated in the PLEM section as shown in Figure 14.

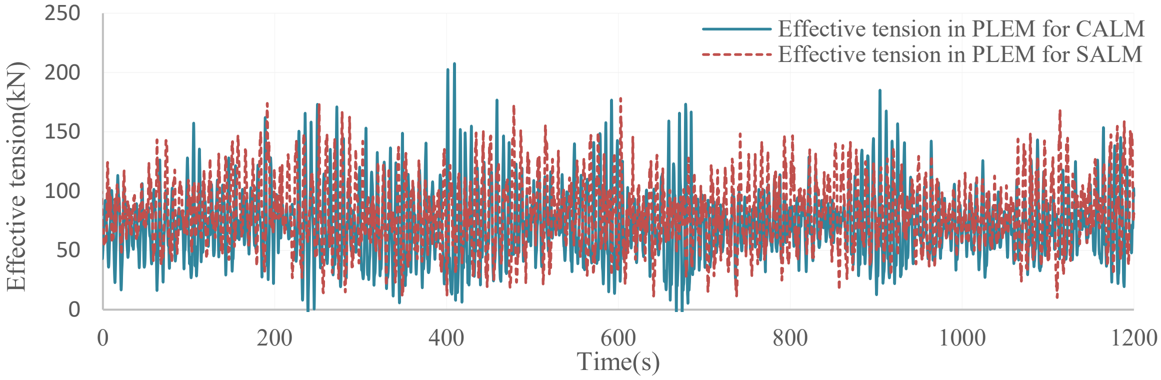

Figure 14. The effective tension generated in PLEM of the CALM and SALM hose under operational conditions.

Based on the results, the time history of the tension created in the PLEM part is lower in the SALM terminal. The maximum tension generated for the CALM and SALM terminals is 207 and 178 kN, respectively.

6. Conclusion

This study investigated the product transfer system, including submarine and floating pipes, in CALM and SALM terminals. First, the response of these systems was examined under the operating conditions of the Persian Gulf. In the next step, the stability of these systems was evaluated under different environmental conditions (up to Sea State 8) when no tanker was connected. The results are summarized below.

- Under the operating conditions of the Persian Gulf, the tension force and the curvature in the SALM terminal product transfer system are created to a lesser extent. The results show that under operating conditions, the curvature and effective tension of the pipes in the SALM terminal are 5% and 93% lower than those in similar operating and environmental conditions in the CALM terminal, respectively.
- With increasing environmental conditions, the product transfer system in the SALM terminal shows more stability when no operation is performed so that this system can be used even for Sea State 8. However, the product transfer system in the CALM terminal can be used for areas whose maximum environmental conditions are in line with Sea State 6.
- The tensions created in the PLEM section in the SALM terminal are 14% less than the tensions created in the CALM terminal.
- The critical point of the product transfer system for the CALM terminal is the connection point of the pipe to the terminal buoy, where the most displacement occurs. But, in the SALM terminal, the critical point for the effective tension of the seabed and for the curvature is the area where the pipe comes out of the water.

List of Symbols

PLEM	Pipe Line End Manifold
CALM	Catenary Anchor Leg Mooring
SALM	Single Anchor Leg Mooring
MBR	Minimum Bending Radius
FSU	Floating Storage Unit
DNV	Det Norske Veritas
API	American Petroleum Institute
OCIMF	Oil Companies International Marine Forum
FPSO	Floating Production Storage and Offloading
RAO	Response Amplitude Operator
QTF	Quadratic Transfer Function

7. References

[1] J. F. Wilson, "Offshore structures (marine engineering)," 2003.

[2] J. J. Ziccardi, "Selection of hose systems for SPM tanker terminals," in *Proceedings of the Annual Offshore Technology Conference*, 1970, vol. 1970-April.

[3] I. Brady, S. Williams, and P. Golby, "A study of the forces acting on hoses at a monobuoy due to environmental conditions," in *Proceedings of the Annual Offshore Technology Conference*, 1974, vol. 1974-May, pp. 1051–1057.

[4] C. Eiken, "Pre-commissioning hose operations on the Valemon field in the North sea." University of Stavanger, Norway, 2013.

[5] X. Qi, Y. Chen, Q. Yuan, G. Xu, and K. Huang, "Calm buoy and fluid transfer system study," in *Proceedings of the International Offshore and Polar Engineering Conference*, 2017, pp. 932–939.

[6] C. V. Amaechi, F. Wang, X. Hou, and J. Ye, "Strength of submarine hoses in Chinese-lantern configuration from hydrodynamic loads on CALM buoy," *Ocean Eng.*, vol. 171, pp. 429–442, 2019.

[7] A. R. C. Girón, F. N. Corrêa, A. O. V. Hernández, and B. P. Jacob, "An integrated methodology for the design of mooring systems and risers," *Mar. Struct.*, vol. 39, pp. 395–423, 2014.

[8] A. R. Cruces Girón, F. N. Corrêa, B. P. Jacob, and S. F. Senra, "An Integrated Methodology for the Design of Mooring Systems and Risers of Floating Production Platforms," in *International Conference on Offshore Mechanics and Arctic Engineering*, 2012, vol. 44885, pp. 539–549.

[9] A. R. C. Girón, F. N. Corrêa, and B. P. Jacob, "Evaluation of safe and failure zones of risers and mooring lines of floating production systems," in *Proceedings of the International Conference on Offshore Mechanics and Arctic Engineering - OMAE*, 2013, vol. 1, p. V001T01A024.

[10] S. Karegar, "Flexible riser global analysis for very shallow water," *Faculty of Science and Technology*, vol. Master. University of Stavanger, Norway, p. 101, 2013.

[11] A. Pecher, A. Foglia, and J. P. Kofoed, "Comparison and sensitivity investigations of a CALM and SALM Type mooring system for wave energy converters," *J. Mar. Sci. Eng.*, vol. 2, no. 1, pp. 93–122, Feb. 2014.

[12] Orcaflex, *OrcaFlex Manual version 9.7a,2015*. section 1;3;4;6;7, 2015.

[13] DNV-RP-C205, "ENVIRONMENTAL CONDITIONS AND ENVIRONMENTAL LOADS," in *The Sixteenth International Offshore and Polar Engineering Conference*.

[14] A. Ozorishin, "FSO concept for shallow waters in the Vietnam offshore oilfield-block Hanoi trough-02." University of Stavanger, Norway, 2012.

[15] D. N. V. O. DNV, "DNV-OS-E301 ((POSITION MOORING))." Det Norske Veritas Offshore Standard, 2010.

[16] OCIMF, "Prediction of wind and current loads on VLCC's," in *Published by Oilcompanies International Marine Forum, London, England, Printed by Witherby & Co Ltd., London, England*, 1977.

[17] R. P. Api, "17B Recommended Practice for Flexible Pipe," *Am. Pet. Institute, Washington, DC*, 2008.

Available online at: www. Ijcoe.org

The impact of the inlet cyclones to the Caspian Sea on the sea level fluctuations

Negin Hatami Bavarsad [1], Dariush Mansoury [2]*, Mohammadreza Khalilabadi [3], Mohammad Malekilonbar[4]

[1] *Graduated in Physical Oceanography, Tarbiat Modares University, Iran; neginbavarsad70@gmail.com*
[2] *Assistant professor, College of Marine Science, Tarbiat Modares University, Iran; mansoury@modares.ac.ir*
[3] *Assistant professor, Faculty of Naval Aviation, Malek Ashtar University of Technology, Iran; khalilabadi@mut.ac.ir*
[4] *Graduated in Physical Oceanography, Tarbiat Modares University, Iran; m.maleki6994@gmail.com*

ARTICLE INFO

Article History:
Received: 21 Jan. 2021
Accepted: 24 Feb. 2021

Keywords:
Sea level,
Atmospheric low pressure,
Wind,
The Caspian Sea

ABSTRACT

In this article, source and trace of the cyclones produced on the Caspian Sea were investigated from 2012 to 2017. The required data for this research consists of water level data recorded at stations such as Amirabad port, as well as other ports, mean atmospheric pressure at the Sea surface and wind data from ECMWF Web site. Results show that source of atmospheric low pressure is from the southwest and west of the Caspian Sea and in 2016 it is from the northern region of this basin. These atmospheric low pressures mostly enter to the Caspian Sea from the northwest of the mid Caspian Sea and their moving trace is to the east and southeast of the southern Caspian Sea. With the investigation of the impact of atmospheric low pressure and wind on the water level of Caspian Sea, in the coasts of Bandar-e Anzali, Fereydunkenar and Amirabad, it was obtained that in 2013 and 2016 low pressure effect and in 2015 wind effect was the most effective phenomena on the water level. The maximum movement velocity of the atmospheric cyclones from 2012 to 2017 was respectively equal to 10.17, 7.96, 44.7, 16.7, and 2.6 m/s.

1. Introduction

The effect of atmospheric cyclones on Iranian water level fluctuations in the Persian Gulf and the Gulf of Oman has been studied in several researches [1, 2, 3]. Variation on sea level when atmospheric cyclone crosses is affected by two phenomena: firstly, wind intensity which causes momentum transmit through pushing the water level and secondly, atmosphere pressure changes which cause fluctuation on the sea level is known as inverse barometer effect [4]. If atmosphere pressure decreases in a region, and air starts to move from surround to the low pressure region, this atmosphere stream is known as cyclone. It is clear that this stream movement to cyclone center is affected by Coriolis force [5]. Pressure centers with respect to the nature and cause of formation are classified into two groups: dynamical and thermal. Thermal pressure centers depended on intensity of the sun radiation and consequently depend on latitude and seasons. Thus, high pressure thermal centers are formed at higher latitudes and during the cold seasons of the year whereas low pressure thermal centers are formed at lower latitudes and during the warm seasons of the year. In other words, the thermal centers depend on the thermal properties and the distance in proportion to the surface of the earth, which decreases in intensity and eventually disappears at an altitude of about 1500 meters above the ground. Dynamical pressure centers are affected by temperature distribution on the earth as an indirect factor, unlike thermal pressure centers [6]. Water level in various ambiances such as oceans, seas, lakes, gulfs, estuaries, rivers, regions far from or close to the coasts changes continuously because of various phenomena [7]. Some marine areas are affected by significant surges several times per year. This phenomenon has historically caused catastrophic water-level enlargements of up to 4.44 m, threatening and claiming human lives and producing major economic and material damages. The negative surges are less frequent, but when they do occur, inhibit the access to the principal harbors and waterways and disable the drinking water intakes of the Metropolitan Area [8]. One of the studies conducted on this field examines the effect of meteorology cyclones transmission on the water level fluctuation in Qeshm channel. The water level and the meteorological data were obtained from National Cartographic Center and Iranian Meteorology Organization, respectively. The results of this research indicate that the period time of the atmospheric cyclones surge in Qeshm channel is about 1-2 days. Statistical investigations, also show that Qeshm channel is mostly affected by cyclones that enter to the region from south or southeast which diminish during moving to the north. Cyclones that enter to the Persian Gulf from northwest rarely reach to the Hormoz strait and Qeshm channel [9]. An analysis of the sea level data (obtained from Kangan and Bushehr Stations-per half an hour), at the northwest of the Persian Gulf showed that in January 2014, there was none-tidal fluctuation. The prominent effects of non-tidal oscillations can also be verified through the data reports obtained from the Kangan and Bushehr Stations [10]. Also, the changes of mean sea level investigated in Persian Gulf during 11 years (starting from 1995). The range of the annually changes is 11.3 cm and the sea level is not significantly dependent on the density and temperature and it is mainly dependent on the pressure [11]. In the Caspian Sea, changes in sea level due to atmospheric circulation were conducted using the MPIM model ((Max Planck Institute for Meteorology). The results emphasize the important role of precipitation in the summer on the Caspian Sea. This study also investigated the precipitation and evaporation of the Volga River and its effect on the Caspian Sea water level [12]. Seasonal variations in water circulation, sea level, and the interaction between atmosphere and sea, investigated by Ibrayev et al. (2010). The model used in this study is the MESH model (Model for Enclosed Sea Hydrodynamics). The results of this study include three-dimensional flow, evaporation, covert heat, sensible heat and changes in the Caspian Sea level. Also, the mean square error of the simulated values and measurements from 1.4 cm at Baku Station change to 3 cm at the Krasnoyarsk station [13]. Mean sea level Equilibrium (MSLE) was studied for a period of ten years from 1999 to 2008 in the Mediterranean Sea. In this study, anomaly changes in density were considered smaller than constant value of density and state equation for density was considered linear and with constant coefficient. It was concluded that the MSLE value obtained from the region in the simulated model represents 2-3 centimeters of error in MSLE values [14]. In another research, the effect of Russia's drought in 2010 on the Caspian Sea was studied. In this hydrological study, the Caspian Sea and the Volga River were studied. This study was conducted for the period from 1993 to 2010, with the emphasis on the severe effect of the European Russia's drought on the Caspian Sea. Figure 1. shows the monthly average of the Caspian Sea water level change for 2009-2011, which shows that water level is decreasing (the numbers in this diagram should be added to the number -27). Another result of this study is the fall in rainfall in July 2010 in the Volga River region, which has led to an increase in evaporation in the area as well as a decrease in the Caspian Sea water level [15].

The model used in this study is the MESH model (Model for Enclosed Sea Hydrodynamics). The results of this study include three-dimensional flow, evaporation, covert heat, sensible heat and changes in the Caspian Sea level. Also, the mean square error of the simulated values and measurements from 1.4 cm at Baku Station change to 3 cm at the Krasnoyarsk station [13]. Mean sea level Equilibrium (MSLE) was studied for a period of ten years from 1999 to 2008 in the Mediterranean Sea. In this study, anomaly changes in density were considered smaller than constant value of density and state equation for density was considered linear and with constant coefficient. It was concluded that the MSLE value obtained from the region in the simulated model represents 2-3 centimeters of error in MSLE values [14]. In another research, the effect of Russia's drought in 2010 on the Caspian Sea was studied. In this hydrological study, the Caspian Sea and the Volga River were studied. This study was conducted for the period from 1993 to 2010, with the emphasis on the severe effect of the European Russia's drought on the Caspian Sea. Figure 1. shows the monthly average of the Caspian Sea water level change for 2009-2011, which shows that water level is decreasing (the numbers in this diagram should be added to the number -27). Another result of this study is the fall in rainfall in July 2010 in the Volga River region, which has led to an increase in evaporation in the area as well as a decrease in the Caspian Sea water level [15].

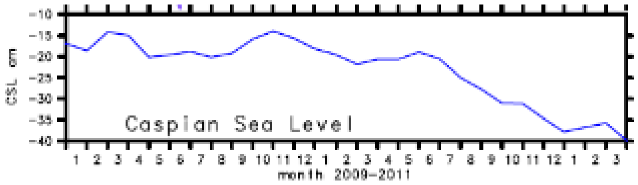

Figure 1. Monthly changes of the mean sea level in the Caspian Sea from 2009 to 2011 (Arpe, et al., 2012)

Seasonal and long-term study of the Caspian Sea water level using satellite and altimeter was conducted by Chen et al., (2017). In this study, with the recording of altimeter data for the years 2002 to 2015, it can be observed that the water level is 20 times lower than global water level furthermore; seasonal fluctuations are larger than mean water level of high seas [16]. Considering that the sea level change is caused by atmospheric cyclones and there is no comprehensive study on the effects of atmospheric cyclones on the Caspian coasts, this research is new. In addition, the use of updated measured data and more statistical periods will affect our understanding of this phenomenon. In this study, the effect of atmospheric cyclones on water fluctuations in the Caspian Sea are investigated.

2. Material and Methods

The study area for the present research is the Caspian Sea, located between Asia and Europe Continents and at 36-48 °N and 46-55 °E. The area is surrounded by Iran, Russia, Turkmenistan, Kazakhstan and Azerbaijan. According to Figure 2, the Caspian Sea can be divided into three parts based on its physical, geographical and topographic conditions: Northern Caspian Basin (NCB), Middle Caspian Basin (MCB) and Southern Caspian Basin (SCB) [17, 18]. The total area of this basin is 168000 km^2 and the deepest point of the Caspian Sea is located at this basin which is 1025 m and the mean depth is 325 m in this basin [19, 20]. Wind and atmosphere pressure data was received from ECMWF database (provided by European Climate Prediction Studies center) during years from 2012 to 2017 with local scale 0.125° and time step 6 hours. Atmosphere pressure from ECMWF database is related to the height of 500 hPa, hence, in this study, the pressure centers is dynamical. The data related to the changes of the Caspian Sea level was also prepared from Caspian research center, recorded in the coasts of Caspian Sea at Bandar-e Anzali, Fereydunkenar, and Amirabad Stations (Figure 2).

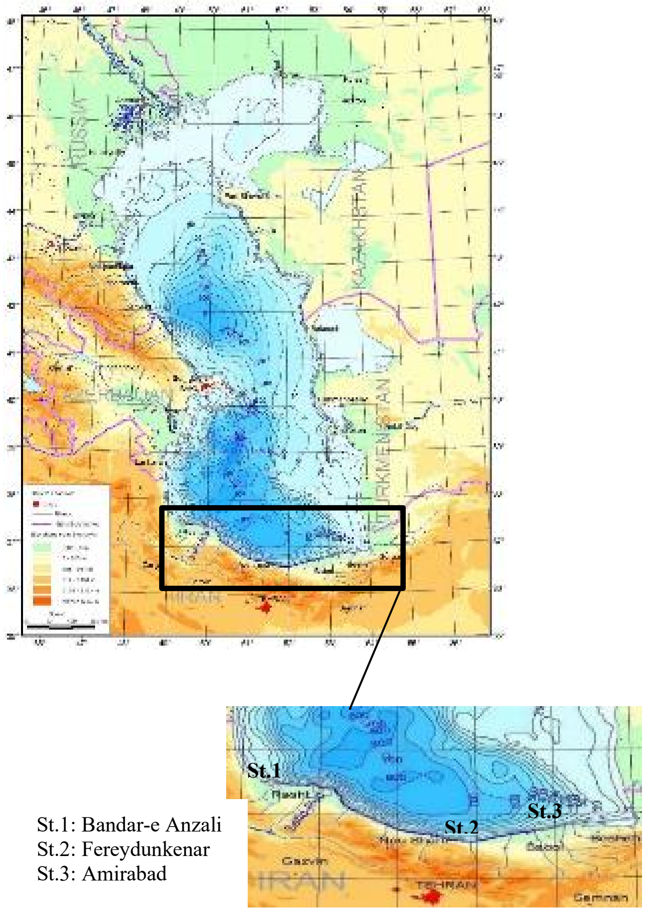

St.1: Bandar-e Anzali
St.2: Fereydunkenar
St.3: Amirabad

Figure 2. Geographical features of the Caspian Sea

To analyze the data, Pyferret software was applied. Pyferret software is suitable media for analyzing the complicated and numerous data. This software was designed and produced for satisfice meteorologist and oceanographer. It was run on UNIX and Mac operating systems as well. Ferret software was developed to the Pyferret version based on Python application [20, 21]. Data with formats such as Netcdf, ASCII and Binary are applicable in this software. Using wind and atmosphere pressure data obtained from ECMWF database, wind and mean surface pressure related to the Caspian Sea were drawn per 6 hours for 1 years [22]. To draw regions with low presser, surfer software was applied and some parameters were analyzed such as number of seasonal atmospheric low pressure, low pressure place, source, movement trace, velocity of atmospheric cyclone movement and the region that cyclone mostly occurs there. Moreover, using time series, the recorded data related to the Caspian Sea level at stations of Bandar-e Anzali, Fereydunkenar and Amirabad, the changes due to the wind and atmospheric low pressure were analyzed. To calculate the changes due to the wind and atmospheric low pressure, at first, the two states of low pressure and normal pressure were recorded, and the pressure difference was calculated based on Pascal. Then, the sea level changes due to the atmosphere pressure were calculated according to the hydrostatical pressure rule (per milibar, pressure decrease causes 1 cm increase in the sea level). Moreover, to calculate sea level changes due to the wind, with respect to the available data of the measurement stations, the level difference for the two mentioned states was calculated. In addition, considering that in this study, sea level changes were studied in a short-term; other factors that have insignificant effects in a short term are ignored in this study such as rivers discharge, evaporation, raining etc. Thus, as the sea level decrease due to the atmospheric pressure, the remaining sea level is allocated to the wind as the most effective factor on the sea level in a short term.

3. Results and Discussion

This study investigates the water level changes in short time ignoring those factors that are not effective in short time. Some of these ignored factors include river discharge, evaporation, raining, etc. Two main factors were investigated in this study that is, wind and mean pressure of the water level. After collecting the data (wind and mean pressure of water level) from the ECMWF database for the years 2012-2017, some parameters were analyzed, including the number of seasonal atmospheric low pressure, the location of atmospheric low pressure, the source and trace of atmospheric cyclone as well as effect of atmospheric low pressure and wind on the sea level.

3.1. Data validation

To validate the study, atmospheric low pressure and the levels of the intended stations were compared. Figure 3 is diagrams of sea level for days before and after the occurrence of the atmospheric low pressure in May (Bandar-e Anzali Station) and November (Fereydunkenar Station). Orange plots on the diagrams show the time of the atmospheric low-pressure occurrence.

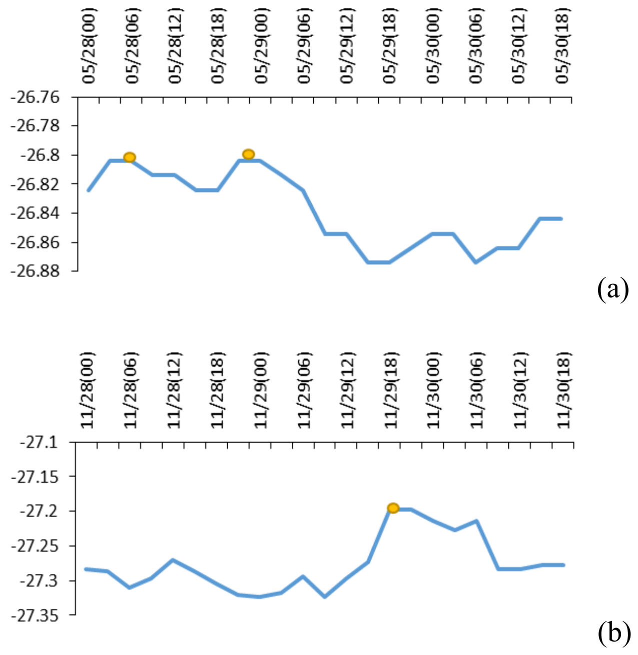

Figure 3. Changes of the Caspian Sea water level on a) May 28th-30th, 2015 at Bandar-e Anzali Station b) November 28th-30th, 2015 at Fereydunkenar Station

3.2. Atmospheric low pressure events

Figure 4 shows the number of the atmospheric low pressure events in the southern Caspian basin monthly from 2012 to 2016. According to Figure 4a, b the maximum of atmospheric low-pressure events is occurred in May and October in 2012 and September and March in 2013.

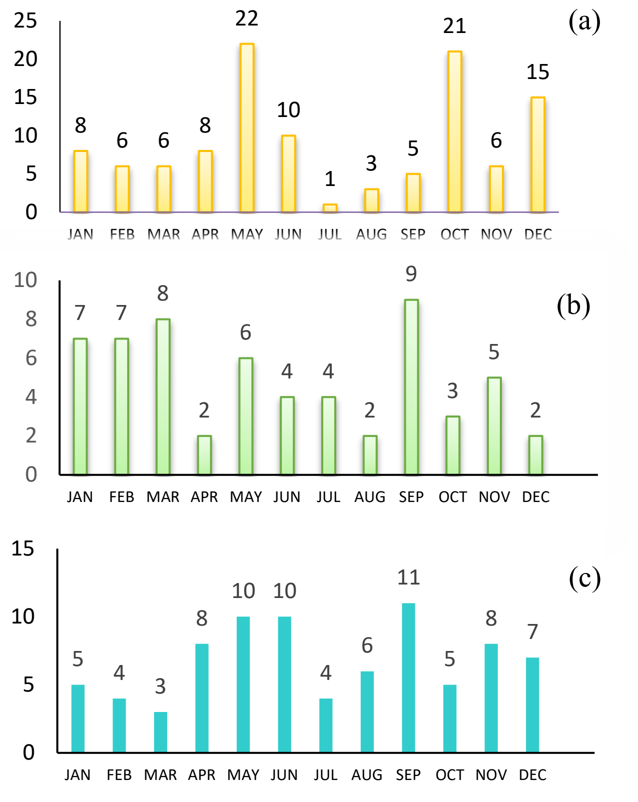

As shown in Figure 4c, in 2014, the maximum of the atmospheric low pressure events are occurred in southern basin of the Caspian Sea in September and May. In 2015, 2016 the maximum of atmospheric low pressure events are occurred in December and May (Figure 4d, e).

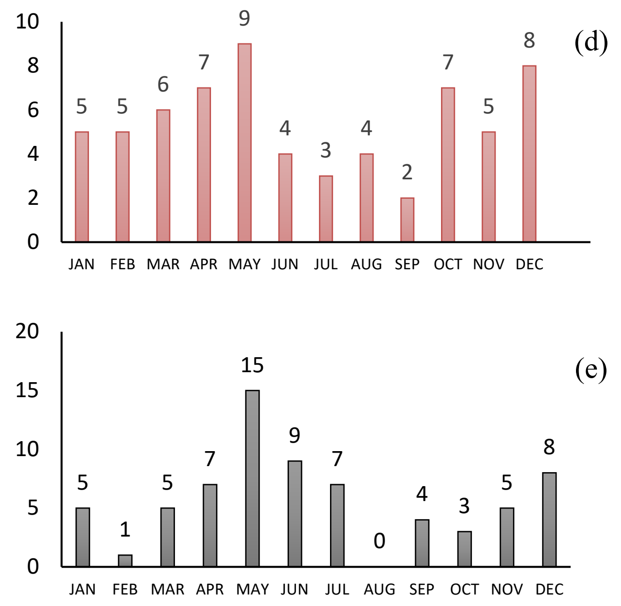

Figure 4. The number of the monthly atmospheric low pressure events in the southern Caspian basin, a) 2012 b) 2013 c) 2014 d) 2015 e) 2016

Figure 5, shows the number of the occurrences of the seasonal atmospheric low pressure in the southern basin of the Caspian Sea. Considering these diagrams and comparing them with the monthly diagrams show that in the whole years (2012-2016), except 2013, the maximum of the atmospheric low pressure events are occurred in spring and autumn.

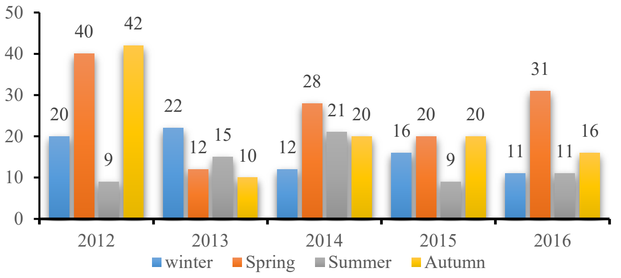

Figure 5. The number of the seasonal atmospheric low pressure events in the southern Caspian basin

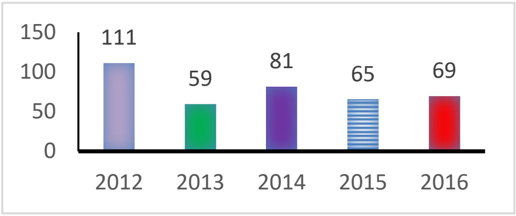

Figure 6. The number of the annual atmospheric low pressure events in the southern Caspian basin

Also, Figure 6, shows that the maximum of the atmospheric low pressure events is occurred in 2012, and the minimum is occurred in 2013. Moreover, by investigating the region with atmospheric low pressure, the latitude and longitude of the atmospheric low pressure center was recorded for 5 years (2012-2016) and plots were drawn on the Caspian Sea by Surfer software. Figure 7, shows the largest numbers of the atmospheric low pressures occurred at the south and southeast. However, in the western region of the middle Caspian basin and some parts of the eastern region of the northern basin, the atmospheric low pressures have occurred less than the southern basin. According to Figure 7, it is concluded that cyclones mostly occur in the southern coasts of the southern basin of the Caspian Sea but about the eastern coast, it is affected by the atmospheric low pressure phenomena because of being flat. It's mean the western coast is more liable to flooding.

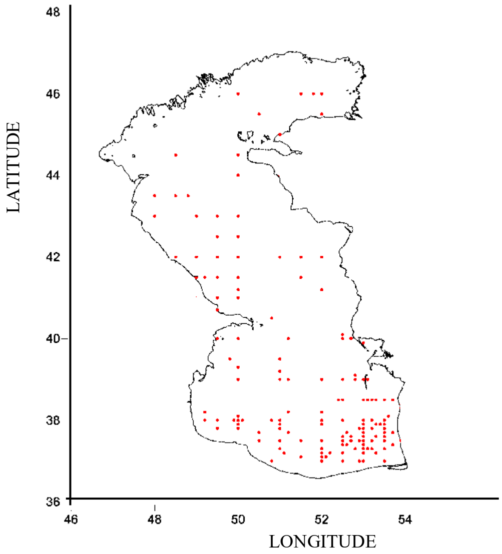

Figure 7. The atmospheric low pressure center in three basins of the Caspian Sea (2012-2017)

3.3. Changes in the Caspian Sea level

The changes in the sea level due to the two factors of atmospheric low pressure and wind in the Iranian coastal stations (Bandar-e Anzali, Amirabad, and Fereydunkenar) during 2013-2016 are shown in Table 1. In Bandar-e Anzali Station in 2015, the atmospheric pressure in the two states of low pressure (Figure 8a) and normal pressure (Figure 8b) were 100500 Pa and 100650 Pa, respectively. Pressure difference between the two mentioned states of pressures is 150 Pa (1.5 milibar). On the other hand, one milibar of pressure decrease causes 1 cm sea level increase and based on this point, the level affected by the atmospheric pressure was calculated. To calculate the changes of the sea level due to the wind, with respect to the measured data of the stations, the sea level relative to the mean sea level for the two mentioned states is -26.99 m and -26.97, respectively. Then the level difference is 2 cm, 1.5 cm of which is due to the atmospheric pressure and 0.5 cm of which is due to the wind.

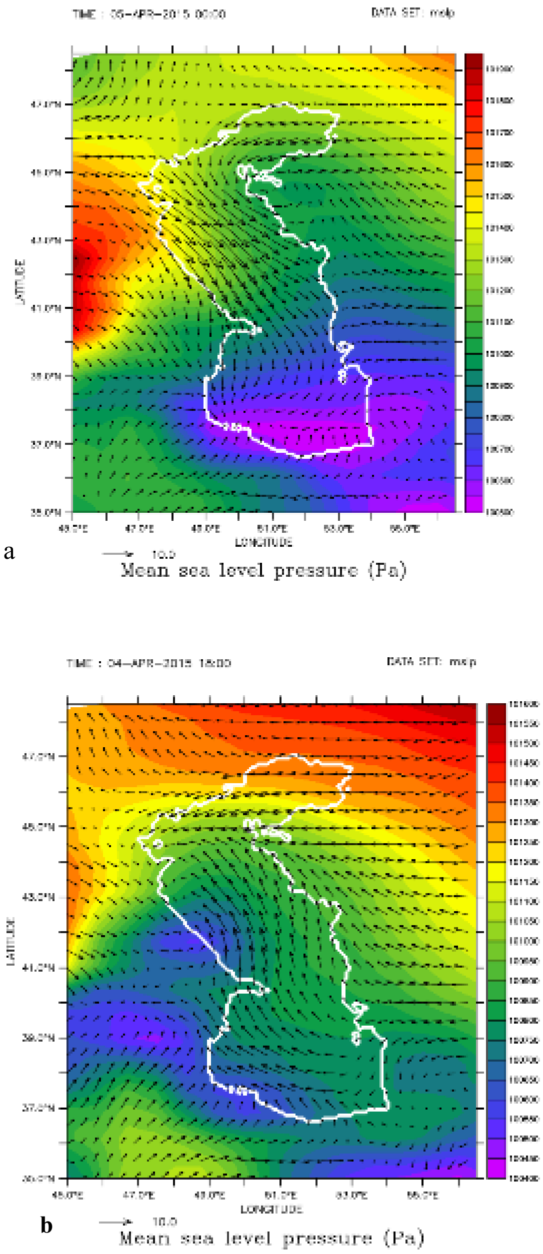

Figure 8. Bandar-e Anzali Station in a) low pressure b) non-low pressure, 2015

Table 1 shows that in Bandar-e Anzali Station in 2013, the atmospheric low pressure factor has had the most effect on the sea level. In 2015, it is observable that the atmospheric low pressure and wind have the most effect at the east of the southern Caspian basin (Amirabad) and the west of it (Bandar-e Anzali), respectively. According to Table 1, changes due to the wind and the atmospheric low pressure in 2016 show that the atmospheric low pressure has the most effect on the sea level in these months. An investigation of the Figures related to this year shows that most of the atmospheric low pressure is also close to the station and the wind direction is also from the coast to the sea.

Table 1. Changes in the Caspian Sea water level due to the atmospheric low pressure and the wind pressure at the Southern Caspian coastal stations (2013-2016)

Station		Date	Pressure (Pa)	Measured water level in station (m)	Increase due to the low pressure (cm)	Increase due to the wind (cm)
Bandar-e Anzali	Low pressure	5/16/2013	100550	-26.365	1.5	0.5
	Non-low pressure	5/15/2013	100400	-26.385		
	Low pressure	7/2/2013	99600	-26.634	4.8	1.2
	Non-low pressure	7/1/2013	100080	-26.694		
	Low pressure	3/9/2013	100950	-26.555	10.5	1.5
	Non-low pressure	3/8/2013	102000	-26.435		
Bandar-e Anzali	Low pressure	11/3/2014	100950	-26.555	1.5	1.5
	Non-low pressure	11/2/2014	102000	-26.435		
Bandar-e Anzali	Low pressure	2/4/2015	100950	-26.994	1	1
	Non-low pressure	2/3/2015	101050	-26.974		
Bandar-e Anzali	Low pressure	5/29/2015	100350	-26.874	1	4
	Non-low pressure	5/28/2015	100450	-26.824		
	Low pressure	8/16/2015	100340	-27.017	1.6	2.4
	Non-low pressure	8/15/2015	100500	-27.977		
Amirabad	Low pressure	11/29/2015	101350	-27.22	2.5	0.5
	Non-low pressure	11/27/2015	101600	-27.25		
	Low pressure	4/5/2015	100500	-26.99	1.5	0.5
	Non-low pressure	4/4/2015	100650	-26.97		
Fereydunkenar	Low pressure	11/29/2015	101400	-27.217	1.5	5.5
	Non-low pressure	11/27/2015	101550	-27.287		
Bandar-e Anzali	Low pressure	2/15/2016	102250	-27.134	3	1
	Non-low pressure	2/14/2016	101950	-27.174		
	Low pressure	3/5/2016	100640	-27.124	3.6	0.4
	Non-low pressure	3/4/2016	101000	-27.164		
Amirabad	Low pressure	2/15/2016	102200	-27.19	2.5	0.5
	Non-low pressure	2/14/2016	101950	-27.16		
	Low pressure	11/14/2016	101850	-27.09	4.5	0.5
	Non-low pressure	11/13/2016	102300	-27.04		
	Low pressure	12/1/2016	101240	-27.11	1.6	2.4
	Non-low pressure	11/30/2016	101400	-27.07		
	Low pressure	5/29/2016	100400	-26.86	4.5	0.5
	Non-low pressure	5/28/2016	100850	-26.91		

Figures 9a-e show, the entry and exit of an atmospheric low pressure system that was studied for 24 hours (from 12 midnights on February 16th, until 12 midnights on February 17th). Based on Figure 9a, an atmospheric low pressure system with a pressure 100000 pa enters from the northwest of the middle basin to the Caspian Sea. This phenomenon, with the velocity of 10.17 m/s and direction of 48.9 degree after 6 hours affects the western coasts of the middle basin and some parts of the southwest coasts of the Caspian Sea (Figure 9b).

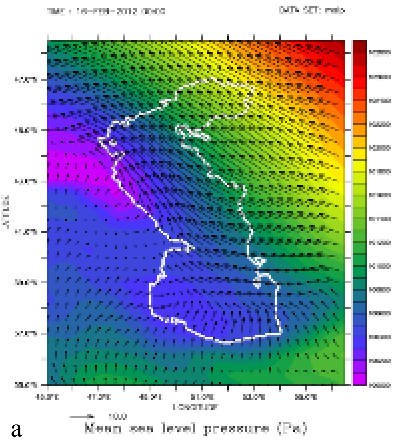

a

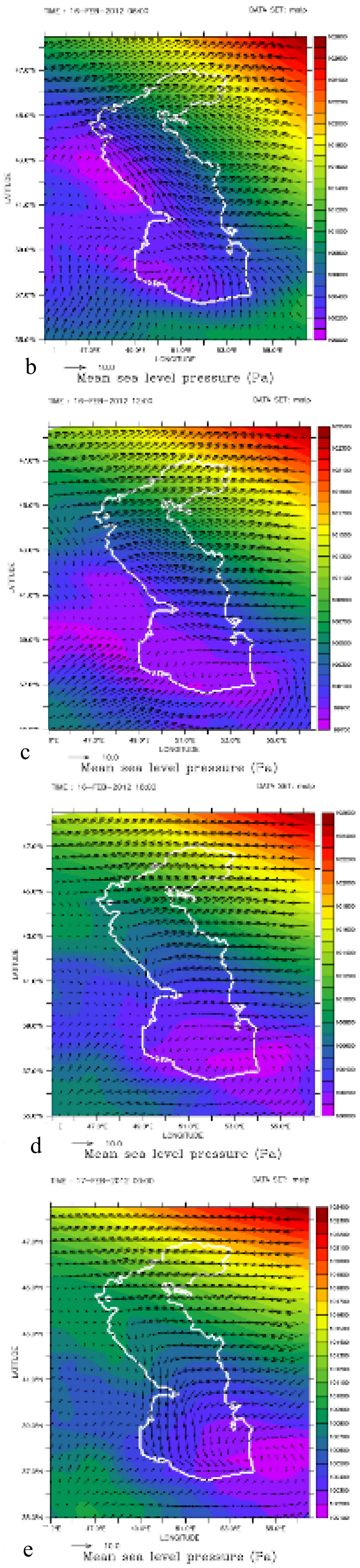

Figure 9. Atmospheric low pressure system on February 16th and 17th, 2012

On August 17th, the atmospheric low pressure creation starts from the southern Caspian basin, with a value 100100 pa (Figure 10a). This system moves with the velocity of 4.83 m/s and the direction of 32 degrees at the east of this basin (Figure 10b). After 6 hours, at 12 o'clock on August, 17th, this atmospheric low pressure vanishes (Figure 10c).

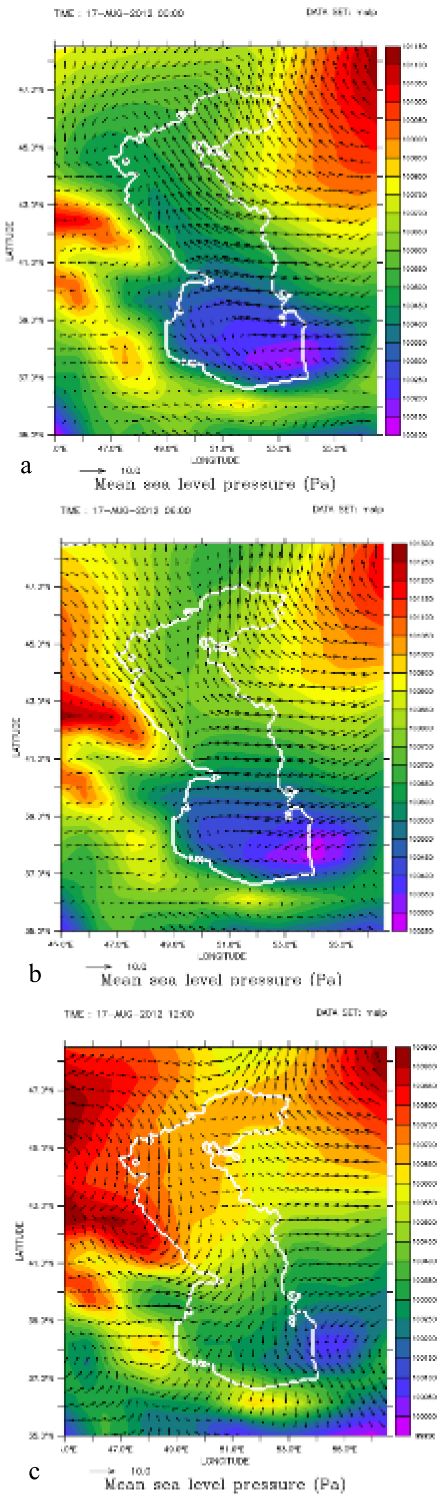

Figure 10. Atmospheric low pressure system on August 17th, 2012

Also, the atmospheric low pressure system enters from the northwest of the middle basin to the Caspian Sea (Figure 11a). It moves with the velocity of 7.96 m/s and direction of 47.72 degree align with the western coasts of the middle Caspian basin (Figure 11b).

After 6 hours, at 12 o'clock on February 16th, the southwest coasts of the southern Caspian basin (especially the Iranian coasts) are affected by the atmospheric low-pressure system 100000 Pa (Figure 11b).

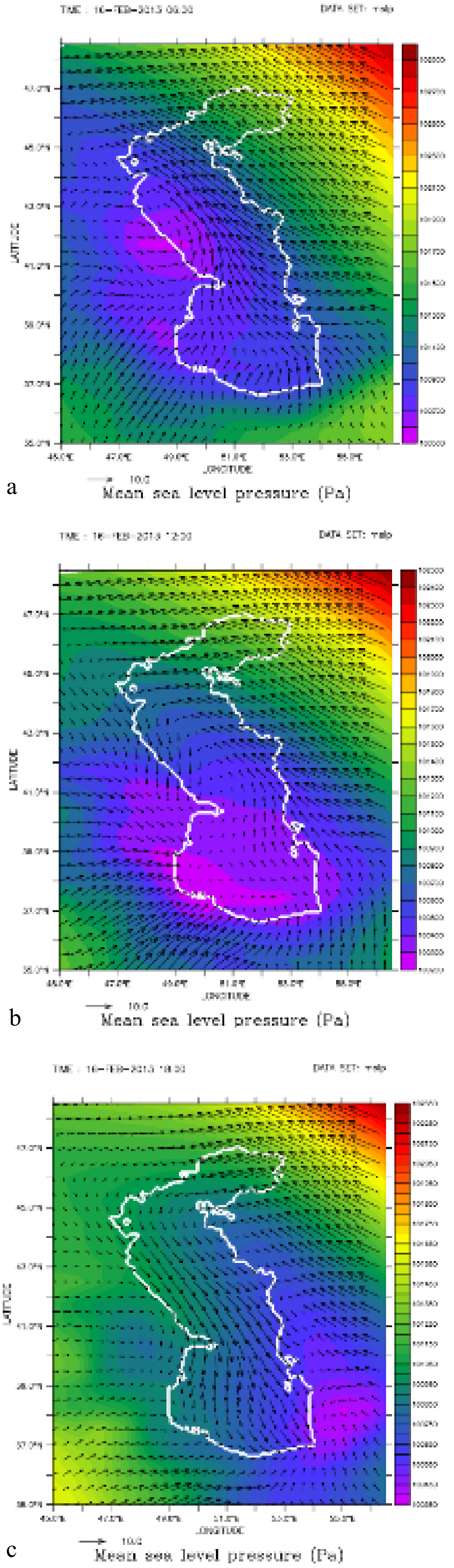

Figure 11. Atmospheric low-pressure system on February 16th, 2013

This atmospheric low-pressure moves with the velocity and direction of 5.02 and 5.7, from the west to the east and at 18 o'clock on February 16th, respectively, it egresses from the southern basin (Figure 11c).

Figure 12, shows the changes of atmospheric low-pressure and the wind pattern for September 18th, in 2013. Based on Figure 12a, the atmospheric low-pressure system surrounded a large part of the middle and the southern Caspian basin and its tense gradually decreases when it moves to the south and the southern region (Figure 12b). Although at 12 o'clock on September 16th, this atmospheric low-pressure system egresses totally from the Caspian Sea basin (Figure 12c), after 6 hours, it moves to the north and along the eastern coasts of the southern Caspian basin with the velocity of 44.7 m/s and direction of 46.3 degree (Figure 12d).

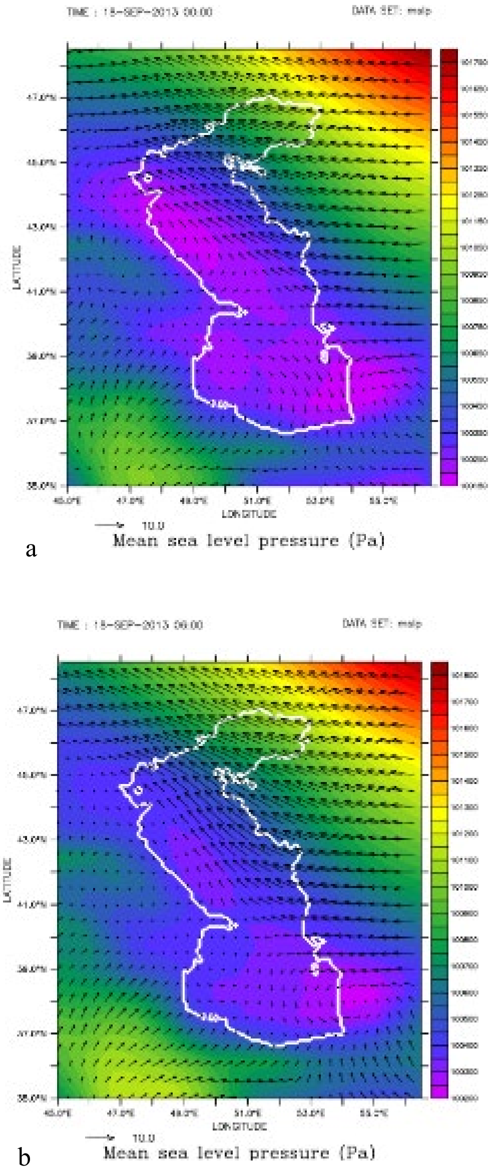

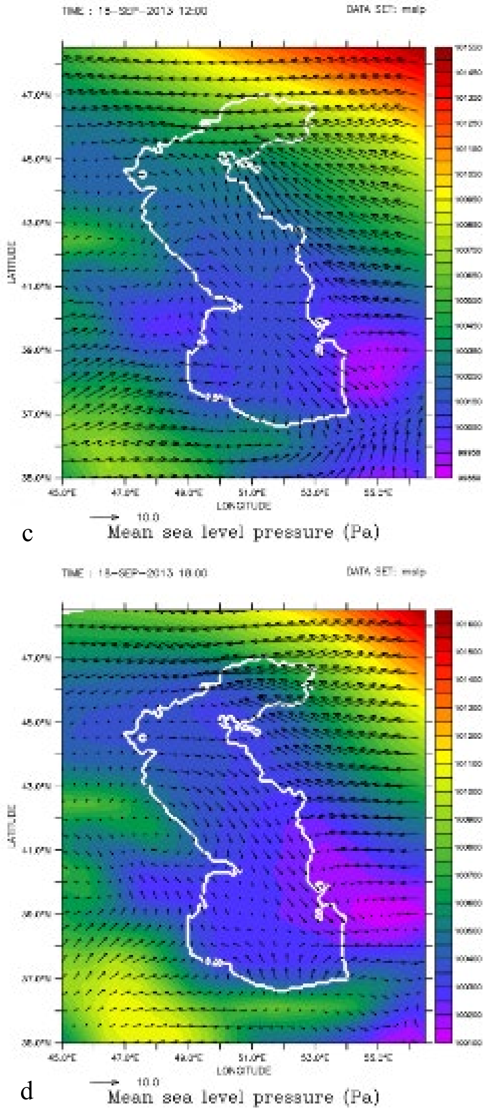

Figure 12. Atmospheric low-pressure system on September 18th, 2013

Figure 13a shows that the atmospheric low-pressure system affected most of the regions of the southern Caspian basin. After 6 hours, this system (at 6 o'clock, February 16th) egresses with the velocity of 1.6 m/s and the direction of 16.6 degree from the east of the southern Caspian basin (Figure 13b, c). At 12 o'clock, February 16th, the southern region of the Caspian Sea (the Iranian coasts of the Northern Province) are mostly affected by atmospheric low-pressure.

Figure 14 shows the changes of the atmospheric low-pressure and the wind pattern for August 19th, in 2013. Based on Figure 14a, the atmospheric low-pressure system enters from the northwest of the middle Caspian basin with the velocity of 44.7 m/s and direction of 46.3 degree to the eastern region of the southern Caspian basin and reaches this region at 6 o'clock, August 19th. This system is egressing with the velocity of 7.58 m/s and direction of 27.92 degree from the eastern region of the southern Caspian (Figure 14b).

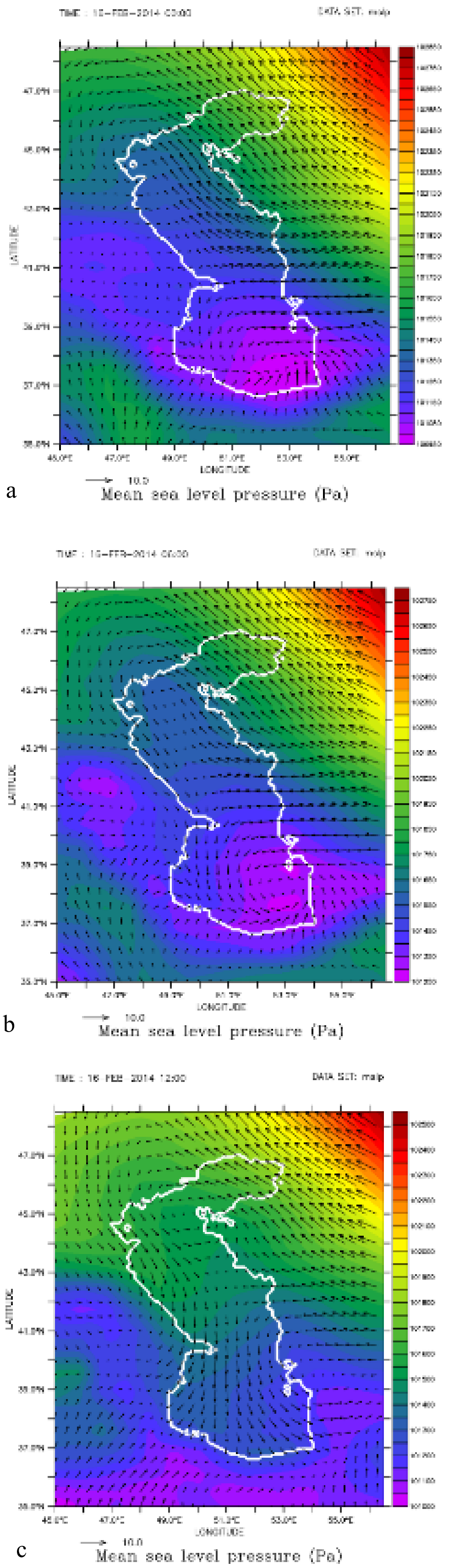

Figure 13. Atmospheric low pressure system on February 16th, 2014

As shown in Figure 15a, the atmospheric low-pressures enter from the west of the mid Caspian to the Caspian Sea and affects the western coasts of the mid Caspian.

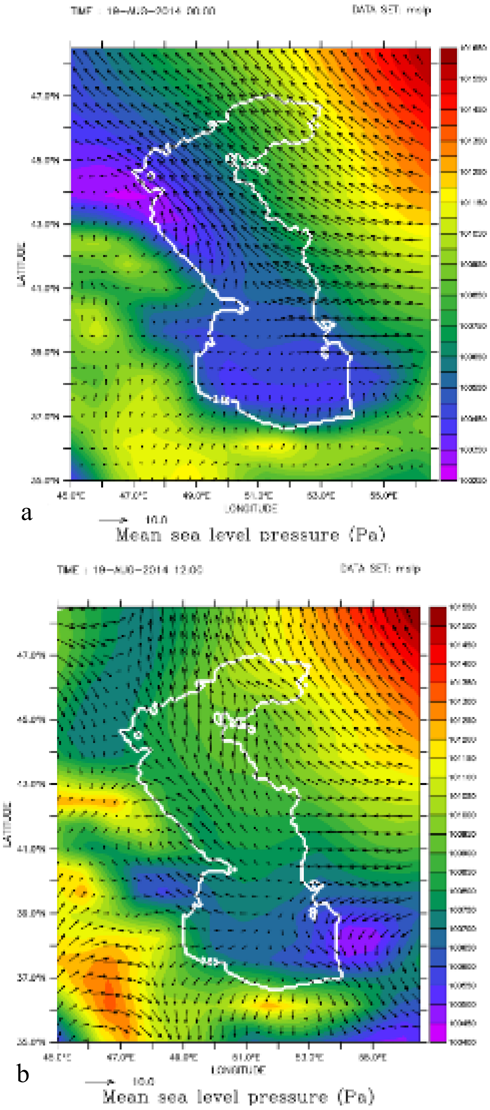

Figure 14. Atmospheric low-pressure system on August 19th, 2014

This atmospheric low-pressure with the velocity and direction of 16.7 m/s and 47.4 degree, respectively, after 6 hours affects the most of the southern Caspian basin and the south of the middle Caspian basin (Figure 15b).

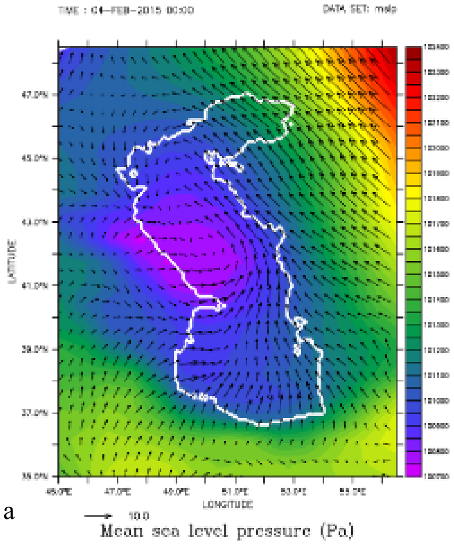

a

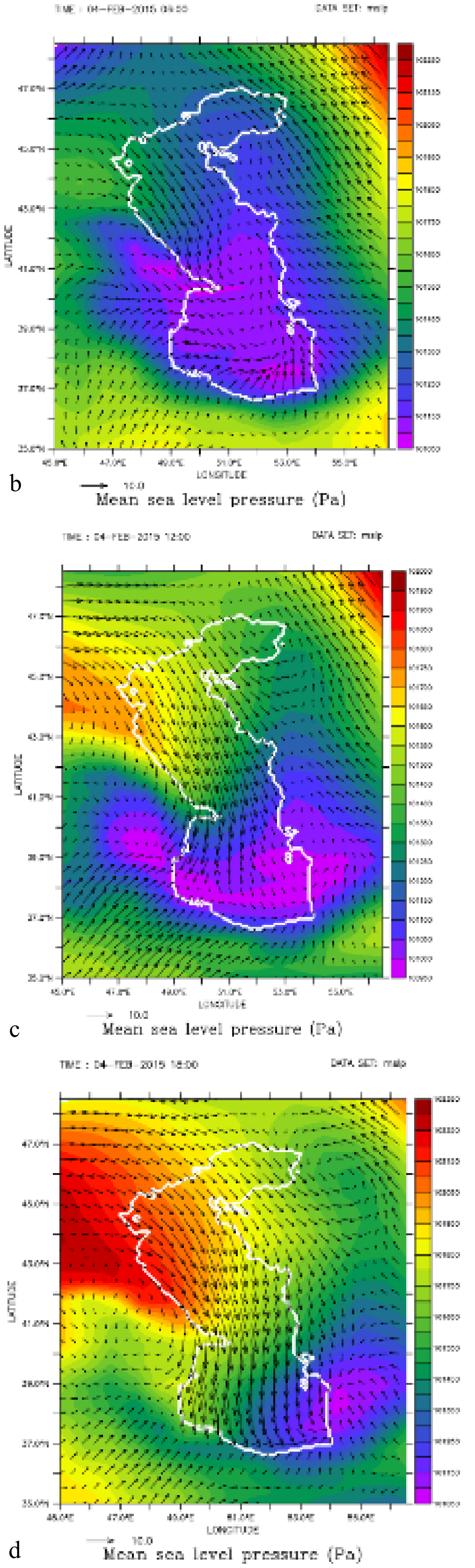

b

c

d

Figure 15. Atmospheric low pressure system on February 4th, 2015

After 6 hours at 12 o'clock, February 4th, the eastern coasts and some coasts at the southwest of the southern Caspian (Bandar-e Anzali) are affected by the atmospheric low-pressure 10095 Pa (Figure 15c). Finally, this atmospheric low-pressure system egresses from the east of the southern Caspian with the velocity of 10.8 and direction of 7.6 degree (Figure 15d).

Based on Figure 16a, the atmospheric low-pressure phenomenon starts from the southeast region of the southern Caspian Sea and far from the coasts. This atmospheric low-pressure is moving with the velocity and direction of 3.91 m/s and 22.78 degree, respectively, toward the eastern region of the southern Caspian basin.

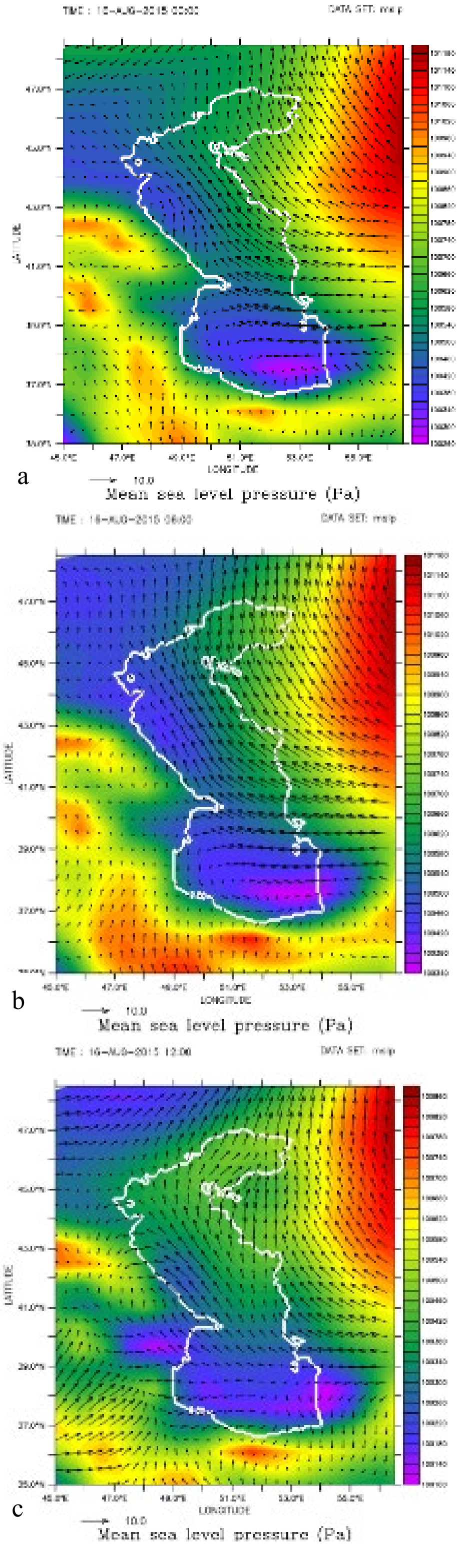

Figure 16. Atmospheric low-pressure system on August 16th, 2015

At 12 o'clock, on August 16th, the atmospheric low-pressure at the southeast of the southern Caspian basin egresses this basin while another atmospheric low-pressure is entering it from the northwest of the southern Caspian (Figure 16b). This system is moving with the velocity of 10.23 m/s to the center and the southeast of the southern Caspian Sea (Figure 16c).

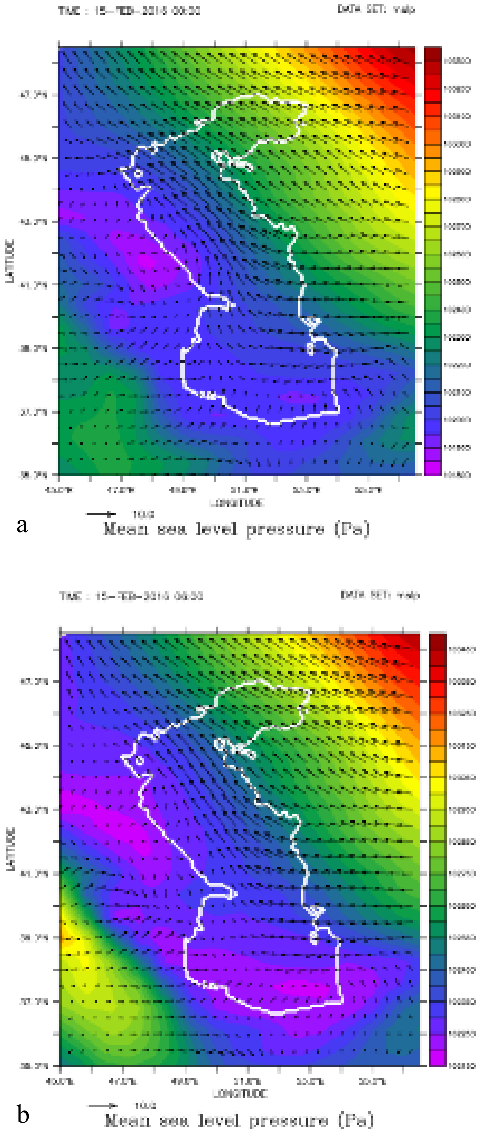

Figure 17. Atmospheric low-pressure system on February 15th, 2016

Based on Figure 17a, the atmospheric low-pressure system, as a rather strong system is moving from the west of the Caspian Sea to the middle Caspian coasts and the southern region of the southern Caspian basin. After 6 hours, at 6 o'clock, on February 15th, it affects all of the Iranian coastal regions. It is clear the changes due to the atmospheric low-pressure and the wind are 2.5 and 0.5 cm, respectively (Figure 17b).

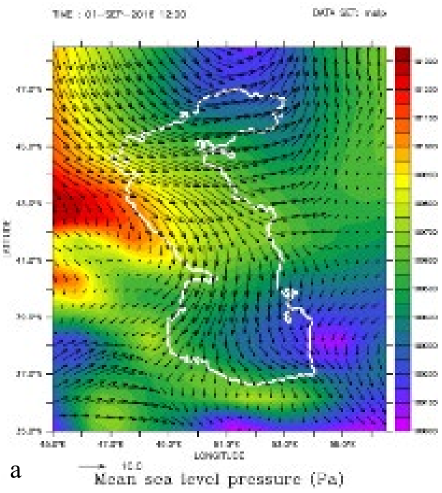

a

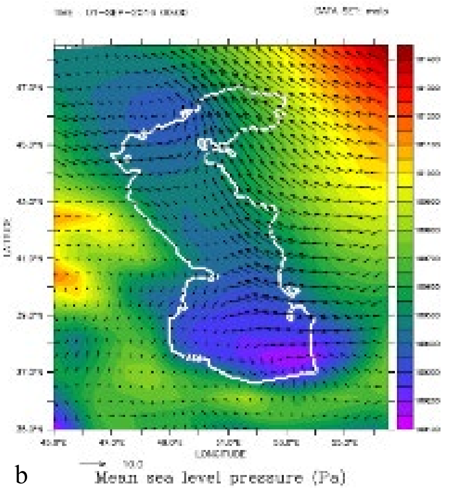

b

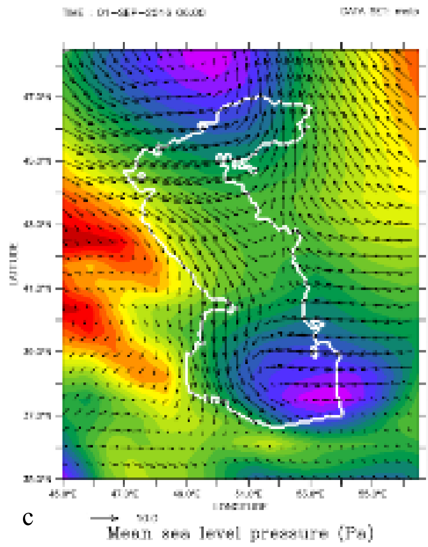

c

Figure 18. Atmospheric low-pressure system on September 1st, 2016

Based on Figure 18a, the atmospheric low-pressure is being created at the southeast of the Caspian Sea. This system is moving with the velocity and direction of 2.6 m/s and 25.5 degree, respectively, to the eastern coasts of the southern Caspian basin. At the same time, another atmospheric low-pressure system at the north of the northern Caspian basin is being created (Figure 18b), which vanishes after 6 hours; the atmospheric low-pressure system in the southeast of the southern Caspian basin is egressing from the eastern coasts of this basin (Figure 18c).

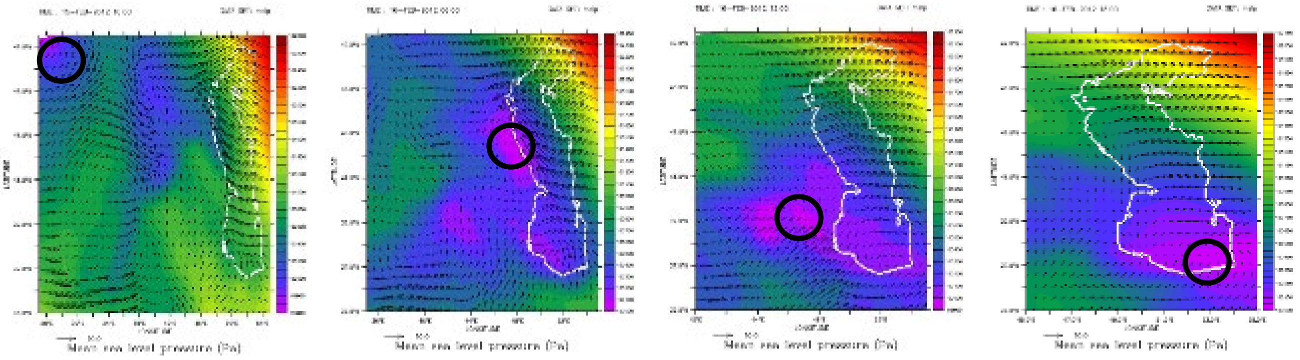

Figure 19. Atmospheric low-pressure tracing, February 15th-16th, 2012

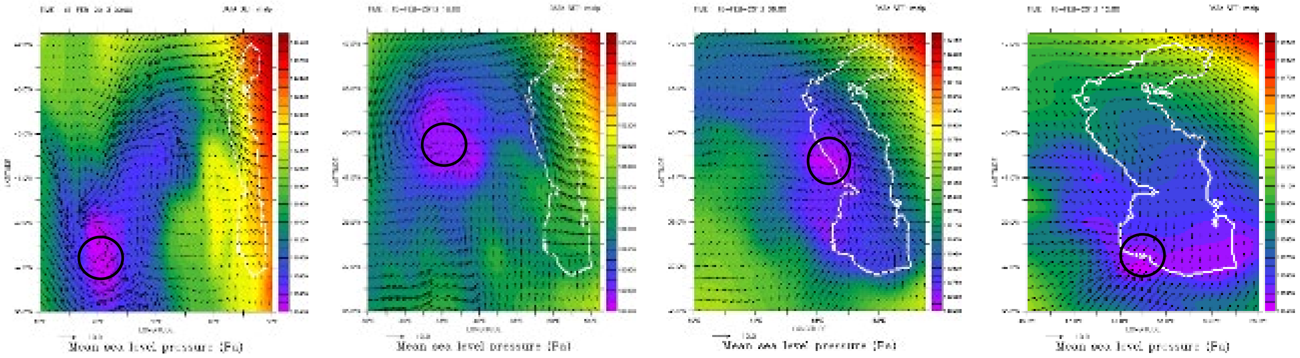

Figure. 20. Atmospheric low-pressure tracing, February, 15th-16th, 2013

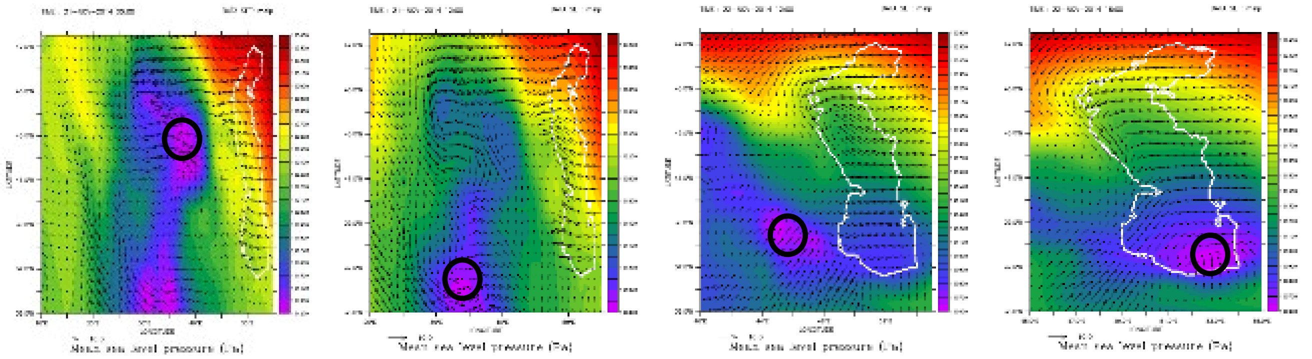

Figure 21. Atmospheric low-pressure tracing, November, 21st-22nd, 2014

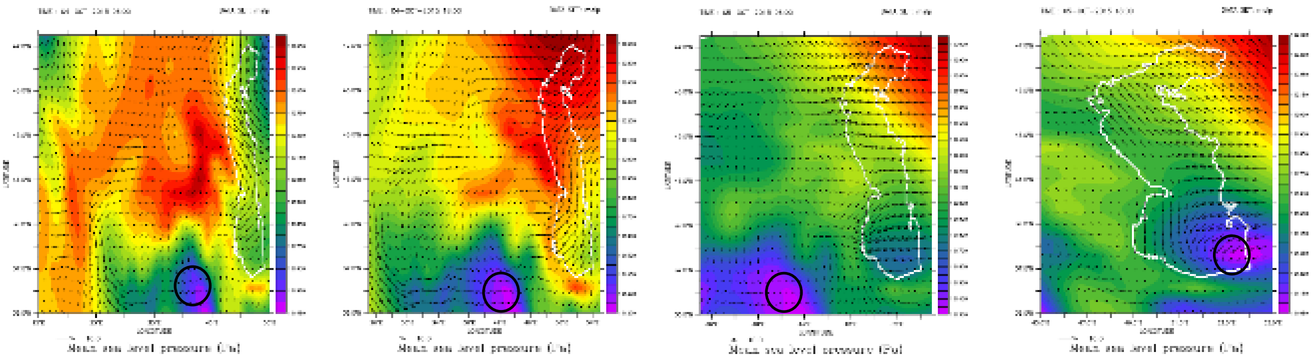

Figure. 22. Atmospheric low-pressure tracing, October, 4th-5th, 2015

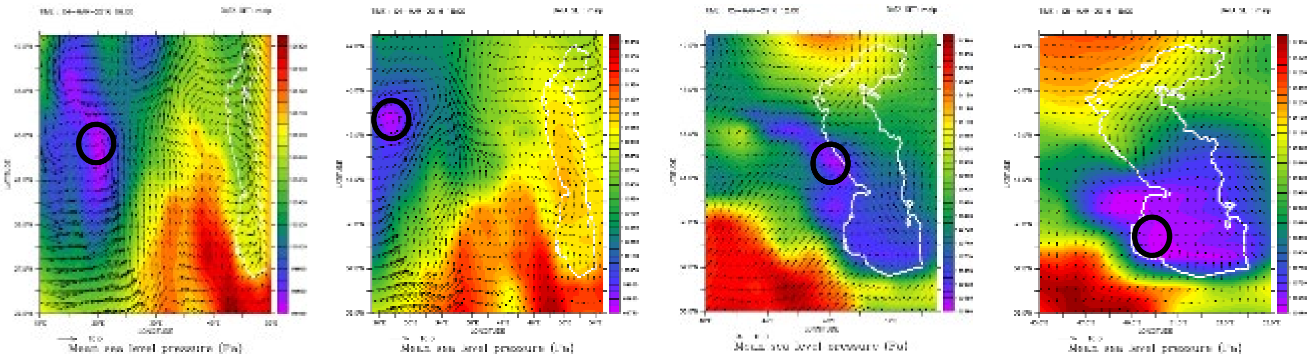

Figure 23. Atmospheric low-pressure tracing, March 4th-5th, 2016

Figures 19-23 show tracing of atmospheric low-pressure from 2012 to 2016 for various months, respectively. According to these Figures, it is observable that in most of these years, the source of the atmospheric low-pressure creation is from the southwest and the west of the Caspian Sea. After some hours, most of the atmospheric low-pressure systems egress from the western coasts of the mid Caspian Sea to the Caspian Sea basin and their destination is mostly the east and the southeast of the southern Caspian basin. In 2016, based on Figure 23, it is observable that the source of low-pressure system is the northwest of the Caspian Sea (high latitude). However, like other years, it enters from the west of the middle Caspian basin to the Caspian Sea.

4. Conclusion

In this research, parameters such as number of seasonal atmospheric low pressure, place of atmospheric low pressure, source and trace of atmospheric cyclones and effects of the atmospheric low pressure and wind on the sea surface level were analyzed. The results of this research show that the atmospheric low pressure mostly occurs in spring and autumn. Also, atmospheric cyclones mostly occur in the southern coasts of the southern Caspian basin. However, the eastern coasts are mostly affected by low pressure phenomenon due to being flat. Investigations on tracing of the atmospheric low pressure shows that in most of these years the source of the creation of atmospheric low pressure is observed to be from the western south and the west of the Caspian Sea. After a few hours, most of the atmospheric low-pressure systems enter from the eastern coasts of the middle Caspian basin to the Caspian Sea basin and their destination is mostly the east and the southeast of the southern Caspian basin. In 2016, it is observed that the source of the atmospheric low pressure is from the northwest of the Caspian Sea (high latitude) but similar to other years, it enters to the middle Caspian from the west of the Caspian Sea. This research studies the effects of wind and the atmospheric low pressure on the sea level in the Caspian Sea in stations such as Bandar-e Anzali, Amirabad and

Fereydunkenar. According to Table 1, it is clear that in 2013, in Bandar-e Anzali Station, the atmospheric low pressure has had a significant effect on the sea level. The Figures related to the atmospheric low pressure show that wind direction is from the coasts to the sea on May 16th. In 2015, it is observable that in the east of the southern Caspian basin (Amirabad Station) and in the west of this basin (Bandar-e Anzali Station), the wind has the most significant effect. In the east of this basin, the direction of the wind is from the coasts to the sea and the low-pressure center is close to Amirabad Station reflecting that the atmospheric low-pressure effect is more than the wind effect in this region. At the west of the basin, the atmospheric low-pressure centers are a bit farther than Bandar-e Anzali Station and the wind direction is from the sea to the coasts and causes mass transition. In this basin, the sea level also increases due to the collision between the bed and waves. Therefore, it is concluded that during the years 2013 and 2016, the low pressure and during the year 2015, the wind has the most significant effect on the sea level. The maximum velocity of the atmospheric cyclone movement from 2012 to 2016 is 10.17, 7.96, 44.7, 16.7 and 2.6 m/s, respectively.

References

1- Khalilabadi MR (2016) *Tide-surge interaction in the Persian Gulf, Strait of Hormuz and the Gulf of Oman.* Weather 71(10):256–261. https://doi.org/10.1002/wea.2773.

2- Khalilabadi, M. R., and Mansouri, D., (2013). *Effect of super cyclone "GONU" on sea level variation along Iranian coastlines.* IJMS Vol.42 (4).

3- Heidari, M., Khalilabadi, M.R., and Bidokhti, A.A., (2012). *Monthly sea level variations in the northern part of Persian Gulf.* Aquatic Ecology, Vol.1: 10-20.

4- Khalilabadi, M., Saranjam, B., (2013). *The fundamentals of the Oceanic Dynamics,* Malekashtar University Publishes, p. 330.

5- Nazmulsadat, M., (2009). *The fundamentals of Atmosphere and Climatology.* Academic Publishing Center, p. 440.

6- Mufidi, A., Zarrin, A., (2006). *An Analysis on the Nature and Structure of High Pressure and Low-Pressure Centers.* Journal of Growth in Education of Geology, No. 47, P. 54-58.

7- Chegini, V., (1998). *Wave Theories.* Jahad Publishes, Water and Watershed Management society, p. 301.

8- Dinápoli, M. G., Simionato, C. G., and Diego Moreira, D., (2020). *Development and validation of a storm surge forecasting/hindcasting modelling system for the extensive Río de la Plata Estuary and its adjacent Continental Shelf.* Natural Hazards 103: 2231-2259.

9- Heydari, M., (2011). *Effect of Meteorological Flows on Fluctuations of Water Level in Qeshm Channel.* Master's Degree in Marine Physics, Islamic Azad University, Science and Research, p. 83.

10- Khalilabadi, M. R., (2016). *The effect of meteorological events on sea surface height variations along the northwestern Persian Gulf.* CURRENT SCIENCE, 110(11): 2138-2141

11- Sultan, S., Ahmad, F., Elghribi, N., Al subhi, A., (1995*). An analysis of Arabian Gulf monthly mean sea level.* Continental Shelf Research, 15(12), 1471-1482.

12- Arpe, K., & Leroy, S.A., (2007). *The Caspian Sea Level forced by the atmospheric circulation, as observed and modeled.* Quaternary international, 173, 144-152.

13- Ibrayev, R., Ozsoy, E., Schrum, C., Sur, H.I., (2010). *Seasonal variability of the Caspian Sea three-dimensional circulation sea level and air-sea interaction.* Journal of Ocean Science Discussions, 6: 1913-1970.

14- Pinardi, N., Bonaduce, A., Navarra, A., Dobricic, S., Oddo, P., (2014). *The mean sea level equation and its application to the Mediterranean Sea.* Journal of Climate, 27, 442–447.

15- Arpe, K., Leroy, S. A. G., Lahijani, H., Khan, V., (2012). *The Impact of the European Russia drought in 2010 on the Caspian Sea level.* Hydrology and earth system science, 16, 19-27.

16- Chen, J. L., Wilson, C. R., Tapley, B. D., Save, H., Cretaux, J. F., (2017). *Long-term and seasonal Caspian Sea level change from satellite gravity and altimeter measurements.* Journal of Geophysical Research: Solid Earth, 122(3), 2274-2290.

17- Dumont, H.J., (2008). *Aquatic Invasions in the Black, Caspian, and Mediterranean Seas (NATO Science Series).* Kluwer Academic, US, p. 314.

18- Naderi Beni, A., Lahijani, H., Mousavi Harami, R., Arpe, K., Leroy, S. A. G., Marriner, N., Reimer, P., (2013). *Caspian Sea level changes during the last millennium: historical and geological evidence from the south Caspian Sea.* Climate of the past, 9(4), 1645-1665.

19- Kosarev, A. N., (2005). *Physico-geographical conditions of the Caspian Sea, The Caspian Sea Environment.* Springer, Vol. 5: p. 5-31.

20- Zereshkian, S., Mansoury, D., (2020). *A study on the feasibility of using solar radiation energy and ocean thermal energy conversion to supply electricity for offshore oil and gas fields in the Caspian Sea.* Renewable Energy, 163, 66-77, doi.org/10.1016/j.renene.2020.08.111.

21- Hankin, S., Callahan, J., Manke, A., O'brien, K., Wei, Y., (2004). *FERRET USER'S GUIDE* Version 5.8, December 20.

22- *Oey. L., Chang, Y. L., Lin, Y. C., Chang, M. C., Xu, F., Lu, H.F., (2012). ATOP-The advanced Taiwan Ocean Prediction System based on the mpiPOM. Part1: Model Descriptions, Analysis and Results.* Terrestrial, Atmospheric & Oceanic Sciences; 24(1), 137-158.

INTERNATIONAL JOURNAL OF
COASTAL & OFFSHORE ENGINEERING
IJCOE Vol.6/No. 1/Winter 2021 (29-35)

Available online at: www. Ijcoe.org

Evaluation of the Soil Properties Effect on Upheaval Buckling of Subsea Pipelines

Abdolrahim Taheri[1*], **Mahdi Tasdighi**[2]

[1*] *Assistant* Professor, Petroleum University of Technology, Iran; rahim.taheri@put.ac.ir
[2] MSc of Offshore Structural Engineering, Petroleum University of Technology, Iran; mahditasdighi@yahoo.com

ARTICLE INFO

Article History:
Received: 14 Nov. 2020
Accepted: 13 Mar. 2021

Keywords:
Upheaval buckling
ABAQUS
Soil properties
Pipeline
Spring

ABSTRACT

Different parameters contribute on the upheaval buckling of subsea pipelines. Seabed is a surface that pipeline contact with it directly. So seabed is one of the most important parameters in the upheaval buckling of subsea pipeline. Subsea pipeline includes imperfection shape and characteristics of the seabed soil. In this paper, different soil types are considered for seabed and modeled with ABAQUS standard code. Seabed is modeled as a two-dimensional springs. The task of these springs is to react like soil against forces. The calculation of spring stiffness is based on standard code of American Lifelines Alliance. The critical stress increases due to the soil cohesion increasing. Soil cohesion is more effective parameter than soil angle friction of the soil. In this study, the effect of temperature difference is evaluated for different types of soil. 10 difference temperature is considered for this evaluation. 50 ℃ to 110 ℃ is the range of mentioned temperature. The effect of difference temperature on the upheaval buckling increases due to increasing of angle friction.

1. Introduction

Subsea pipelines are exposed to upheaval buckling due to high temperatures and pressure [1,2]. Many subjects affect pipeline conditions. The specifications of the space around the pipeline can be the most important factor affecting the risks that may occur to the pipeline [3]. The pipeline is surrounded by water and seabed. Hydraulic pressure is inserted into the subsea pipeline due to sea water [4,5]. Also, high pressure and high temperature creates axial force on subsea pipeline [6]. Pipeline reacts due to hydraulic pressure and other pressures on the pipeline. This reaction is called buckling. In the buried pipeline, soil cover weight is less than the surrounding soil weight, so upheaval buckling is possible. Vertical movement is important in upheaval buckling of pipeline. The intensity of vertical reaction depends on the characteristics of the seabed [7-10]. So, seabed characteristic is one of the most important parameters in upheaval buckling. The importance of soil type has proven on upheaval buckling studies so that the soil type in this study are listed. In previous studies have been marked the type of seabed soil and theses study divided to two parts, clayey seabed [11,12] and sandy seabed [13,14] separately. Previous studies not discuss about detail of soil characteristics and its effect on upheaval buckling. ABAQUS standard code is the most commonly used software for numerical analysis of upheaval buckling. Previous studies are modeled seabed as rigid surface [15-17]. Analytical rigid surfaces are geometric surfaces with profiles that can be described with straight and curved line segments. An analytical rigid surface is associated with a rigid body reference node whose motion governs the motion of the surface. An analytical rigid surface does not contribute to the rigid body's mass or inertia properties analytical rigid surfaces are always single-sided with their orientation specified through their definition. Therefore, contact interaction is recognized only on the outer boundary of an analytical rigid surface. To model contact on both sides of a thin structure, use an analytical rigid surface that wraps around the boundary of the thin structure.

In this study, different seabed soils are considered and have been compared with each other. The main aim of this study is to evaluate the effect of soil types on upheaval buckling. In this study, the effect of temperature difference is evaluated for different types of soils. 10 difference temperature is considered for this evaluation. Upheaval buckling is modelled with ABAQUS standard code and seabed is modelled as 2d spring in 2 directions. The critical stress increases due to the soil cohesion increasing. The effect of difference temperature on the upheaval buckling increases due to increasing of angle friction. Soil cohesion is more effective parameter than soil angle friction of the soil.

2. FE model

The length of pipeline is considered 500 (m) for ABAQUS modeling. The two-dimensional beam elements were used to pipeline model. According to DNV-F-110 (2006) recommendation, mesh size assumes 0.5 (m). The pipeline is modelled as 2D beam with PIPE21 elements. Nonlinear spring with Spring1 element is used for seabed modeling.

Initial imperfection is a key parameter for upheaval buckling starting. The most common initial imperfection assumption used by the previous researchers, the sinusoidal profile imperfection is:

$$f(x) = {}^{W_0}/_{2}\left(1 + \cos\left({}^{2\pi x}/_{L_0}\right)\right). \; -{}^{L_0}/_{2} \le x \le {}^{L_0}/_{2} \qquad (1)$$

Imperfection height and wavelength are defining imperfection parameters. Imperfection properties are shown in table 1.

Table 1. Imperfection properties

Characteristic	Value
Wave length(m)	60
Imperfection height(m)	0.15

Static analysis is used step in ABAQUS model. The basis of this analysis is nonlinear buckling analysis. There is difference temperature due to fluid flow through the pipeline in operation that is causing to axial force to pipeline. The amount of difference temperature is variable for this model.

The soil is modeled as spring in this model. Figure. 1 illustrates the general schematic of using axial, lateral and vertical springs for soil modeling of buried pipeline. The calculation of spring stiffness is based on standard code of American Lifelines Alliance [18].

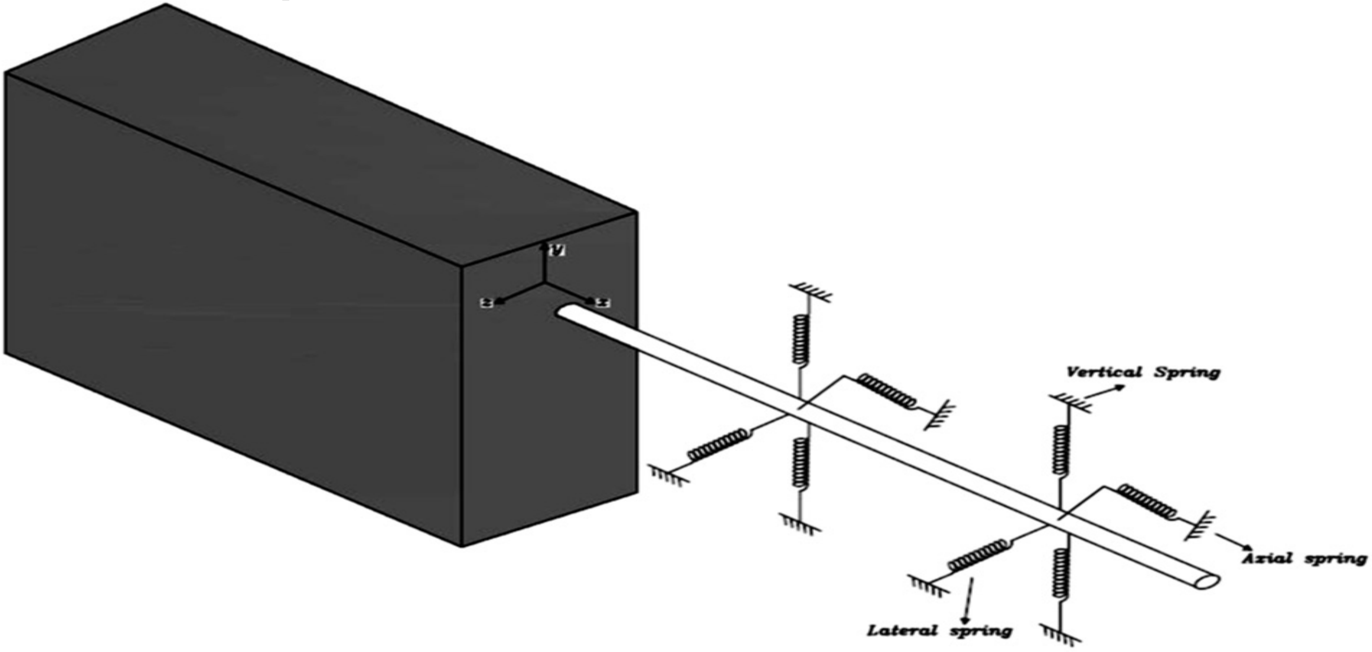

Figure 1. General schematic of using axial, lateral and vertical springs for soil modeling [18]

3. Methodology

This research is focused on the effect of soil specification on upheaval buckling. To achieve this aim, seabed is modeled with different types. Table 2 is shown the specification of used soils.

In the past 30 years, the researcher summarized models of buckling of the pipeline. These models are suitable for a certain condition.

The Terndrup-Pedersen's assumptions [20]:

- Pipeline a is linear beam;
- Seabed is rigid;
- Effect of the soil cover is fixed; this model is suitable for pipeline with the small vertical displacement;
- Pipeline is completely elastic;
- Pipeline and trench bottom may be imperfect;
- Initial imperfection is considered for seabed and pipeline.

The imperfection shape is defined by:

$$\omega_f = \delta_f \left(\frac{x}{L_0}\right)^3 (4 - \frac{3x}{L_0}) \tag{2}$$

Where

$$L_o = (\frac{72EI\delta_f}{q_f})^{\frac{1}{4}} \tag{3}$$

Where:

δ_f= Initial imperfection height

q_f= Pipe submerged weight

Figure.2, illustrates the imperfection shape of a pipeline with expressed assumptions. The pipeline loaded with a weight of per unit length. Also, it is assumed that the below area of pipe is not empty.

$$\omega_f = \delta_f \left(\frac{x}{L_0}\right)^3 (4 - \frac{3x}{L_0}) \tag{4}$$

Where

$$L_o = (\frac{72EI\delta_f}{q_f})^{\frac{1}{4}} \tag{5}$$

Where:

δ_f= Initial imperfection level

q_f= Pipe submerged weight

Figure.2, illustrates the deflection shape of an elastic pipeline with bending stiffness EI placed over a protruding object of height f and loaded with a weight of per unit length. Besides, it is assumed that the cavity below the propped pipe will be filled with soil, either through natural process or engineering backfill procedures.

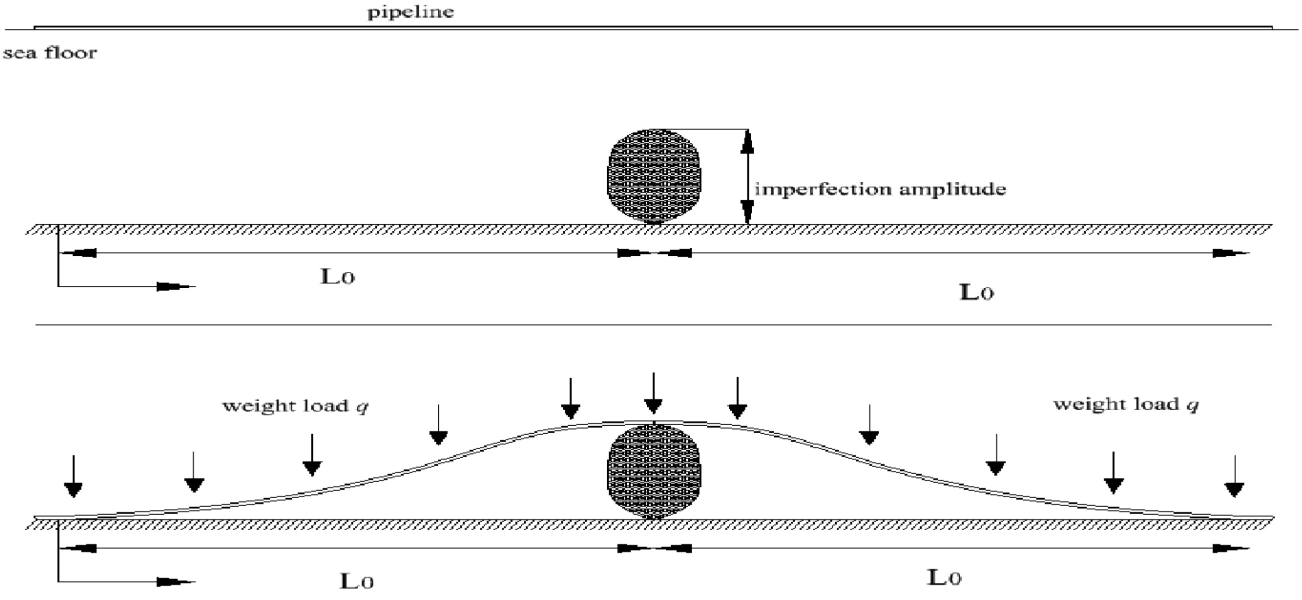

Figure 2. Pipeline position on initial imperfection [19]

Figure. 3, illustrate the uplift op pipeline with initial imperfection in the x-w coordinate system, as shown in, the uplift amount of pipeline with initial imperfection can be given as:

$$EI\frac{d^4}{dx^4}(\omega - \omega_p) + N\frac{d^2\omega}{dx^2} + q = 0 \tag{6}$$

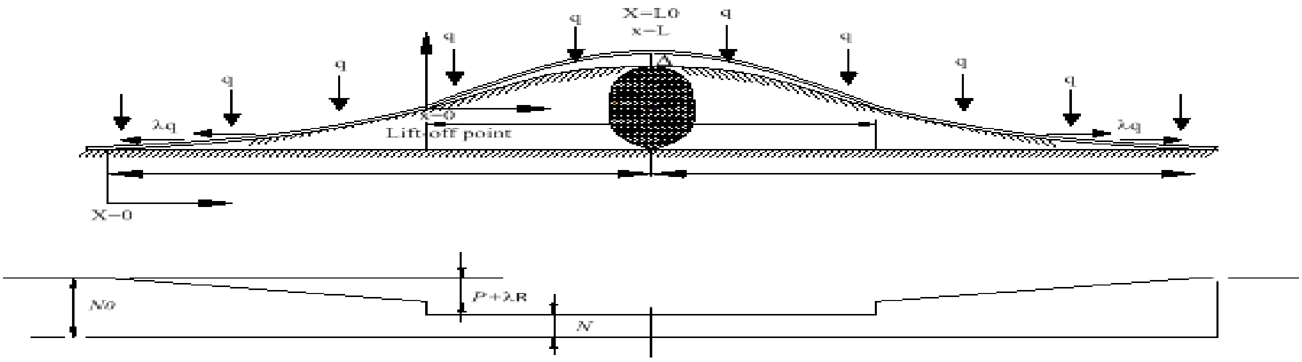

Figure 3. Upheaval buckling of pipeline with initial imperfection [19]

Table 2. Specification of different soil types

Parameters	Clay	Muddy Clay	Silty Clay	Reclaimed Sand (RS)	Drainage Coarse Sand (DCS)
$\rho_{sat}\ (KN/m^2)$	17.84	18.15	18.32	19.64	20.71
ϑ	0.30	0.35	0.30	0.28	0.25
$C\ (KPa)$	11	9	12	0	0
$\emptyset$ (°)	14	15	18	28.9	32

The general effective download can be given as:

$$q = q_{pipe} + q_s \quad (7)$$

Where:

q_{pipe}= Pipe submerged weight

q_s= Uplift resistance of the cover material

Where:

$$q_s = \gamma_c \left(HD_o - \frac{\pi}{8}{D_o}^2 + H^2 tan\varphi_c\right) g \quad (8)$$

$$q_{pipe} = m_0 g \quad (9)$$

Where:

D_o= Overall outside diameter including coatings

c= Submerged weight of burial material per unit volume, 1023 kgm3 in this paper

g= Acceleration Due to Gravity

H= Minimum height of the cover soil measure between the pipe centerline and the seafloor

m0= Submerged mass per unit length of the pipeline

Then allowable temperature rise may be calculated with the equation.

$$N_o = \frac{\pi}{4} E\alpha_s\left({D_e}^2 - {D_i}^2\right)\Delta T + \frac{\pi}{4}(1 - 2\vartheta)\left(p_i {D_i}^2 - p_o {D_e}^2\right) \quad (10)$$

This modeling is focused on the effect of soil specification on upheaval buckling. To achieves this aim, seabed is modeled with different types. Table 2 is shown the specification of used soils.

Temperature plays important role in upheaval buckling. In this study, the effect of temperature difference is evaluated for different types of soil. 10 difference temperature is considered for this evaluation. 50 °C to 110 °C is the range of mentioned temperature.

In this study, the aim is the evaluation of the influence of soil characteristics on upheaval buckling. In this study, the soil is modeled as spring. The task of these springs is to react like soil against forces.

3.1. Results

Figure 2 shows the critical stress increase due to increasing of difference temperature. Figure2 describes this process for the different type of soils. According to soil characteristics which is shown in Table 1 and Figure. 2, the critical stress increases due to the soil cohesion increasing. According to the comparison between the curve of clay and muddy clay, soil cohesion is more effective parameter than soil angle friction of the soil.

Also, the slope of curves increases due to increasing of angle friction. In other words, the effect of difference temperature on the upheaval buckling increases due to increasing of angle friction.

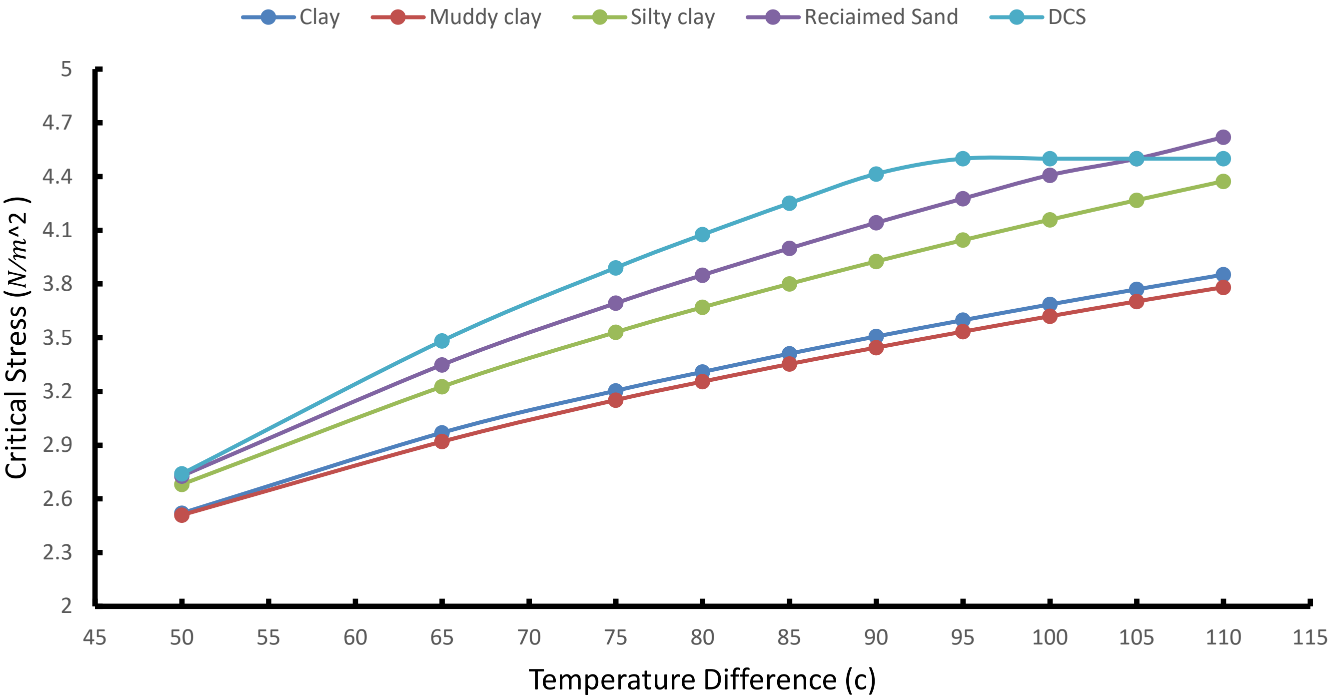

Figure. 2. The critical stress of upheaval buckling for different soils

Figure. 3. illustrates the maximum amplitude of upheaval buckling for different soils. As is shown in Figure. 3, the buckle amplitude increases due to increasing of soil cohesion in clay soils and the buckle amplitude increase due to increasing of friction angel in sand soils. According to distance between curves, the effect of temperature difference due to friction angel increasing in sandy soils is more than clayey soils. Also, the curve slope is constant for different soils.

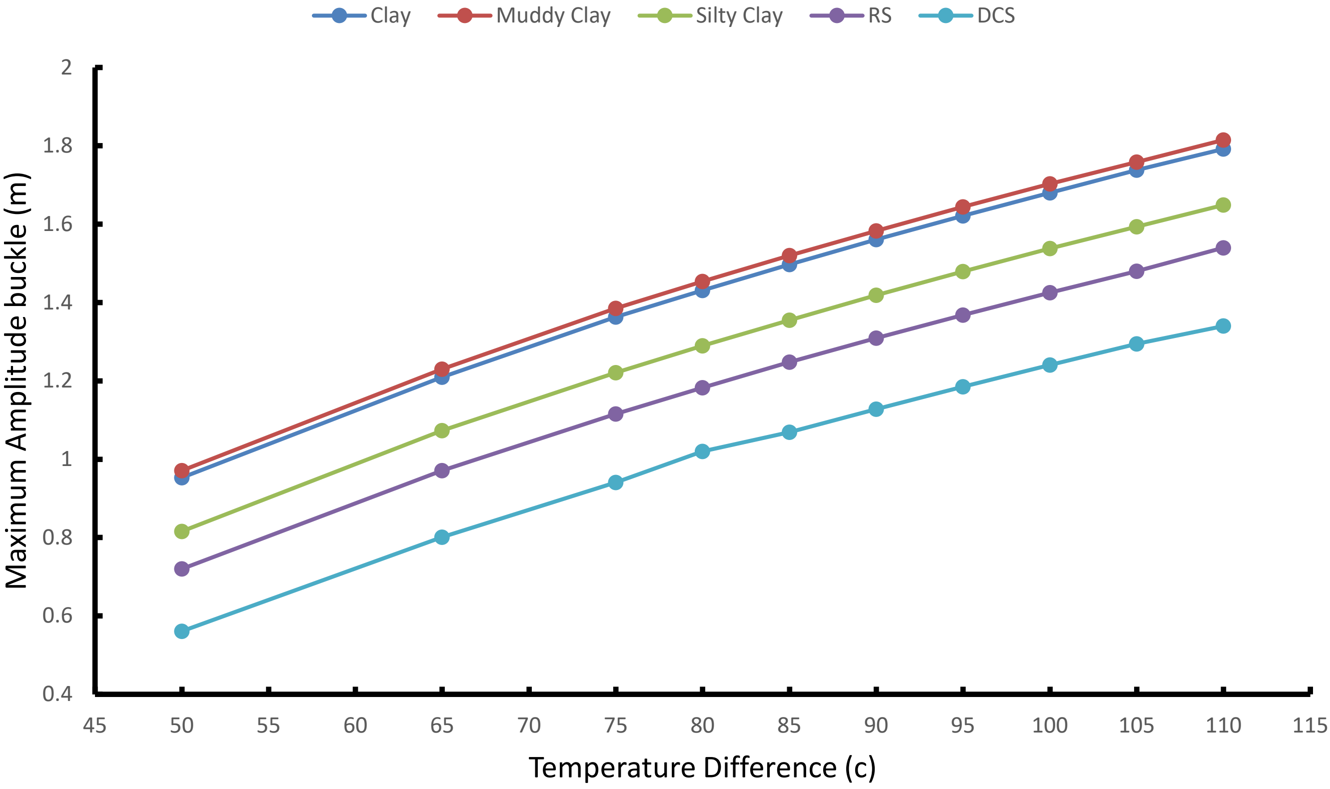

Figure 3. The maximum amplitude of upheaval buckling for different soils.

Figure 4 illustrates the critical temperature of upheaval buckling for different soils. As is shown in Figure 4, the slope of curves decreases due to increasing of friction angel of soil. In other words, the temperature difference is not effective on critical temperature in soils with high friction angel.

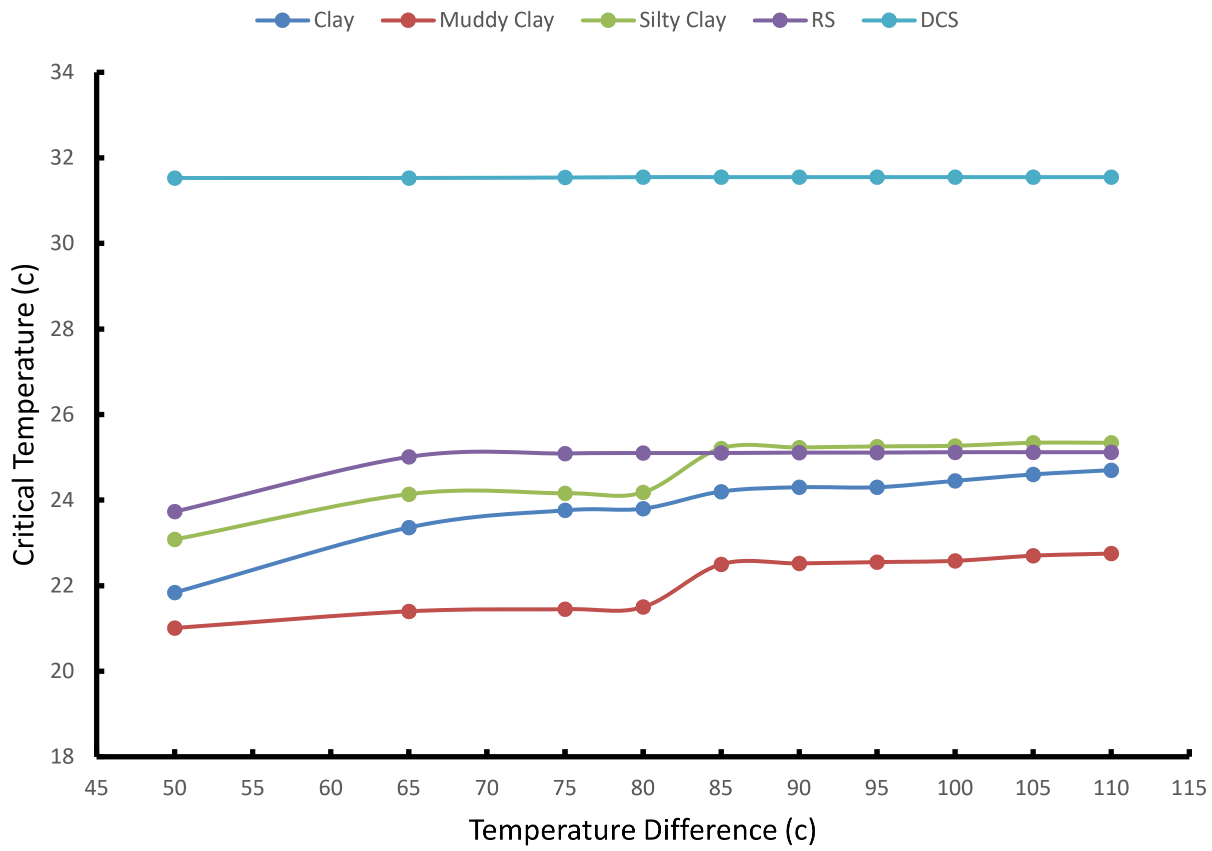

Figure 4. The critical temperature of upheaval buckling for different soils

5. Conclusions

- The critical stress increases due to the soil cohesion increasing
- Soil cohesion is more effective parameter than soil angle friction of the soil.
- The effect of difference temperature on the upheaval buckling increases due to increasing of angle friction.
- The buckle amplitude increases due to increasing of soil cohesion in clay soils and the buckle amplitude increase due to increasing of friction angel in sand soils
- The effect of temperature difference due to friction angel increasing in sandy soils is more than clayey soils
- The temperature difference is not effective on critical temperature in soils with high friction angel.

8. References

[1] Palmer AC, Ellinas CP, Richards DM, Guijt J. *Design of submarine pipelines against upheaval buckling*. In: Proceedings of 22nd annual offshore technology conference. 1990. p. 551–60.

[2] Schamin´ee PEL, Zorn NF, Schotman GJM. *Soil response for pipeline upheaval buckling analyses: full-scale laboratory tests and modelling*. In: Proceedings of 22nd annual offshore technology conference. 1990. p. 563–72.

[3] AB Taheri, M Tasdighi, M Faraji – 2019. *Reliability Analysis of Subsea Pipeline against Upheaval Buckling*, IJCOE Vol.2/No. 4/ Winter 2019 (17-23) International Journal of Coastal and Offshore.

[4] Pandey DS, Pan I, Das S, Leahy JJ, Kwapinski W (2015) *Multigene genetic programming based predictive models for municipal solid waste gasification in a fluidized bed gasifier*. Bioresour Technol 179:524–533 36. Ferreira C (2001) Gene

[5] Liu, R., Wang, W. G., and Yan, S. W. (2012). "*Engineering Measures for Preventing Upheaval Buckling of Buried Submarine Pipelines*." Applied Mathematics and. Mechanics, Springer, 36(6), 781–796.

[6] Hobbs, R. E., "*Pipeline Buckling Caused by Axial Loads*," Journal of Constructional Steel Research, Vol. 1, 1981, pp. 2-10.

[7] Zeng, X., Duan, M., Che, X., 2014. *Critical upheaval buckling forces of imperfect pipelines*. Applied Ocean Research, vol. 45, pp. 33-39.

[8] Karampour, H., Albermani, F. and Gross J. (2013), "*On lateral and upheaval buckling of subsea pipelines*", Eng. Struct., 52, 317-330.

[9] Wang, Z.; Chen, Z.; Liu, H. *Numerical study on upheaval buckling of pipe-in-pipe systems with full contact imperfections*. Eng. Struct. 2015, 99, 264–271.

[10] Zhihua Chen, Jianguo Yang, Zhenkui Wang (2020). *Numerical study on upheaval buckling for surface laid subsea pipelines with topographic step imperfection*. Applied Ocean Research. Volume 101, August 2020, 102232

[11] Nazari A, Rajeev P, Sanjayan JG (2015) *Modelling of upheaval buckling of offshore pipeline buried in clay soil using genetic programming*. Eng Struct 101:306–317

[12] Ismail, S., Najjar, S.S., and Sadek, S. (2018). *Reliability analysis of buried offshore pipelines in sand subjected to upheaval buckling*. Proceedings, Offshore Technology Conference (OTC), Houston, Texas. OTC-28882-MS.

[13] D. Suresh Kumar, D. Achani, M. R. Sunny (2019). *Influence of Wave-Induced Uplift Forces on Upheaval Buckling of Pipelines Buried in Sandy Seabeds*. Journal of Offshore Mechanics and Arctic Engineering.

[14] Bransby, M.F. and Ireland, J. 2009. *Rate effects during pipeline upheaval buckling in sand*. Proc. ICE Geotechnical Engineering 162: 247–256.

[15] S Ismail, S Sadek, S Najjar, M Mabsout. (2018). *Nonlinear finite element analysis of upheaval buckling of buried offshore pipelines in medium dense sand with fine*. Innovative Infrastructure Solutions, 2018

[16] P Vazouras, A Tsatsis, P Dakoulas - Journal of Pipeline Systems …, 2020 - ascelibrary.org. *Thermal Upheaval Buckling of Buried Pipelines: Experimental Behavior and Numerical Modelin*

[17] Wang, Z., Huachen, Z., Liu, H. and Yidu Bu, Y., 2015, "*Static and dynamic analysis on upheaval buckling of unburied subsea pipelines*", Ocean Engineering, Elsevier, 104(1 August 2015): 249-256.

[18] American society of civil engineers, *American Lifelines Alliance Guidelines for design of buried steel pipe*, July 2001.

[19] Y. Bai, Q. Bai, *Subsea Pipelines and Risers*, Elsevier, Oxford, UK, 2005.

[20] Pedersen P T, Jensen J J. *Upheaval creep of buried heated pipelines with initial imperfections* [J]. Marine Structures, 1988, 1: 11-22.

INTERNATIONAL JOURNAL OF
COASTAL & OFFSHORE ENGINEERING

IJCOE Vol.6/No. 1/Winter 2021 (37-45)

Available online at: www. Ijcoe.org

A Hydrodynamic Model of Tidal Current in the Strait of Hormuz

Mehri Fallahi[1], Masoud Torabi Azad[2*], Dariush Mansoury[3]

[1]*Graduate of Marine Physics, Faculty of Natural Resources and Marine Sciences, Tarbiat Modares University, Noor, Iran. mehri_fallahi@ut.ac.ir*

[2*] *Professor, Department of Physical Oceanography, Islamic Azad University, North Tehran Branch, Tehran, Iran. Corresponding Author (M_Azad@Iau-tnb.ac.ir)*

[3]*Assitance Prof. Department of Marine Physics, Faculty of Natural Resources and Marine Sciences, Tarbiat Modares University, Noor, Iran. mansoury@modares.ac.ir*

ARTICLE INFO

Article History:
Received: 17 Jan. 2021
Accepted: 17 Mar. 2021

Keywords:
Tidal current, Strait of Hormuz, Hydrodynamic model, Shallow water, Persian Gulf

ABSTRACT

This research presents a model for prediction of tidal currents in shallow sea areas. This hydrodynamic model is based on the solution of shallow water equations. Also contains effects of earth rotation, topographic changes, and influences of bottom friction. One of the results of solving these equations is the dispersion relation of tidal wave in the study area by which the wave number of each tidal constituent is obtainable. Finding velocity and direction of tidal currents is among other results of solving these equations. Thus, for low-amplitude waves in shallow water, the direction and velocity of tidal currents can be calculated hourly and on different days throughout the year. In order to facilitate calculations, a computer program was written in C^{++} programming software by which the tidal currents in the Strait of Hormuz have been computed at different times and the results have been diagrammed accordingly. This research indicates that the average velocity of tidal currents at the sea surface of the Strait of Hormuz during Spring tide is 0.35 m/s and ranges between 0.02 m/s - 1.7 m/s. The maximum tidal current velocities occur in shallow coastal waters, whereas in other areas these values are lower. As a result, the range of tidal currents in the Strait of Hormuz is more than that of the Persian Gulf. In addition, results showed that the tidal current direction upon entrance and exit in the Strait indicates the anticlockwise circulation of currents in the Persian Gulf.

1. Introduction

The Persian Gulf in South of Iran is connected to the Oman Sea and Indian Ocean through the Strait of Hormuz with a width of 60 km [1]. Today, this strait is one of the world's most sensitive and vital waterways. This strait is crescent-shaped 187 km long with a minimum width of around 55km from Ras Qabr al Hindijn in the North-East of Oman Peninsula to the mouth of the Gaz River in Iran and its medium width from Bandar Abbās in Iran to Ra's-e-Shurit in the North of Oman is about 187km. Its depth, due to the sharp slope of the Strait floor, varies from north to south and is about 36 m near Larak Island while in the southern coasts near Musandam Island, Oman, ranges between 180 to 200 m. The deepest point in the Strait is a pit with 223m depth, which is located 45 km North of Musandam Island.

The Strait of Hormuz as an international strait which is located between Iran and Oman is economically and strategically important. The narrowness of the Strait and existence of several islands and littoral elevations in the vicinity of marine routes make meeting the security requirements of the oil tankers and trading vessels passing through the Strait of Hormuz an internationally important issue [2]. Mehrfar etal using COHERENS model as a three dimensional hydrodynamic model to address the coastal currents in the western Persian Gulf. The obtained results suggested that Iranian northwestward coastal currents developed from January to April and experienced their maximum intensity from June to August when the rate of the surface inflow current increases through the Strait of Hormuz and the stability of the seasonal thermocline becomes gradually stronger [3].

Pous et al. (2015) concluded that thermohaline structure and circulation also vary on intraseasonal timescale, induced by the high-frequency tidal and atmospheric forcings [4]. Mehrfar et al as result of the simulation by three-dimensional hydrodynamic model (COHERENS) showed a coastal jet stream with a speed rate of 30 cm/s from May to October [5].

Le Provost suggested a model for tides at Kuwait coastlines and tidal charts and velocity diagrams of the tidal currents in the Persian Gulf were generated, accordingly. The velocity of tidal currents is mostly 20 cm/s and won't exceed more than 0.4 m/s. It is intensively influenced by the coast topography and seabed type. According to his model, all the predicted tidal currents in the medium water depth have 10 cm/s error and for the maximum tidal range, the current velocity ranges between 1-2 m/s [6].

Lardner *et al* calculated the current driven by average monthly wind drift and density gradient for the surface and bottom of the Persian Gulf. As held by this research, these currents in the Persian Gulf rotate anticlockwise and in the South-Eastern coasts have the highest values. In Iranian coasts these currents at the sea surface and at the near bottom are about 0.05 m/s and 0.04 m/s, respectively. Also, in Iranian coasts of the Persian Gulf the maximum current generated by average monthly wind drift in June at the sea surface is almost 0.085 m/s and bottom are 0.1 m/s [7].

Floating vessel registers have recorded that there are currents along the Iranian coasts towards the northwest with velocities higher than 0.1m/s. These currents tend to flow in 51.5 E ° direction (near shore) and change their direction toward the south west of the Gulf away from Iranian coasts [8, 9]. According to Torabi Azad a numerical model for mesoscale motion in the Persian Gulf presented and concluded that the average annual surface currents in the Persian Gulf are between 0.075m/s to 0.1875 m/s [10]. Based on a nonlinear barotropic model for the study of water circulation by wind pressure and tide in the Persian Gulf, was found that the velocity distribution in the Persian Gulf is in a way that water circulations with higher velocities belong to shallow areas and occur along the coastline. Also, the topographic effects of the Persian Gulf upon nonlinear barotropic currents are highly significant [11]. Teubner et al presented a model that predicts tidal elevations and current velocities which is developed and applied to the Persian Gulf. The model uses finite difference techniques applied to two- dimensional spherical coordinate equations that govern tidal movement in coastal regions. Because of the importance of the Gulf to the shipping and fishing industries, it is necessary to be able to predict tidal elevations and flows at many near shore lines. However, due to the size of the Gulf, it would be impractical to use a very fine finite difference grid over the whole Gulf. Thus, a technique is developed for nesting a fine grid within a coarse grid, so that important areas can be modeled more accurately [12].

The purpose of this study is to provide a method for computing direction and magnitude of a tidal current and describing the effect of depth upon these quantities. The effects of the rotation of the earth and bottom topography are also included in this model.

Results of this research can be used to study effect of tidal currents upon sedimentation and erosion of coastal areas and tidal rivers of the region studied. Furthermore, in designing coastal structures, taking the direction and velocity of tidal currents into consideration is important.

2. Governing Equations

The current can be described by governing equation of force per unit mass (momentum equation) and the continuity equation [13]. These equations are as follows:

$$\frac{d\vec{U}}{dt} = -\frac{1}{\rho}\nabla P - 2\vec{\Omega}\times\vec{U} + \vec{g} + \Phi \qquad (1)$$

$$\vec{\nabla}.\vec{U} + \frac{1}{\rho}\frac{\partial \rho}{\partial t} = 0 \qquad (2)$$

Where $\vec{U} = u\,\vec{i} + v\,\vec{j} + w\vec{k}$ is vector velocity , ρ is the water density, $\vec{\Omega}$ is the angular velocity vector of earth, $\vec{g}$ is acceleration of gravity, Φ is the other effective forces which is bottom friction here, ∇P is pressure gradient and d/dt is the substantial operator .Parametric condition which is characterizes shallow-water theory $(\frac{H}{L} << 1)$ in study area is considered, sea water is incompressible $(\vec{\nabla}.\vec{U} = 0)$, the fluid is barotropic $(\frac{\partial \rho}{\partial x} = \frac{\partial \rho}{\partial y} = 0)$, tidal waves are small amplitude ($\eta_o \langle\langle H_0$), the bottom friction is assumed as $\vec{\tau}_b = k'\rho_w \frac{\vec{U}}{H}$, where k' is the bottom friction coefficient and equals 75×10^{-4} m/s [11]. Also, depth variation is taking net in to consideration. In above assumptions, H is mean water depth, L is wavelength of tidal constituent, $\eta_\circ$ is the amplitude of tidal constituent, and $H_\circ$ is station depth from mean sea level.

According to the above assumptions tidal waves are small amplitude waves moving in shallow water. Further we suppose u and v (velocity components of East -West and North - South direction) are small enough that $\frac{\partial \vec{U}_H}{\partial t} >> \vec{U}_H.\nabla\vec{U}_H$. Also, from the dimensional analysis $\vec{\nabla}.\vec{U} = 0$ it can be concluded that, there is no need to calculate the vertical velocity component because it can be ignored compared with the values of other components.

The primary expansion of the governing equations is as below:

$$\begin{cases} \dfrac{\partial u}{\partial t}+\left[u\dfrac{\partial u}{\partial x}+v\dfrac{\partial u}{\partial y}+w\dfrac{\partial u}{\partial z}\right]-fv=-\dfrac{1}{\rho}\dfrac{\partial \tilde{P}}{\partial x}-\dfrac{k'}{H_0}u \\ \dfrac{\partial v}{\partial t}+\left[u\dfrac{\partial v}{\partial x}+v\dfrac{\partial v}{\partial y}+w\dfrac{\partial v}{\partial z}\right]+fu=-\dfrac{1}{\rho}\dfrac{\partial \tilde{P}}{\partial y}-\dfrac{k'}{H_0}v \\ \dfrac{\partial w}{\partial t}+\left[u\dfrac{\partial w}{\partial x}+v\dfrac{\partial w}{\partial y}+w\dfrac{\partial w}{\partial z}\right]=-\dfrac{1}{\rho}\dfrac{\partial \tilde{P}}{\partial z}-g \end{cases} \tag{3}$$

Where f is Coriolis parameter, (u, v, w) are the velocity components in the eastward (x), northward (y) and vertical (z) directions respectively. From the z component of above equations (3) the pressure relation can be obtained in terms of the depth and from that the pressure displacement can be related to the displacement of oscillation dimension of the tidal constituents. Considering the above assumptions and explanations, a partial differential equation system is obtained as follows:

$$\begin{cases} \dfrac{\partial u}{\partial t}-fv=-g\dfrac{\partial \eta}{\partial x}-\dfrac{k'}{H_0}u \\ \dfrac{\partial v}{\partial t}+fu=-g\dfrac{\partial \eta}{\partial y}-\dfrac{k'}{H_0}v \end{cases} \tag{4}$$

The Solutions (4) maybe sought in form of a plane wave. i.e [14].

$$\eta=\eta_o\cos(kx+ly-\sigma\cdot t) \tag{5}$$

Where η is the tide height due to a particular constituent and its phase is $kx+ly-\sigma.t$, $\vec{K}=k\hat{\vec{i}}+l\hat{\vec{j}}$ is wave propagation vector, k and l are wave vectors of each tidal constituent in North - South and East –West directions, respectively. K is wave number vector; σ is the angular velocity of the tidal constituent.

If (5) is substituted in (4) after some manipulation, yields the dispersion relation for each tidal constituent is as follows:

$$\sigma^2=\left(\frac{k'^2}{H_0^{\,2}}+f^2\right)+C_0^2K^2 \tag{6}$$

Here $C_\circ=\sqrt{gH_\circ}$ is the phase velocity. The velocities u and v can be found in terms of η from the solution of differential equation system (4):

$$u=\frac{-g\eta_0k\sigma\left(f^2-\sigma^2+\dfrac{k'^2}{H_\circ^{\,2}}\right)+\dfrac{2k'}{H_\circ}\sigma(gfl\eta_0+gk\eta_0\dfrac{k'}{H_\circ})}{\left(f^2-\sigma^2+\dfrac{k'^2}{H_\circ^{\,2}}\right)^2+\dfrac{4k'^2}{H_\circ^{\,2}}\sigma^2}\cos(kx+ly-\sigma.t)$$
$$+\frac{-g\eta_0k\sigma^2\dfrac{2k'}{H_\circ}+(gfl\eta_0+gk\eta_0\dfrac{k'}{H_\circ})\left(f^2-\sigma^2+\dfrac{k'^2}{H_\circ^{\,2}}\right)}{\left(f^2-\sigma^2+\dfrac{k'^2}{H_\circ^{\,2}}\right)^2+\dfrac{4k'^2}{H_\circ^{\,2}}\sigma^2}\sin(kx+ly-\sigma.t) \tag{7}$$

$$v=\frac{-g\eta_0l\sigma\left(f^2-\sigma^2+\dfrac{k'^2}{H_\circ^{\,2}}\right)+\dfrac{2k'}{H_\circ}\sigma(-gfk\eta_0+gl\eta_0\dfrac{k'}{H_\circ})}{\left(f^2-\sigma^2+\dfrac{k'^2}{H_\circ^{\,2}}\right)^2+\dfrac{4k'^2}{H_\circ^{\,2}}\sigma^2}\cos(kx+ly-\sigma.t)$$
$$+\frac{g\eta_0l\sigma^2\dfrac{2k'}{H_\circ}+(-gfk\eta_0+gl\eta_0\dfrac{k'}{H_\circ})\left(f^2-\sigma^2+\dfrac{k'^2}{H_\circ^{\,2}}\right)}{\left(f^2-\sigma^2+\dfrac{k'^2}{H_\circ^{\,2}}\right)^2+\dfrac{4k'^2}{H_\circ^{\,2}}\sigma^2}\sin(kx+ly-\sigma.t) \tag{8}$$

The velocity component is parallel to wave propagation vector $u_{||}$ and velocity component is perpendicular to the wave propagation vector $u_{\perp}$ are as follows:

$$u_{||}=\frac{-g\eta_0\sigma\left(f^2-\sigma^2+\dfrac{k'^2}{H_\circ^{\,2}}\right)+\dfrac{2k'}{H_\circ}\sigma(g\eta_0\dfrac{k'}{H_\circ})}{\left(f^2-\sigma^2+\dfrac{k'^2}{H_\circ^{\,2}}\right)^2+\dfrac{4k'^2}{H_\circ^{\,2}}\sigma^2}\times K\times\cos(kx+ly-\sigma.t)+$$
$$\frac{g\eta_0\sigma^2\dfrac{2k'}{H_\circ}+g\eta_0\dfrac{k'}{H_\circ}\times\left(f^2-\sigma^2+\dfrac{k'^2}{H_\circ^{\,2}}\right)}{\left(f^2-\sigma^2+\dfrac{k'^2}{H_\circ^{\,2}}\right)^2+\dfrac{4k'^2}{H_\circ^{\,2}}\sigma^2}\times K\times\sin(kx+ly-\sigma.t) \tag{9}$$

$$u_{\perp}=\frac{-\dfrac{2k'}{H_\circ}\sigma.g.f.\eta_0}{\left(f^2-\sigma^2+\dfrac{k'^2}{H_\circ^{\,2}}\right)^2+\dfrac{4k'^2}{H_\circ^{\,2}}\sigma^2}\times K\times\cos(kx+ly-\sigma.t)+$$
$$\frac{-g.f.\eta_0\left(f^2-\sigma^2+\dfrac{k'^2}{H_\circ^{\,2}}\right)}{\left(f^2-\sigma^2+\dfrac{k'^2}{H_\circ^{\,2}}\right)^2+\dfrac{4k'^2}{H_\circ^{\,2}}\sigma^2}\times K\times\sin(kx+ly-\sigma.t) \tag{10}$$

It is convenient to replace

$$\eta=f'\eta_0\cos\left(\frac{2\pi}{T}t+g'+V_\theta\right).$$

in (5) and applying in (9) and (10) [15]. Where f' is knot factor, whose value for each day should be taken from tide tables and can be used as a coefficient for the correction of the amplitude, V_θ is the astronomical argument which is printed for important constituents such as Admiralty Tide Table [16]. T is period of tidal constituent, g' is the phase delay which is calculated regarding the tidal observations.

The utilized depth values are extracted from the depth maps of the Geography Organization of the Army and the amplitude and Greenwich phase delay of each station are extracted from the co-tidal maps of the Cartography Organization of Iran [17]. In order to made the calculations a computer program was written in C^{++} and was run in two stages:

A) At the first stage, by the use of the instructions available in Admiralty Tide Tables, a computer program is written to help interpolate the knot factor and astronomical arguments for each constituent in the related region [16, 17]. The output of the present program will be an input file for the second program.

B) At the second stage, by the use of what we described before a program is written whose output will be the velocity and direction of the tidal flow.

3. Results and Discussion

In order to verify the equation result and also output of current velocity which has determined by computer, the output of this program is going to compare and study with the existent data. This study was done in two steps:

a) Prediction of current in a station in the Strait of Hormuz and comparison with the field study measurements.

b) Prediction of current in two stations with different depths and compare the results by tidal theory. Location of study stations are presented in figure 1.

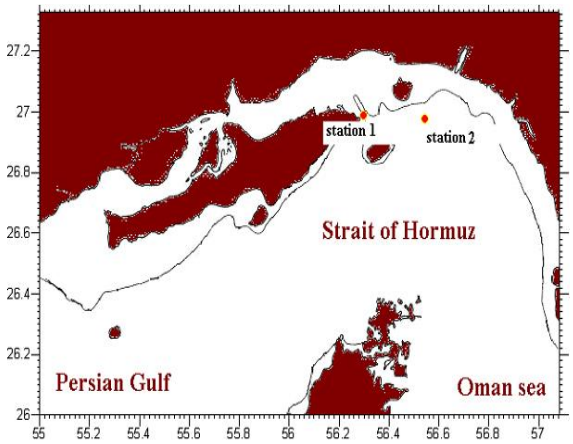

Figure 1. Position of Strait of Hormuz and study stations

1-3 Prediction of current at a station in Strait of Hormuz in accordance with the field Current measurement

For this step, station 1 were considered in the Strait of Hormuz, then the output mean velocity of prediction program, with the mean velocity of field Current measurement in this station has been compared. It's necessary to mention those current meters are floated half meter from the water surface (Table 1). Program outputs with the mean velocity which obtained from computer program running are shown in Table 2. The mean velocities in table 1 and 2 have been compared with each other. It is remarkable that there is a significant difference between two mean velocity measures in these stations which caused by current meters floating or currents arise by wind, currents arise by different density and rivers discharge in this area. The difference between two average velocities can be due to the instrumental errors in field measurements or the approximations used in the calculation of tidal currents.

2-3 Prediction of current in stations with variation depths and results comparison by tidal theory

In this step, current variations with depth in stations 1 and 2 near the shore has been studied, the depth was less than 20m. In other hand the output program verify with the tidal theory has been checked (Table 3and 4).

Table 1. Information of current monitoring

Time specification of current metering	Longitude (Deg)	Latitude (Deg)	Velocity (cm/s)
6 Feb 2006, 9 A.M. total time 15 hour	56.19 E	26.39 N	14.93

Table 2. Prediction of tide characteristics in station 1

Longitude (Deg) :56.18 E		Latitude (Deg) :26.41 N		Depth (m) :85.73		Velocity (cm/s) :16.58	
M2		S2		K1		O1	
Amplitude(m)	Phase(deg)	Amplitude (m)	Phase(deg)	Amplitude (m)	Phase(deg)	Amplitude (m)	Phase(deg)
0.71	313.5	0.25	357	0.25	75	0.2	69

Table 3 Tide characteristics of station 1

Tidal constituent	Amplitude (m)	Greenwich delay phase (Deg)
M_2	0.93	312.56
S_2	0.3	356.59
K_1	0.3	69.31
O_1	0.2	56.94

Table 4. Tide characteristics of station 2

Tidal constituent	Amplitude (m)	Greenwich delay phase (Deg)
M_2	0.91	309.33
S_2	0.3	342.07
K_1	0.3	64.75
O_1	0.2	50.25

Characteristics which mentioned in Table 3 are the inputs of program. Current for 25th of January 2016 at surface of water is predicted. So, the magnitude and current direction can be individually studied. Figures 2 and 4 shows time variation of current magnitude respectively at two stations 1 and 2 that predicted by the model. It is expected that as tides are due to a harmonic force, changes in water height as well as changes in current velocity are harmonic. Figures 3and 5 shows time variation of current direction respectively at two stations 1 and 2 that predicted by the model.

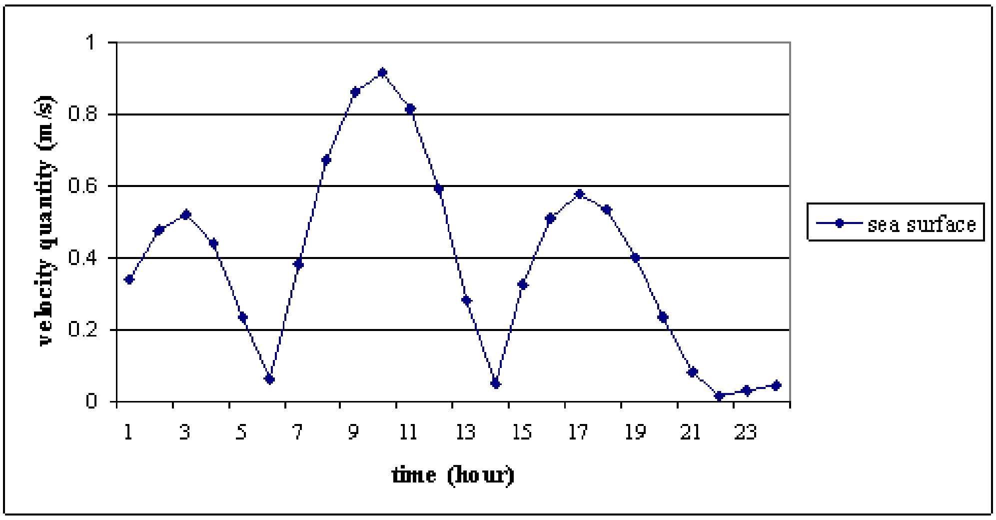

Figure 2. Time variations of current magnitude at sea surface (station 1)

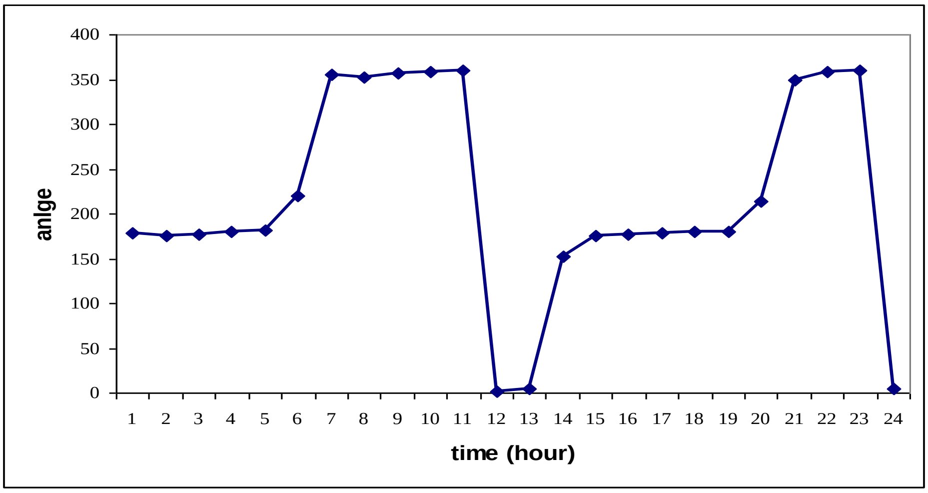

Figure 3. Time variation of Current direction at sea surface (station 1)

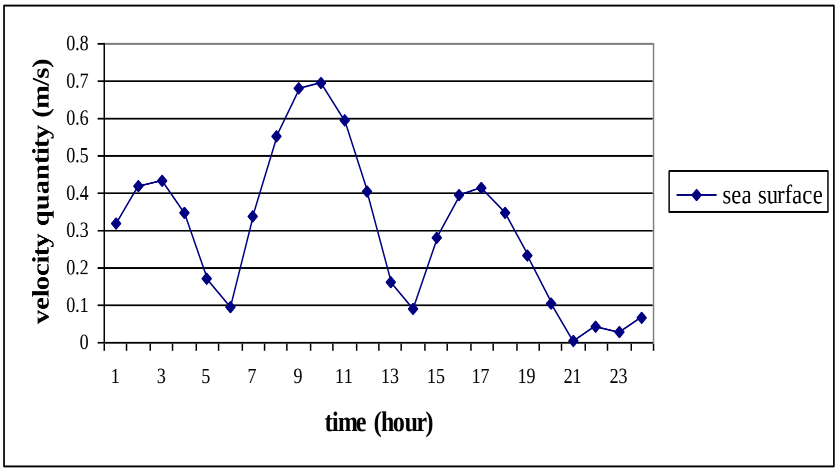

Figure 4. Time variations of current magnitude at sea surface (station 2)

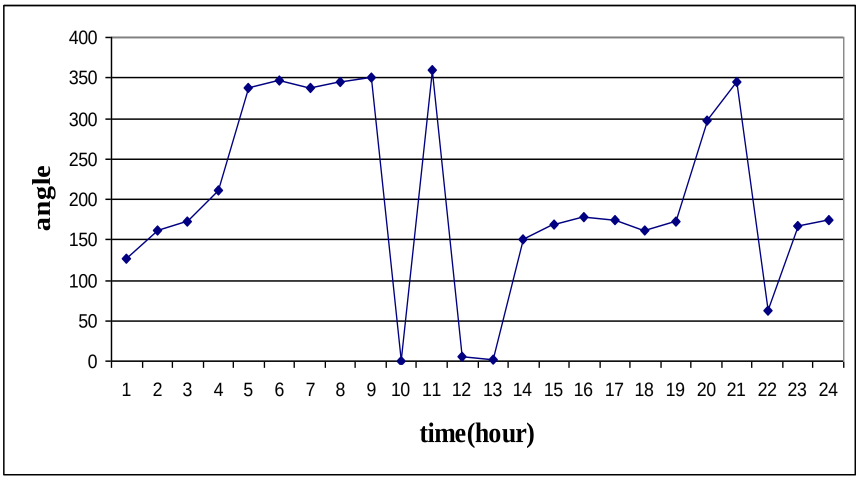

Figure 5. Time variation of Current direction at sea surface (station 2)

It is considering that current vector is parallel with the strait axis or west - east axis in maximum hours of a day and also current direction is changing when spring tide shift to neap tide. If this program runs for deeper stations, it is found that in these stations, has a high difference between tidal theory and model results. Thus, by calibration in selected stations and change of friction coefficient, it can be possible model results approach to result of theory.

Results of this model have been shown a good precision of tidal currents at upper layer and sea surface. Subsequently, by this program the tidal current for the surface of the Strait of Hormuz will be predicted. For this purpose, an area measuring 200 km in length and 100 km in width was chosen so that it encompassed the Strait of Hormuz. Then, at every five kilometers a station was chosen and the characters of each station including the station's longitude and latitude, depth and tidal characteristics were saved in a file which later served as the input of the computer program. The output of the compiled program was made ready by Excel software, so to use of Surfer software we can draw vector field of tidal current. Tidal current vectors at water surface in several times on 27^{the} June 2017 are shown in figures (6) to (9).

One may notice that 27^{the} June 2017 is beginning time of lunar moon which maximum tide happens, so it is expected that the maxima tidal currents exist in this time. Also, the program was run in each 6 hours according to semidiurnal period of tide.

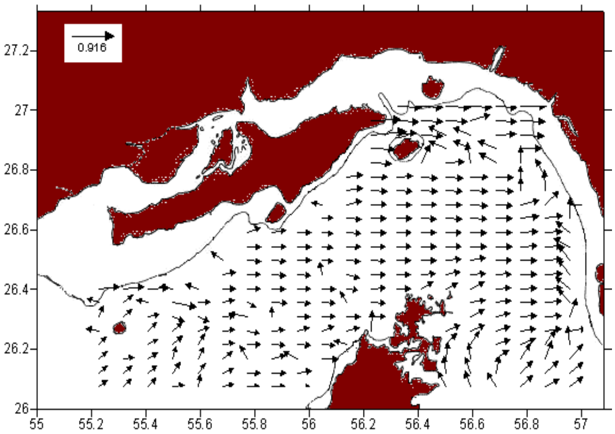

Figure 6. Tidal current vectors (m/s) at 6:00 a.m., 27.6.2017

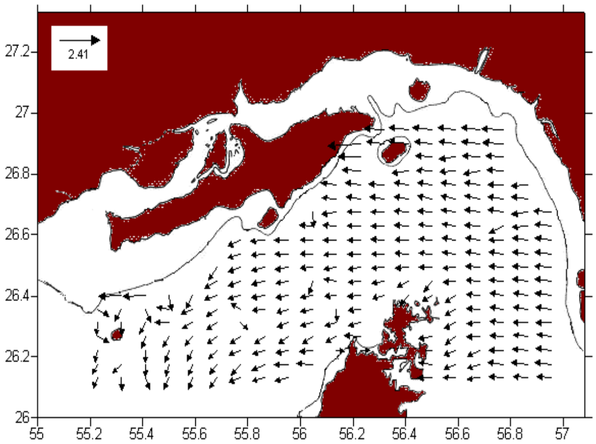

Figure 7. Tidal current vector (m/s) at 12:00 p.m., 27.6.2017

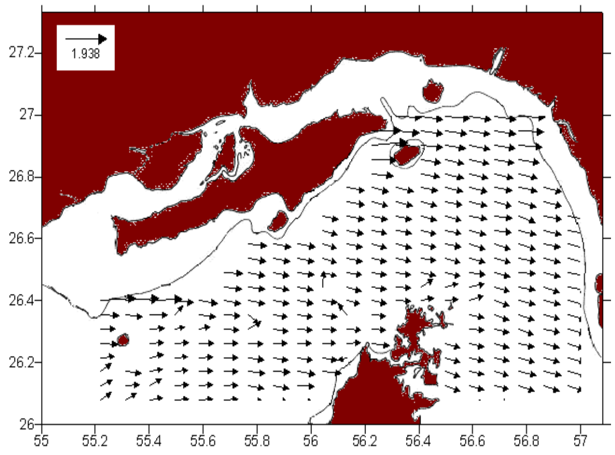

Figure 8. Tidal current vector (m/s) at 18:00, 27.6.2017

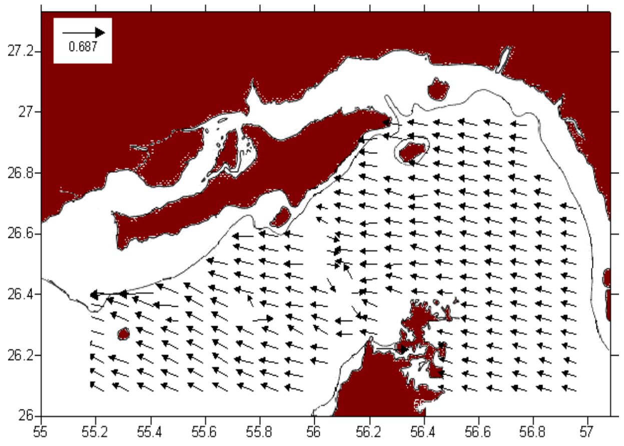

Figure 9. Tidal current vector (m/s) at 23:00, 28.6.2017

The predicted of tidal currents indicates that when the flow enters the Persian Gulf through the Strait of Hormuz, it deviates towards North-West and during leaving the Gulf it is flowing toward North-West. This result is compatible to Raees al-Sadat and which are consistent with the results of Sabbagh Yazdi and Mashayekh Poul [1, 18 and 19].

Tidal currents upon leaving the Strait of Hormuz and when reach to shallow Eastern regions and return coastal currents, has flow almost along the coastline. This result is also compatible with research done by Khaleghi Zavareh in 1994 [11].

Both from the predicted values and the figure of tidal currents, it is deducted that stronger currents are in shallow areas, a fact which had verified by the relevant previous studies. Mean velocity of tidal currents at the surface of Strait of Hormuz and during the first 12 hours of a month is 0.35 m/s and in average its velocity varies between 0.02m/s to 1.7 m/s. The maximum of these current velocities occur in shallow coastal areas. Based on researches done in the Persian Gulf; currents vary from 0.0017m/s to 0.15 m/s [10, 20]. Therefore, the range of velocity of tidal currents in the Strait of Hormuz is higher than that of the Persian Gulf. Furthermore, it is observed that at the center of the Strait of Hormuz tidal currents are parallel with the Strait's axis and velocity vectors are also parallel with each other. The analysis of current data shows that semi diurnal tide is the main constituent. Hence this component was removed to consider the residual components due to wind and buoyancy typical deep tidal current is about 30-40 cm/s while the surface tidal current can reach 112 cm/s and the residual current range from 4.5-7.6 cm/s. In research Stations of Strait of Hormuz, residual current magnitude in winter 5 cm /s is smaller than the spring rate 8 cm/s. The effects of tide on currents in the Strait of Hormuz at consider stations have been shown. By moving from the center towards the north coasts of Strait of Hormuz increasing the speed of tidal currents._Residual currents are influenced by wind and density differences and moves from the north of Strait of Hormuz into the Persian Gulf. This current movement speed is lower in winter than in spring. Lardner and et al the monthly mean wind driven current and density gradient current was investigated for Persian Gulf and speed of currents close to the coast of Iran at surface 0.05 m/s to about 0.04 m/s in bottom was estimated [7].

4. Conclusions

A model has been made to predict the tidal currents in the Strait of Hormuz. This model uses the shallow water equations and assumes that tidal waves are small amplitude waves. The solutions of governing equations sought in form of a plane wave, and this leads to dispersion relation for each tidal constituent. The model is run for magnitude and direction of tidal currents in Strait of Hormuz in day that maximum amplitude of tide happens in 2017. Model results show that mean values of tidal currents at sea surface varies between 0.02 m/s to 1.7 m/s.

Current vectors being parallel to the flow axis in the center of Strait of Hormuz indicate that tidal currents in the Strait have similar characteristics with currents in narrow channels. It is found that of this study, maximum tidal currents are related to coastal areas and the tidal circulation in the Strait of Hormuz is anticlockwise.

5. References

1-Raees al-Sadat, S. M. Bannazadeh.M.R, Bidokhti.A.A., (2003), *A model for Circulation in the Persian Gulf*, NIVAR Journal (In Persian), No. 50 & 51, p. 29.

2- Bakhtiari, M., (1990), *Comprehensive Guidebook of Iran*, vol. 22, Hormozgan Province, Gitashenasi Publications, Tehran, Iran

3-Mehrfar.H, Torabi Azad.M, lari.K, Bidokhti.A.A.,(2020), *A numerical simulation case study of the coastal currents and upwelling in the western Persian Gulf*, Journal of Ocean Engineering and Science, Vol 5. Issue 4, p.323-332, doi.org/10.1016/j.joes.2019.12.005

4-Pous S., Lazure P., Carton X.,(2015), *A model of the general circulation in the Persian Gulf and in the Strait* *of Hormuz: Intraseasonal to interannual variability*, Continental Shelf Research Vo. 94 p.55-70, http://dx.doi.org/10.1016/j.csr.2014.12.008

5-Mehrfar.H, Torabi Azad.M, lari.K, Bidokhti.A.A.,(2020), *Seasonal variations of the coastal currents and eddies in the Persian Gulf ; A Numerical case study*, Marine Technology Society Journal,Vol 54,No 1,p. 44-52, doi.org/10.4031/MTSJ.54.1.4

6-Le Provost, C., (1984), *Models for Tides in the KAP (Kuwait Action Plan) Region*, UNESCO Report of Marine Science, Vol. 24.

7-Lardner R. W., A. H. Al-Rabeh, Gunay, N., Hossain, M., Reynolds, R. M. and Lehr, W. J., (1993), *Computation of the Residual Flow in the ROPME sea area using the Mt- Mitchell data and the KFUPM/RI hydro dynamical models*, Final reports of the Mt-Mitchell cruise the ROPME sea area, p. 116-150.

8-Hunter, J.R., (1982), *The physical oceanography of the Persian Gulf: a review and theoretical interpretation of previous observations*, Marine Environments and pollution, Proceedings of the first Persian Gulf Conference on Environments and Pollution, Kuwait, 7-9 February, p. 1-23.

9-Chao, S.Y., Kao, T.W. and Al-Hajri, K.R.,(1992), *A numerical investigation of circulation in the Persian Gulf*, Journal of Geophysics Research, 97,p. 11219-11236

10-Torabi Azad, M.,(1999), *A Numerical Model for Mesoscale Motions in the Persian Gulf, Ph.D Dissertation, Islamic Azad University Science & Research Branch*, Tehran, Iran.

11-Khaleghi Zavareh, H., (1994), *Development of a Nonlinear Barotropic model of the wind driven circulation for Persian Gulf*, NIVAR Journal (In Persian), No. 21, p. 53

12-Teubner, M.D, Najafi, H.S., Noye, B.J. and Rasser, P.E., (1999), *Modeling Tides in the Persian Gulf using Dynamic Nesting, Modeling Coastal Sea Process*, World Scientific Publishing co.

13-Knauss John A., (1997), *Introduction to Physical Oceanography*, Prentice Hall Inc, Chp10.

14-Pedlosky, J., (1987), Geophysical Fluid Dynamics, Second Edition, Springer Velarg, New York, U.S.A.

15-Foreman.M.G.G., (1996), *Manual for tidal currents analysis and prediction*, Pacific Marine Science Report 78-6, Institute of ocean sciences, Patricia Bay, Sidney

16- *Admiralty Charts, Persian Gulf*, (2016), principal Harmonic Constituent.

17-*Cartography Organization of Iran's Data*,(2016), Use have been made of the tidal data and also Admiralty tide tables available in this organization,Tehran, Iran.

18-Sabbagh Yazdi, S.-R., Zounemat-Kermani, M., Kermani, A., (2007), *Solution of depth-averaged tidal currents in Persian Gulf on unstructured overlapping finite volumes*, International Journal for Numerical Methods in Fluids, Volume 55, Issue 1, p. 81–101.

19-Mashayekh Poul.H, (2016), *Modelling tidal processes in the Persian Gulf - With a view on Renewable Energy*, Ph.D Dissertation, Institute of Oceanography University of Hamburg, 115

20-Reynolds, M.R. ,(1993), *physical oceanography of the Gulf, Strait of Hormuz, and the Gulf of Oman- Results from the Mt. Mitchell expedition* ,Marine Pollution .Bull.27,p.35-39

INTERNATIONAL JOURNAL OF
COASTAL & OFFSHORE ENGINEERING

IJCOE Vol.6/No. 1/Winter 2021 (47-53)

Available online at: www. Ijcoe.org

Numerical modelling the effect of wind on Water Level and Evaporation Rate in the Persian Gulf

Omid Mahpeykar[1*], MohammadReza Khalilabadi[2]

[1*] *Ph.D. student, Khorramshahr university of marine science and technology, Omidd8@gmail.com*
[2] *Assistant professor, Faculty of Naval Aviation, Malek-Ashtar University of Technology, Khalilabadi@mut.ac.ir*

ARTICLE INFO

Article History:
Received: 04 Feb. 2021
Accepted: 03 Apr. 2021

Keywords:
Persian Gulf
Water Level
Wind
Numerical modelling

ABSTRACT

Evaporation is one of the most important quantities in the marine climate, and in the Persian Gulf, this parameter makes it one of the saltiest free waters in the world. Evaporation estimation is essential for water balance studies, irrigation, and land resource planning. Persian Gulf is known as shallow water and therefore has a high temperature in summer, which increases the rate of evaporation and high salinity up to 50PPT. In this study, the effect of wind speed and direction on the rate of evaporation in the Persian Gulf, assuming that there is no water inflow into the basin, was investigated using numerical modelling. Mike model is based on the three-dimensional solution of the Navier Stokes equations, assumption of incompressibility, Boussinesq approximation, and hydrostatic pressure. The effects of wind on evaporation at four different wind speeds and four different wind directions have been investigated. Results show the wind direction has little effect on evaporation, but wind speed has significant changes on evaporation rate and water level, and these changes are nonlinearly related to water temperature so that in summer the evaporation rate increases faster with increasing temperature.

1. Introduction

Evaporation estimation is essential for water balance studies, irrigation, and land resources planning. There are different methods for estimating and measuring evaporation rates. These methods can be divided into several categories: 1- Experimental [1], 2- Water budget [2], 3- Energy budget [3], 4- Mass transport [4], 5. Combined [5]. Studies show that meteorological factors such as pressure gradient, wind speed, and temperature have the greatest effect on evaporation. The evaporation rate is calculated using the Bulk method as follows [6]:

$$E = K(e_w - e_a)w \tag{1}$$

Where E is the evaporation in mm/day, K = 10.137 × 10-2, e_w is the saturated vapor pressure at water temperature, and e_a is the vapor pressure at air temperature. These two parameters are calculated as follows [7]:

$$e_a = 6.112 \times \exp\left(\frac{17.67T}{273.15+T}\right) \tag{2}$$

$$e_w = e_a \times relative\ humidity \tag{3}$$

The Persian Gulf is semi-enclosed and shallow water that results from continuous deposition in a once-deep basin [8]. The length of the Persian Gulf is about 1000 km in the northwest-southeast direction, the maximum width is 338 km and the minimum width is 56 km in the Strait of Hormuz, which has an approximate area of 3.39×105 Km2. The coastal topography of the Persian Gulf on the periphery of the countries shows the following features: While the coasts of Iran are mountainous, the coasts of the Arab countries are mostly flat deserts, except around the Strait of Hormuz, which has a high and rocky topography on the Musandam Peninsula. Depth measurement of the Persian Gulf also shows asymmetry, so that a depression extends from the Strait of Hormuz to the northwest along the coast and a shallow coastal area with a depth of fewer than 20 meters in the southwest of the Persian Gulf (Figure 1). With an average depth of 35 meters and a maximum depth of 110 meters in the Strait of Hormuz, the Persian Gulf bed falls quickly from the Strait of Hormuz without any significant effects and reaches a depth of 2000 meters in 200 kilometers inside the Oman Sea [9].

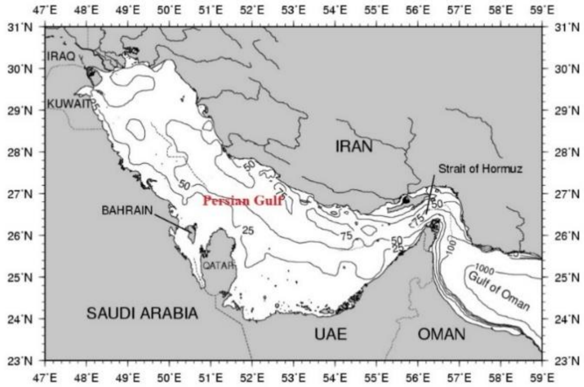

Figure 1. Map of the Persian Gulf region

Persian Gulf water is one of the saltiest bodies of water in the world's oceans. This water comes out of the deep areas of the Strait of Hormuz and creates a kind of reverse estuaries due to the way water is exchanged. As the water leaves the strait, less saline water enters the Persian Gulf from the Oman Sea, diluting it. The outflow waters of the Persian Gulf reach a neutral buoyancy level at depths of 200 to 350 m and are released horizontally as the saltiest groundwater in the North Indian Ocean [10, 11, 12, 13]. The waters of the Red Sea and the Persian Gulf together provide high salinity intermediate waters at 900 m above the Indian Ocean [11]; thus, similar to other sub-marine and marginal seas such as the Red and Mediterranean Seas, the Persian Gulf, as a dense basin, is responsible for supplying subsurface saline waters in the open oceans.

Due to the region's high air temperatures and its arid climate, evaporation in the Gulf is high. Previous studies on heat fluxes in the Persian Gulf provide mixed answers for the amount as well as times of maximum and minimum evaporation rates in the Gulf. There are several studies of heat fluxes in the Persian Gulf. Privett reported maximum evaporation rates of 0.0036 Sv (1 Sv = 106 m3/s) in December and minimum rates of 0.00049 Sv in May with an annual-mean evaporation rate of 0.011 Sv [14]. Hastenrath and Lamb used a climatic atlas of the Indian Ocean and estimated monthly evaporation rates for the Persian Gulf [15]. The values as well as the time of occurrence of maximum and minimum evaporation estimated by these authors are in agreement with Privett. According to these authors, evaporation of 29.3 cm/month occurs in June and a minimum value of 8.1 cm/month is found in February, with an annual mean of 20.16 cm/month for that area. Xue and Eltahir estimate that the Gulf acts as a sink of heat for the atmosphere (+3 W/m2) and the annual evaporation from the Gulf is 1.84 m/yr [16].

It is difficult to consider all the components affecting evaporation in the hydrological cycle, to study their effects and the extent of the impact of each. In this study, the effect of wind speed and direction on the rate of evaporation in the Persian Gulf is investigated, assuming that there is no water inflow into the basin.

Because observational data are limited, previous estimates of water and heat budgets are highly uncertain. This large defect has attracted the attention of climatic and hydrological studies. The values of previous studies related to surface heat flux from incoming flux + 66 W/m2 to the lost flux-21 for the Persian Gulf have been reported. This uncertainty leaves many questions and causes the water exchange rate to be reported from 1.4 to 2.1 m/year. As shown in relation (1), one of the factors affecting evaporation is wind speed, which changes the rate of evaporation linearly, but when these changes are accompanied by a change in temperature according to relations (2) and (3), it will become nonlinear. In other words, the effect of wind in different seasons causes the evaporation rate to be different. In this study, the effect of wind speed and direction on the change of water level and evaporation rate due to seasonal changes in temperature will be investigated.

The evaporation rate directly affects the salinity of the Persian Gulf, which is one of the most important and influential parameters in the circulation of the Persian Gulf. The circulation in the Persian Gulf is a cyclonic circulation that is primarily caused by the density difference between the Gulf of Oman and the Persian Gulf, and this density difference is affected by the salinity difference between the two basins [17, 18, 19]. In oceanic numerical modeling, evaporation is usually considered as an input in the form of latent heat flux. Therefore, accurate determination of this parameter leads to more accurate modeling results. On the other hand, direct measurement of evaporation is impossible due to the exchange of Persian Gulf water with the Oman Sea and the data of meteorological stations near the Persian Gulf cannot be cited because the mechanism of measuring evaporation in these stations is different from how seawater evaporates, And only perhaps can seasonal variations of this data be cited under certain conditions.

2. Method

Equations In this research, JEBCO topography data with an accuracy of about one kilometer have been used. Then, in the Mesh Generator section of Mike software, an irregular and triangular computational network of 10699 elements and 6196 nodes were created (Figure 2). The boundaries of the study area were considered as land boundaries to prevent water from entering the basin. Therefore, the equations are solved by considering the heat-salinity forces and wind stress and without considering the tide. In models that are implemented with one of the finite element numerical methods or finite difference, the stability and convergence of the model depend on characteristics such as time step, the distance of network nodes, etc. In the hydrodynamics module of the MIKE program, the CFL condition is also used for stability, which is as follows:

$$CFL = \left(\sqrt{gh} + |u|\right)\frac{\Delta t}{\Delta x} + \left(\sqrt{gh} + |v|\right)\frac{\Delta t}{\Delta y} \qquad (4)$$

Because the network used in the model is an unstructured network, the dimensions of each network cell are different, so the time step used to calculate the CFL value is between 0.01 and 30 seconds. Also, the critical CFL value is set to 0.8, and if the calculated CFL values for each of the network cells exceed this value, the model will crash. It should be noted that the critical CFL value is based on the default of the model and its value is determined by considering the highest flow velocity that can be observed in the seas. If the CFL value for all cells is less than 0.8 during the model run, the stability condition is met.

Mike model uses the following equations to calculate evaporation. The latent heat can be written as [20]:

$$q_v = -P(a_1 + b_1 W_{2m}) \cdot \left(\frac{\exp\left(K\left(\frac{1}{T_k} - \frac{1}{T_{water}+T_k}\right)\right)}{T_{water} + T_k} - \frac{R.\exp\left(K\left(\frac{1}{T_k} - \frac{1}{T_{air}+T_k}\right)\right)}{T_{air} + T_k} \right) \tag{5}$$

Where P_v=4370 J.°K/m^3, K=5418°K, R is relative humidity, T_k=273.15°K is the temperature at 0°C, T_{water} and T_{air} are the temperatures water and air respectively. During cooling of the surface the latent heat loss has a major effect with typical values up to 100 W/m^2.

The wind speed, W_2, 2 m above the sea surface is calculated from the wind speed, W_{10}, 10 m above the sea surface using the following formula: assuming a logarithmic profile the wind speed, u(z), at a distance z above the sea surface is given by

$$u(z) = \frac{u_*}{\kappa} \log\left(\frac{z}{z_0}\right) \tag{6}$$

Where u_* is the wind friction velocity, z_0 is the sea roughness and κ=0.4 is von Karman's constant. u_* and z_0 are given by

$$z_0 = z_{Charnock} u_*^2 / g \tag{7}$$

$$u_* = \frac{\kappa u(z)}{\log\left(\frac{z}{z_0}\right)} \tag{8}$$

Where $z_{charnock}$ is Charnock parameter. The default value is $z_{charnock}$=0.014. The wind speed, W_2, 2 m above the sea surface is then calculated from the wind speed, W_{10}, 10 m above the sea surface by solving Eq. (7) and Eq. (8) iteratively for z_0 with z=10m and u(z)=W_{10}. Then W_2 is given by

$$W_2 = W_{10} \frac{\log\left(\frac{2}{z_0}\right)}{\log\left(\frac{10}{z_0}\right)} \qquad W_{10} > 0.5 m/s \tag{9}$$

$$W_2 = W_{10} \qquad W_{10} \leq 0.5 m/s$$

The heat loss due to vaporization occurs both by wind driven forced convection by and free convection. The effect of free convection is taken into account by the parameter a_1 in Eq. (5). The free convection is also taken into account by introducing a critical wind speed $W_{critical}$ so that the wind speed used in Eq. (9) is obtained as W_{10}=max(W_{10},$W_{critical}$). The default value for the critical wind speed is 2 m/s.

Table 1 shows the different scenarios that have been considered. The effects of wind on evaporation at four different velocities and four different wind directions have been investigated. The accuracy of the model results is checked based on the change of water level under standard conditions. The prevailing wind in the Persian Gulf, according to most studies [21, 22], is the Shamal wind, which blows from the northwest during the year, and the speed of 5 meters per second is the average speed that can be considered for this wind during a year. Implementation of the model taking into account these conditions should lead to a reduction of 1.3 to 2.2 meters of water level due to evaporation in the Persian Gulf, as mentioned in previous studies [22]. Therefore, if under these special conditions the amount of evaporation or reduction of Persian Gulf water is in this range, we can ensure the accuracy of the results obtained. Of course, it must be said that because evaporation is usually one of the input parameters of models, in some modelling is considered as a variable parameter; That is, it must be corrected to lead to temperature and salinity output with minimal error.

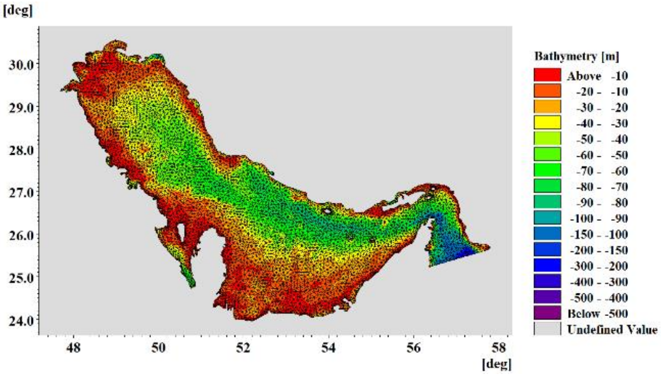

Figure 2. The network used in the model

Table 1. Different scenarios to investigate the effect of wind on evaporation

Dependent Variable	**Number of Test**	**Independent Variables**	
		Wind Speed (m/s)	**Wind Blowing Direction (deg)**
Evaporation	1	5	270
	2	5	0
	3	5	90
	4	5	180
	5	8	270
	6	2	270
	7	12	270

3. Results and Discussion

Number The output of the model including evaporation rate and water level at three different points in the basin has been studied under different scenarios. The coordinates of these three points are specified as stations 1, 2, and 3 in Figure 3. Figure 4 shows the water level changes due to the change in wind direction. As can be seen, the change in wind direction did not have a significant effect on the change in water level, and for all directions, the water level decreased by more than two meters during the year. Figure 5 also shows the changes in evaporation rate per change of wind direction, and as we see in stations 1 and 2, there is no significant difference between changes in evaporation rate per change of wind direction, but in station 3 at the end of the one-year period there is little difference. It exists between different directions and has a higher evaporation rate per 180° wind angle.

As can be seen, the water level has decreased by approximately 2.2 meters during one year of the model running. Although this value is within the allowable range, it seems that the average speed of 5 m/s throughout the year causes maximum evaporation, which can be better judged by the results that are examined at different speeds. Note that the model of Kampf and Sadrinasab has an evaporation rate of 1.8 m/year that is larger than observations [17]. The rate of evaporation minus precipitation in the modeling study of Yao and Johns (from 1.2 to 1.43 m/year) [23].

In studies about the investigation of evaporation in water basins, as well as the equations that exist to calculate evaporation, only wind speed is considered and wind direction has no role. In the results of this section, the effects of wind direction change on evaporation are not observed and the reason is that the distinction between different wind directions is not included in the model evaporation calculations. However, physically, basins such as the Persian Gulf, which are limited to the mountainous areas in Iran from the north and to the desert areas in Saudi Arabia from the south, have different wind directions that transfer moist air masses to different areas. This can be accompanied by a change in relative humidity over the water basin.

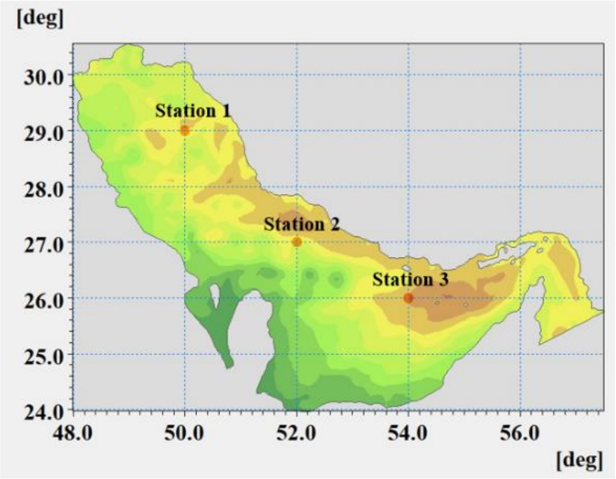

Figure 3. Location of Stations

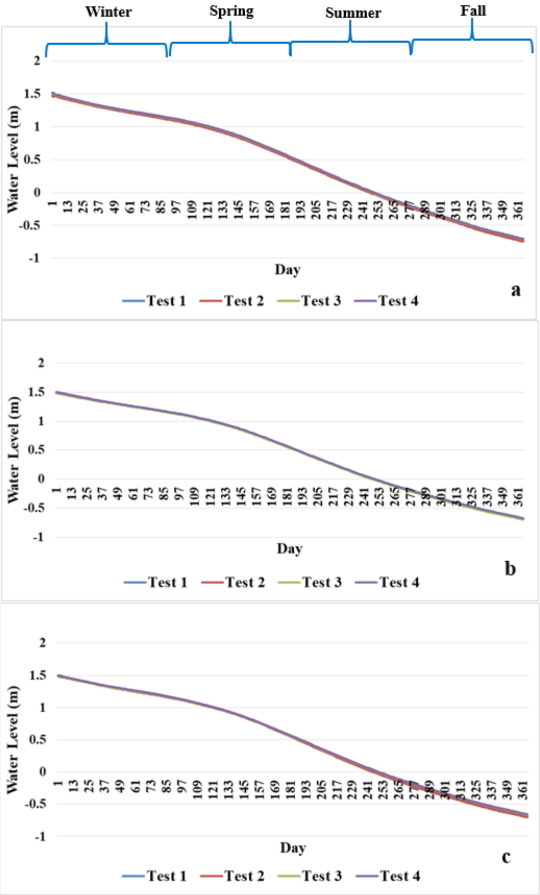

Figure 4. Water level changes due to the change in wind direction at (a) station 1, (b) station 2, (c) station 3

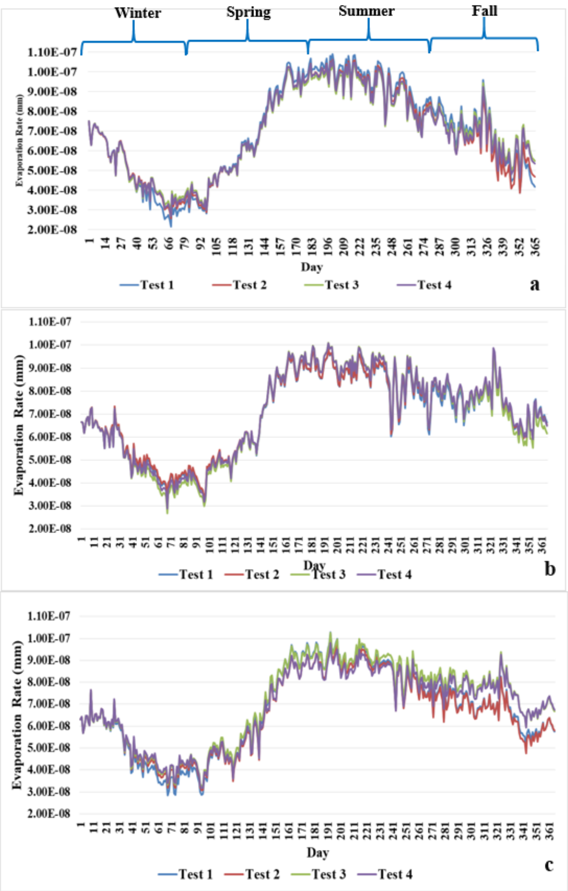

Figure 5. Evaporation rate changes due to the change in wind direction at (a) station 1, (b) station 2, (c) station 3

Figure 6 shows changes in water level due to changes in wind speed. Contrary to the wind direction, wind speed has a significant effect on water level, so that by increasing the wind speed from 2 to 12 m/s, the water level decreases by about 4 times. Figure 7 shows the changes in evaporation rate due to changes in wind speed, and it can be seen that in winter, when the surface water temperature is low, the change in wind speed has no significant effect on changes in evaporation rate, but in summer with increasing Water surface temperature, evaporation rate has increased significantly with increasing wind speed. Figure 8 also shows the surface temperature in winter and summer and shows that the temperature difference in most places is more than 10 degrees. the SST is as much a reflection of the surface flux as being a forcing of the flux in a shallow water system, the high-frequency variability of the SST must be resolved (using a coupled model) to be consistent with the response time scale of the local air–sea feedback process, otherwise systematic biases may occur [24].

Yu and Weller analyzed the trend relationship between latent evaporation and SST using the OAFlux products. They found that the linear trend patterns in the two variables are very similar, suggestive of the atmospheric response to oceanic forcing. Also they reinforced the notion that the relationship between evaporation, wind speed and humidity is nonlinear and that SST is a forcing for changes in evaporation [25]. In Figure 8, the nonlinearity of the evaporation rate with the wind speed can be seen well, and according to the temperature change due to the change of seasons, temperature increase can be considered as a stimulus to increase evaporation.

Yu examined the role of wind speed change in global changes in ocean evaporation. Using EOF analysis, he examined the yearly winter-mean time series of evaporation and related air-sea variables such as wind speed and humidity. The results showed the dominant role of wind force in evaporation and humidity. He hypothesized that the effect of wind on evaporation takes place in two ways. The first way is direct: the greater wind speed induces more evaporation by carrying water vapor away from the evaporating surface to allow the air–sea humidity gradients to be reestablished at a faster pace. The second way is indirect: the enhanced surface wind strengthens the wind-driven subtropical gyre, which in turn drives a greater heat transport by the western boundary currents, warms up SST along the paths of the currents and extensions, and causes more evaporation by enlarging the air–sea humidity gradients [26].

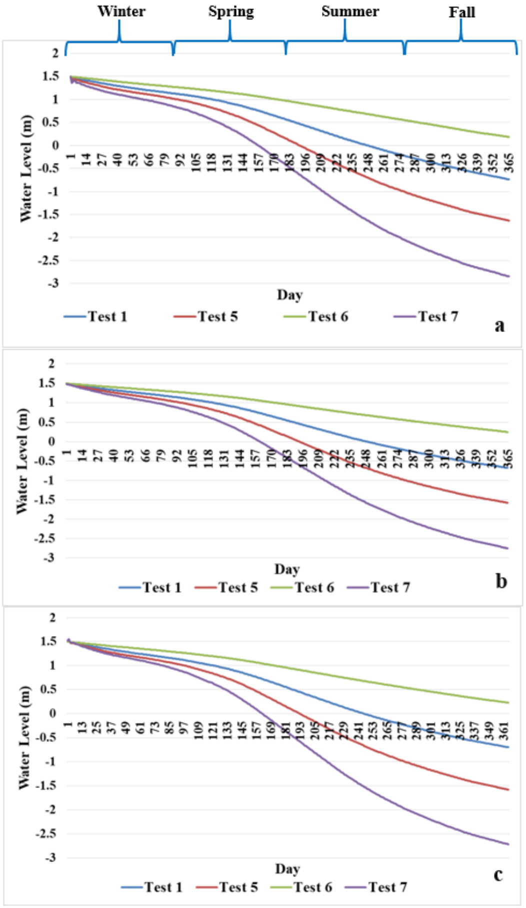

Figure 6. Water level changes due to the change in wind direction at (a) station 1, (b) station 2, (c) station 3

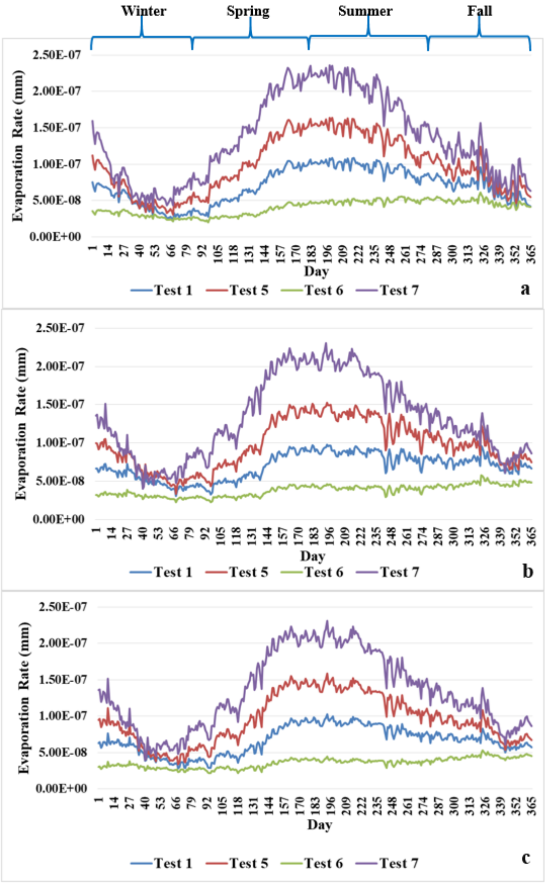

Figure 7. Evaporation rate changes due to the change in wind direction at (a) station 1, (b) station 2, (c) station 3

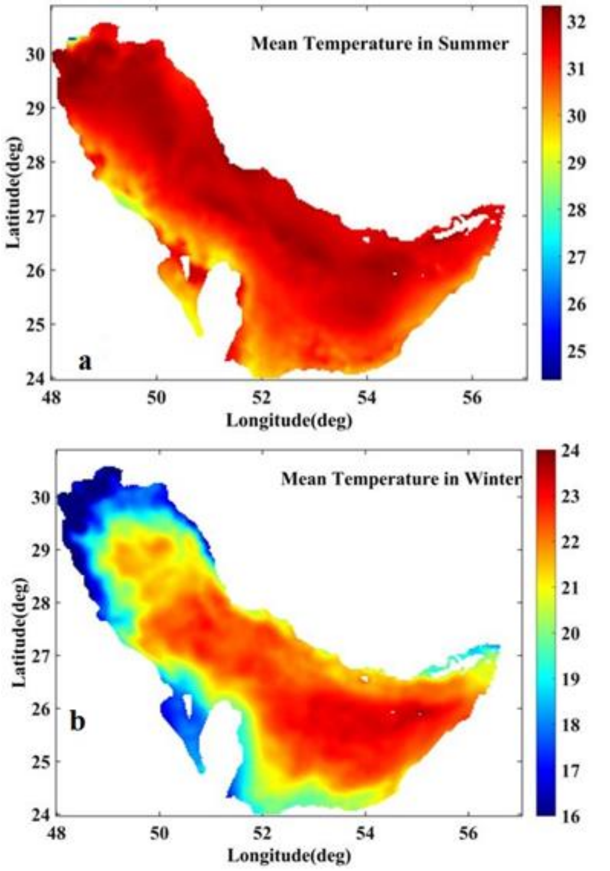

Figure 8. Sea surface temperature in (a) Summer, (b) Winter

4. Conclusions

Comparison of all figures shows that wind direction changes have no effect on evaporation rate and water level and its effects are very small; However, changes in wind speed have a great effect on evaporation rate and water level, especially in summer with increasing water temperature, increase in evaporation rate and the effect of wind speed is more, and this shows that changes in evaporation rate with wind speed are nonlinear. The decrease in water level also increases with increasing temperature and this parameter is also nonlinear and the higher the wind speed, the higher the rate of evaporation and decrease of water level.

Evaporation is one of the most important quantities in the maritime climate, and in the Persian Gulf, this parameter has made this basin one of the saltiest open waters in the world. Evaporation depends on factors such as air temperature, wind, relative humidity, cloud cover, etc. In this study, the effects of wind including wind speed and direction on evaporation rate during one year were investigated. The results showed that the wind direction has little effect on evaporation but wind speed has significant changes on evaporation rate and water level and these changes are nonlinearly related to water temperature so that in summer the evaporation rate grows faster with increasing temperature. Of course, perhaps the reason why the wind direction effects were not well defined is that the model only simulated marine parameters. To investigate the effect of wind direction, it is better to couple the oceanic model with a meteorological model and include a wider area including the areas around the Persian Gulf in the modelling basin. Past studies on evaporation rates have shown conflicting results from time to time; in other words, some researchers have found that evaporation rates are higher in summer and others in winter. However, in the study of Xue and Eltahir, the highest evaporation rate was obtained in November, although the summer average is higher than the winter [16].

5. References

1- Kohler, M.A., Nordenson, T.J. and Fox, W.E. (1955), *Evaporation from pans and lakes*, U.S. Dept. Commerce Res.p.38.

2- Guitjens, J.C., (1982), *Models of Alfalfa yield and evapotranspiration*, Journal of the Irrigation and Drainage Division, Proceedings of the American Society of Civil Engineers, 108(IR3), 212– 222.

3- Fritschen, L.J., (1966), *Energy balance method*, Proceedings, American Society of Agricultural Engineers Conference on Evapotranspiration and its role in Water Resources Management, December 5±6, Chicago, IL. St. Joseph, MI., 34-37.

4- Harbeck Jr, G.E., (1962), *A practical field technique for measuring reservoir evaporation utilizing mass-transfer theory*, U.S. Geol. Surv., Paper 272-E, 101–105.

5- Shuttleworth, W.J. and Wallace, J.S., (1984), *Evaporation from sparse crops Ð an energy combination theory*, Q. J. R. Meteorol. Soc., 111: 839-855.

6- Singh, V.P. and Xu, C.Y., (1997), *Evaluation and Generalization of 13 Equations for Determining Free Water Evaporation*, Hydrol. Processes, 11: 311–323.

7- Csanady, G.T., (2001), *Air-Sea Interaction Laws and Mechanisms*, University of Cambridge, United Kingdom, 239.

8- Emery, K.O., (1956), *Sediments and water of the Persian Gulf*, AAPG Bull., 40, 2354–2383.

9- Yao, F., 2008, *Water Mass Formation and Circulation in the Persian Gulf and Water Exchange with the Indian Ocean (PhD thesis)*, University of Miami. 162 p.

10- Rochford, D. J., (1964), *Salinity maxima in the upper 1000 meters of the north Indian Ocean*, Aust. J. Mar. Freshw. Res, 15, 1–24.

11- Wyrtki, K., (1973), *Physical oceanography of the Indian Ocean*, in The Biology of the Indian Ocean, vol. 3, pp. 18–36.

12- Bower, A.S., Hunt, H.D. and Price, J.F. (2000), *Character and dynamics of the Red Sea and Persian Gulf outflows*, J. Geophys. Res., 105, 6387–6414.

13- Prasad, T.G., Ikeda, M. and Kumar, S.P., (2001), *Seasonal spreading of the Persian Gulf Water mass in the Arabian Sea*, J. Geophys. Res., 106, 17,059–17,073.

14- Privett, D.W., (1959), *Monthly charts of evaporation from the North Indian Ocean, including* *the Red Sea and the Persian Gulf*, Q. J. R. Meteorol. Soc., 85, 424–428.

15- Hastenrath, S. and Lamb, P.J., (1979), *Climatic Atlas of the Indian Ocean*, Part I: Surface Climate and Atmospheric Circulation. University of Wisconsin Press.

16- Xue, P. and Eltahir. E.A.B., (2015), *Estimation of the Heat and Water Budgets of the Persian Gulf Using a Regional Climate Model*, American Meteorological Society, Volume 28, 5041-5062.

17- Kampf, J. and Sadrinasab, M., (2006), *The circulation of the Persian Gulf: A numerical study,* Ocean Sci., 2, 1–15.

18- Dabestani, M., MohammadMahdizadeh, M., Gheybi, A., Azizpour, J., (2018), *Investigation of Sea Surface Salinity in the Persian Gulf Using Data of MODIS and AMSU-B Sensors,* Hydrophysics, 23;4(1):95-104.

19- Azizpour, J., SiadatMousavi, S.M., Chegini, V., (2015), *Study of Physical Oceanographic Parameters in the Strait of Hormuz,* Hydrophysics, 1;1(1):15-24.

20- MIKE 21 & MIKE 3 FLOW MODEL FM, Hydrodynamic and Transport Module, Scientific Documentation, (2012)

21- Reynolds, R. M., (1993), *Physical oceanography of the Gulf, Strait of Hormuz, and the Gulf of Oman – Results from the Mt Mitchell expedition,* Mar. Pollution Bull., 27, 35–59.

22- Pous, S., Lazre, P., Carton, X., (2015), *A model of the general circulation in the Persian Gulf and in the Strait of Hormuz: Intraseasonal to interannual variability*, Continental Shelf Research, 94, 55–70.

23- Yao, F., Johns, W.E., (2010), *A HYCOM modeling study of the Persian Gulf. 2. Formation and export of Persian Gulf Water,* J. Geophys. Res. 115, C11018.

24- Xue, P., Eltahir, E.A.B, Malanotte-Rizzoli, P. and Wei, J., (2014), *Local feedback mechanisms of the shallow water region around the Maritime Continent*. J. Geophys. Res. Oceans, 119, 6933–6951.

25- Yu, L., Weller, R.A., (2007), *Objectively analyzed air–sea heat fluxes for the global ice-free oceans (1981–2005),* Bull. Amer. Meteor. Soc., 88, 527–539.

26- Yu, L., (2007), *Global Variations in Oceanic Evaporation (1958–2005): The Role of the Changing Wind Speed*, Journal of Climate, 20(21), 5376-5390.

INTERNATIONAL JOURNAL OF
COASTAL & OFFSHORE ENGINEERING

IJCOE Vol.6/No. 1/Winter 2021 (55-64)

Available online at: www. Ijcoe.org

Modeling of wind driven waves and estimation of wave energy in Chabahar Bay

Alireza Bahmanzadegan Jahromi[1], Mojtaba Ezam[2*], Kamran Lari[3], Abbas Ali Aliakbari Bidokhti[4]

[1] Ph. D. student, Marine Science Department, Science and Research Branch, Islamic Azad University, Tehran, Iran; ar.bahmanzadegan@gmail.com
[2]Assistance Professor, Marine Science Department, Science and Research Branch, Islamic Azad University, Tehran, Iran; ezam@srbiau.ac.ir*
[3] Associate Professor, Physical Oceanography Department, North Tehran Branch, Islamic Azad University, Tehran, Iran; k_lari@iau-tnb.ac.ir
[4] Full Professor, Institute of Geophysics, University of Tehran, Tehran, Iran; bidokhti@ut.ac.ir

ARTICLE INFO

Article History:
Received: 01 Jan. 2021
Accepted: 04 Apr. 2021

Keywords:
Chabahar Bay
MIKE21-SW model
Wave height
Wave energy

ABSTRACT

Sea waves are one of the main characteristics of water areas in the world, which are mainly produced by wind. Waves are the main boundary condition in the dynamic loading and hydraulic calculations of coastal structures. Numerical models are being developed to bring the sea and ocean conditions closer to the real conditions. In this research, the SW model from MIKE21 software is used to simulate wind waves in the Chabahar Bay and the energy extracted from these waves is estimated. The SW model simulates the growth, transmission and decay of wind waves in offshore and coastal areas. Chabahar Bay is a semi-closed and subtropical bay with an average depth of 7.5 m, which is located in the southeast of Iran. The model was implemented for a period of one year (2017) with a spatial resolution of maximum 5 km for offshore regions and less than 500 m in the interior parts of Chabahar Bay. ECMWF model wind data with a time step of 6 hours and a spatial resolution of 0.125 minutes were used. Comparison of model results for hourly averages with measured data shows a correlation coefficient of 0.84 for significant wave height. The annually average and maximum of wave height due to wind in the entrance of Chabahar Bay is 0.82 m and 2.19 m, respectively. The direction of the dominant waves is from south and the largest share of energy is related to waves with a period of around 11. The average of annual extractable power related to wind waves in the southern parts of Chabahar Bay was calculated from the order of 3 kW/m.

1. Introduction

Coastal areas are one of the most important national areas of Iran; A significant volume of various activities in various fields such as commercial, fisheries, oil, industrial, environmental, tourism, etc. activities are performed in these areas. Unfortunately, due to the lack of sufficient information and field data, achieving long-term goals has not been possible. In some cases, negative interactions in the hydrodynamic and geomorphological process of the region reduce the useful life of structures and ports. Waves are the most important factor in determining the geometric position and composition of beaches and also have a major impact on the design of ports, waterways and other coastal activities (Akbarifard et al., 2017). Sea waves are one of the main characteristics of water zones in the world, which are mainly produced by wind. Waves are the main boundary condition in the dynamic loading and hydraulic calculations of coastal structures (Nayebi et al., 2014). In coastal engineering applications and construction of coastal and offshore structures, wave height is the most important parameter in design (Esmaili and Kohnepushi, 2013). Over the past few decades, various methods and models, including experimental relationships and numerical models, have been developed to establish a direct or indirect relationship between wind speed and wave parameters. The use of mathematical formulas in numerical models increase the impact of wind to achieve more accurate results in wave modeling. Therefore, the impact of numerical models on wind is very important and also the study of the impact of models on wind is very important (Mohamad-Mehdizadeh and Hassan Tabar, 2017). Numerical models are being developed to bring sea and ocean conditions closer to real conditions. Among the various methods, numerical-spectral models can be named as the most complex and, of course, the most accurate methods for estimating the characteristics of wind waves. In this regard, various third generation numerical models such as SWAN (Boij et al., 2009), WAM (Group, 1988) and WaveWatch-III (Tolman, 2014), which are based on solving the equilibrium equation of the wave density spectrum, are presented (Dezvare Rasani et al., 2019). MIKE21 software is one of the most applied and accurate software in hydrodynamic studies. The MIKE21 software package is a third-generation model for simulating hydrodynamic processes. The solution of wave energy equations is based on the finite volume method on irregular triangular networking (Salehpour and Haji Valiei, 2015). This model considers phenomena such as wave breaking, refraction, energy loss in the breaking zone and the effects of bed depth changes (Tavakoli Oskooi and Hakimzadeh, 2016). The Sea of Oman and its shores, due to their connection to the open waters of the world, have been considered in the past and present, and its proximity to the Persian Gulf has increased its importance. Chabahar is one of the southeastern cities of Sistan and Baluchestan province and the only ocean port in the country, which is located on the coast of the Oman Sea and the Indian Ocean, and its berth is capable of mooring ocean-going ships. Chabahar Bay is the largest bay on the shores of the Oman Sea. This Bay is classified as omega bays in geology due to its omega (Ω) shape (Afsharian et al., 2010). Chabahar Bay is a semi-enclosed, subtropical bay (Fazeli and Zare, 2011). The average depth, area and volume of the Bay compared to the chart datum are 7.5 m, 290 km^2 and 2162×10^6 m^3, respectively. Its width at the entrance (east-west) is 13.5 km and its length (south-north) is 17.5 km (Biglari et al., 2015). The Bay is affected by monsoon conditions (Soltanpour and Dibajnia, 2015). Monsoon, meaning season, is a system of winds that blow over the ocean. Summer monsoon winds are much stronger than winter monsoon (Dehbandi et al., 2013). In the northern parts of the Indian Ocean, the prevailing winds are southwest during the months of May to September (summer monsoon) and during November to February, the winds often blow from the northeast (winter monsoon), March to April. And October winds are weak and are transitional months (Shankar et al., 2002).

The potential of the oceans has led many scientists and inventors to build devices that can convert wave, current, and tidal energy into other energies. Shirinmanesh and Chegini (2011) estimated the power extractable from the waves in Chabahar 3.9 kW using the Chabahar Buoy data and the Fourier analysis method. In another study, Saket et al. (2012) Used the SWAN model to model the wave in the Chabahar region and calculated the average annual wave power of just under 3 kW/m. The Ports and Maritime Organization, in line with its governance duty and in order to complete the maritime database and provide a way to solve many existing problems from the perspective of coastal engineering, including sedimentation and erosion in the coastal parts of the country, has defined a monitoring and modeling studies of iran coasts. In the first phase of this project, which covers the area of Chabahar Bay and about 100 km of coastline of Sistan and Baluchestan province, marine parameters during one year (2006-2007) by 7 waveguides and flowmeters and suspended sediment concentrations by 3 devices Turbidity was measured. Abbasi (2012) Using the wave modeling results, related to the Ports and Maritime Organization, the average annual wave height and power extractable from the waves at a point with a depth of 50 meters near Chabahar Bay has been calculated 0.88 m and 8.7 kW/m, respectively. In this research, using the MIKE21 numerical model, wind waves related to 2017 in the Chabahar Bay are estimated and after comparing the modeling results with field data, the energy extracted from the waves is calculated.

2. Materials and methods

2.1 Study area

Chabahar Bay is located in the south of Sistan and Baluchestan province and is considered a part of the Oman Sea. The Sea of Oman, or Gulf of Oman, connects the Arabian Sea in the northern Indian Ocean to the Persian Gulf via the Strait of Hormuz. The study area includes Chabahar and Pozm Bays (latitude 25.00-25.45 °N and longitude 60.00-61.00°E). The location of the study area, water depth in the model area, the position of the Chabahar buoy, the wave measuring device (ADCP) as well as the sampling stations are shown in Figure 1.

2.2 Model MIKE21-SW

The SW model from the MIKE21 simulates the growth, transmission and decay of wind waves in offshore and coastal zone. The basis of the SW model is the wave equilibrium equation in which the wave field is represented using the spectral density of the

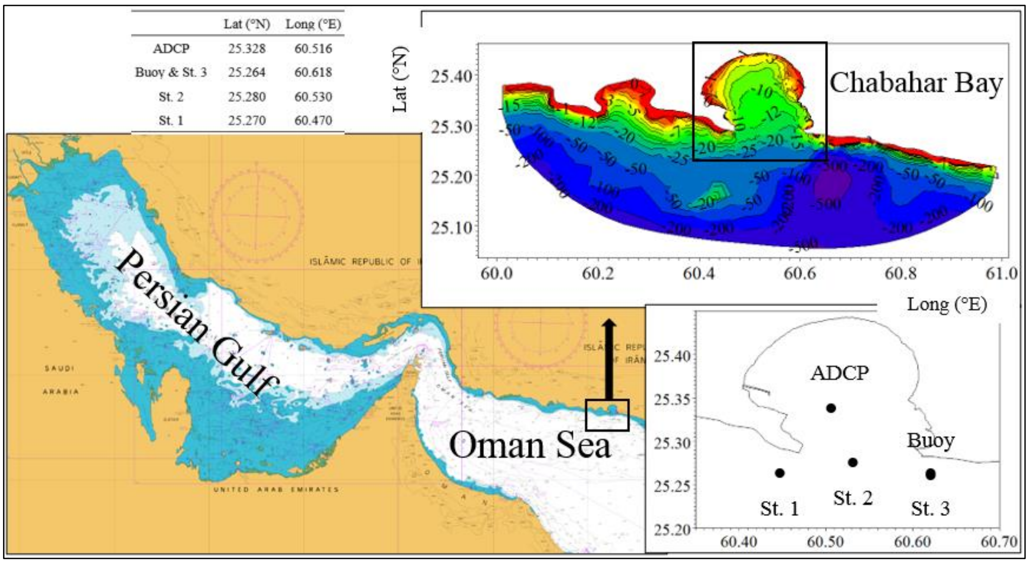

	Lat (°N)	Long (°E)
ADCP	25.328	60.516
Buoy & St. 3	25.264	60.618
St. 2	25.280	60.530
St. 1	25.270	60.470

Figure 1. Location of Chabahar Bay, modeling area, hydrography and studied stations

wave, $N = (\sigma, \theta)$ in which the angular frequency σ is a function of the frequency (f) and is defined as $\sigma=2\pi f$ and θ is direction for wave propagation. Also, the relationship between energy spectral density E and wave spectral density N is defined using the relationship $N=E/\sigma$ (DHI, 2009). In the SW model, there are two different types of formulations: 1- Parametric formulation with directional separation and 2- Full spectrum formulation. In cases where there is a need to simulate the growth, transmission and decay of wind waves in coastal and offshore areas, full spectrum formulation is used. In cases where only wave transmission is concerned and the spatial dimensions are less than 10-50 km, or in cases where the sea is fully developed in terms of wave growth rate, or in cases where swell waves or the combination of sea waves and swell waves are not important; Parametric formulation with directional separation can be used. The full spectrum formulation is based on the wave equilibrium equation proposed by Kamen et al. (1994) and Young (1999) (DHI, 2009). In the Mike 21 wave model, the evolution of the wave spectrum at position (x, y) and time t at the Cartesian coordinates is expressed by the spectral equilibrium equation (Abdollahzadeh et al., 2014):

$$\frac{\partial}{\partial t}N+\frac{\partial}{\partial x}C_xN+\frac{\partial}{\partial y}C_yN+\frac{\partial}{\partial \sigma}C_\sigma N+\frac{\partial}{\partial \theta}C_\theta N=\frac{S}{\sigma} \qquad (1)$$

The first expression to the left of the equation represents the local variation in the change in spectral density of the wave (N) over time; The second and third expressions show the propagation of N with velocities C_x and C_y in the direction x and y, respectively. The fourth expression shows the relative frequency transfer (with the propagation rate C_σ in the σ space) due to the change in depth and current. The fifth indicator represents the refraction due to depth and flow with velocity C_θ in the θ direction. The expression S on the right side of the equation, which represents energy sources; It includes various physical phenomena:

$$S=S_{in}+S_{wc}+S_{nl}+S_{bf}+S_{br} \qquad (2)$$

S_{in} represents wind energy, S_{wc} energy dissipation due to wave whitening, S_{nl} energy transfer due to nonlinear wave-wave interactions, S_{bf} is the loss due to bed friction and S_{br} is the loss due to wave failure due to depth change.

2.3 WAFO Toolbox

The definition of the wave energy spectrum $S(\omega)$ is:

$$\sigma^2 = \int_0^\infty S(\omega).d\omega \qquad (3)$$

Where σ^2 is variance of surface elevation and ω is angular frequency (Journee and Massie, 2001). In order to calculate the spectral density, WAFO software package was used. WAFO (Wave Analysis for Fatigue and oceanography) is a toolbox of MATLAB routines for statistical analysis and simulation of random waves and random loads (WAFO, 2011).

2.4 Used data

In order to determine the water depth, ETOPO1 data with a spatial resolution of 1 minute for the entire model range and hydrographic data of the Ports and Maritime Organization with a spatial accuracy of 100 meters for the interior parts of the Bay were used. ECMWF wind data for 2007, 2011 and 2017 with a spatial accuracy of 0.125 degrees and a time step of 6 hours were extracted for the model range and used as a surface force in the SW model. In order to validate the results of the model, Chabahar wave buoy data (2011 and 2017), ADCP measurement data (2007) belonging to the Ports and Maritime Organization were used. Also, the wind data of Chabahar synoptic station belonging to the Meteorological Organization were used to evaluate the wind speed; This data is collected in 3-hour time steps and is related to the years 2009 to 2017.

2.5 Model set up

First, a triangular grid with 3397 points and 6290 triangular elements was created in Mike software environment. In order to model the wind waves, full spectrum formulation was used; Also, ECMWF model wind data were extracted with a time step of 6 hours. The model was implemented for a period of one year (2017) with a spatial resolution of maximum 5 km for offshore areas and less than 500 m in the interior of Chabahar Bay. The refractive index $\gamma = 0.8$ and the bed hardness coefficient $k_n = 0.04$ were selected. In order to validate the model results, three data sets with the following specifications were used (Figure 2); It should be noted that all data used for validation is belong to the Ports and Maritime Organization which include: 1- ADCP data, these data are in the form of hourly averages of the significant wave height, which have been measured in the first phase of the monitoring and simulation studies of Iranian coasts; 2- Chabahar Buoy data for year 2007 and 3- Chabahar Buoy data for year 2011. The average of daily wave height for Chabahar Buoy extracted from the website of the Ports and Maritime Organization.

2.6 Error and accuracy of the model

In order to evaluate the results of the model, the statistical parameters of bias (BIAS), correlation coefficient (R), mean square error (RMSE) and scattering index (SI) according to the definitions of Shanas et al. (2014) were used; In these relationships, the values A_i are related to the model and the values B_i are related to ADCP or buoy.

$$\mathrm{BIAS}=\frac{1}{N}\sum_{l=1}^{N}(A_i-B_i) \tag{4}$$

$$R=\frac{\sum_{l=1}^{N}[(A_i-\bar{A})(B_i-\bar{B})]}{\sqrt{\sum_{l=1}^{N}[(A_i-\bar{A})^2(B_i-\bar{B})^2]}} \tag{5}$$

$$\mathrm{RMSE}=\sqrt{\frac{1}{N}\sum_{l=1}^{N}(A_i-B_i)^2} \tag{6}$$

$$\mathrm{SI}=\frac{\sqrt{\sum_{l=1}^{N}[(A_i-\bar{A})-(B_i-\bar{B})]^2}}{\bar{B}} \tag{7}$$

3. Results and discussion

The monthly average and maximum values of wind speed related to Chabahar synoptic station are presented in Table 1. The annual average of wind speed is 3.1 m/s. The maximum of observed wind speed is in November and February, which were 15 m/s and 14 m/s, respectively. The average monthly wind speed varies in the range of 2.7 m/s (in October) and 3.5 m/s (in July). Figure 2 (a) compares the hourly averages of the measured index wave height data for 2007 with the results of the SW model. The large correlation coefficient (0.84) and the small BIAS error (0.15) indicate that the model prediction for the significant wave height is within an acceptable range. On the other hand, it can be seen that the significant wave height for model usually has predicted the lower hand. In Figure 2 (b and c), the daily averages of the model results are compared with the Chabahar buoy data. The statistical parameters are within an acceptable range. BIAS and correlation coefficient have both decreased; The correlation coefficient of the model results with Buoy Chabahar data is slightly less than 0.70 (0.68 and 0.69). The square of the mean error did not change much in all three cases and ranged from 0.14 to 0.19. Dispersion index related to hourly data (0.12) was better than daily data (0.19 and 0.26).

Table 1. Mean and maximum monthly values of wind speed (m/s), Chabahar Synoptic Station (2009-2017)

	Jan	Feb	Mar	Apr	May	Jun	Jul	Aug	Sep	Oct	Nov	Dec
Ave.	2.9	3.2	3.2	3.1	3.0	3.2	3.5	3.4	3.1	2.7	2.8	2.8
Max.	10.0	10.0	14.0	13.0	9.0	12.0	12.0	8.0	9.0	7.0	15.0	12.0

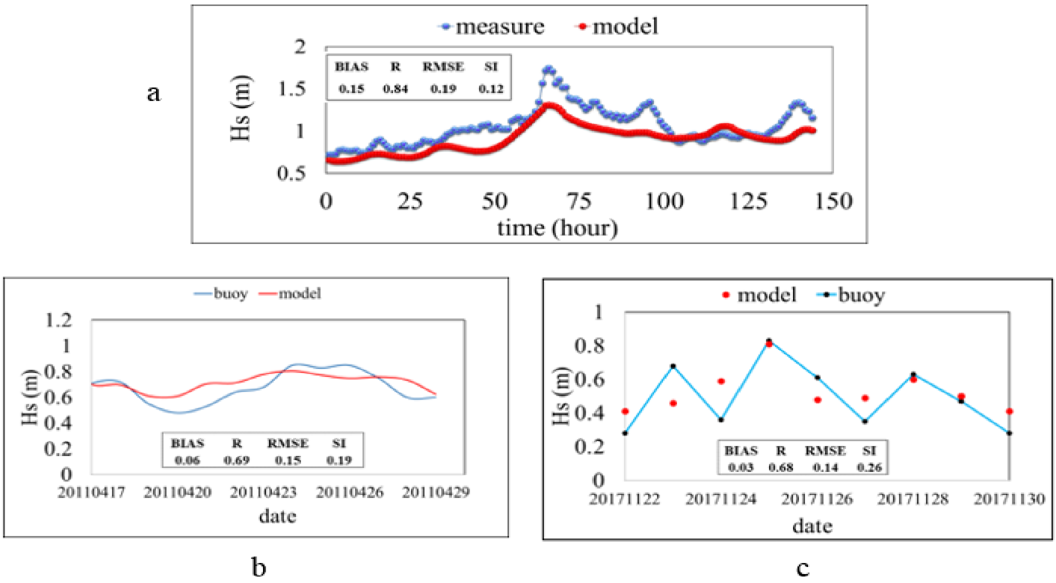

Figure 2. Validation of model results with data a) ADCP, related to 2007 and Chabahar wave buoy related to b) 2011 and c) 2017

The Chabahar wave buoy was active between 2012 and 2017, although there is a lot of missing data during this period; however, a considerable amount of data has been collected. The results related to the monthly averages of the wave height of the Chabahar Buoy in comparison with the monthly averages of Station No. 3 are shown in Figure 3. The results of the model and measured have almost the same annual trend. Thus, in spring, from April to June, the wave height increases and the maximum average wave height is seen in early summer (July). From July to November and December, the wave height decreased and at the beginning of winter, despite small changes, the wave height increased relatively. The highest values of model and buoy wave height occurred in July and are 1.32 and 1.57 meters, respectively. The results of the model are more different from the measured data related to buoy in spring and summer.

The monthly average of the significant wave height in the Chabahar Bay area is shown in Figure 4. In January and February, the significant wave height is often low (less than 0.5 m) and from January to February, slight changes are seen throughout the Bay. In March, the wave height at the entrance and in the middle of the Bay increased relatively. From March to July, the wave height increases in all parts of the Bay, and in July, all parts of the Bay experience maximum wave height. In May to August, the wave height at the mouth of the Bay is often more than 1 meter. From August to December, the trend of wave height changes is decreasing and in December, the lowest wave height is seen. The maximum wave height is related to the entrance of the Bay and the wave height decreases as it progresses into the Bay. The western parts of the Bay usually have lower wave heights than the eastern parts; the wave height in the western regions was usually less than 0.2 meters.

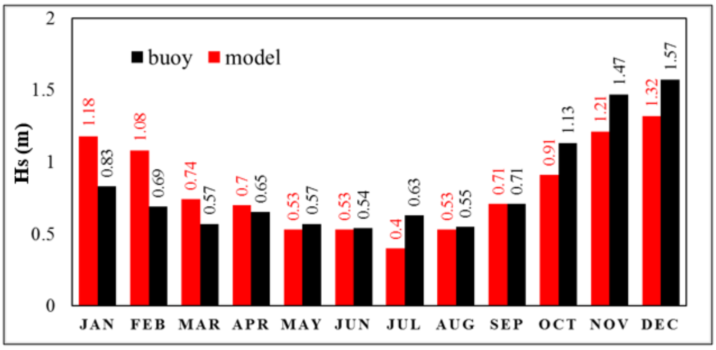

Figure 3. Comparison of monthly mean of significant wave height (m), Chabahar buoy data (black) (2014-2017) with model results (red) (2017)

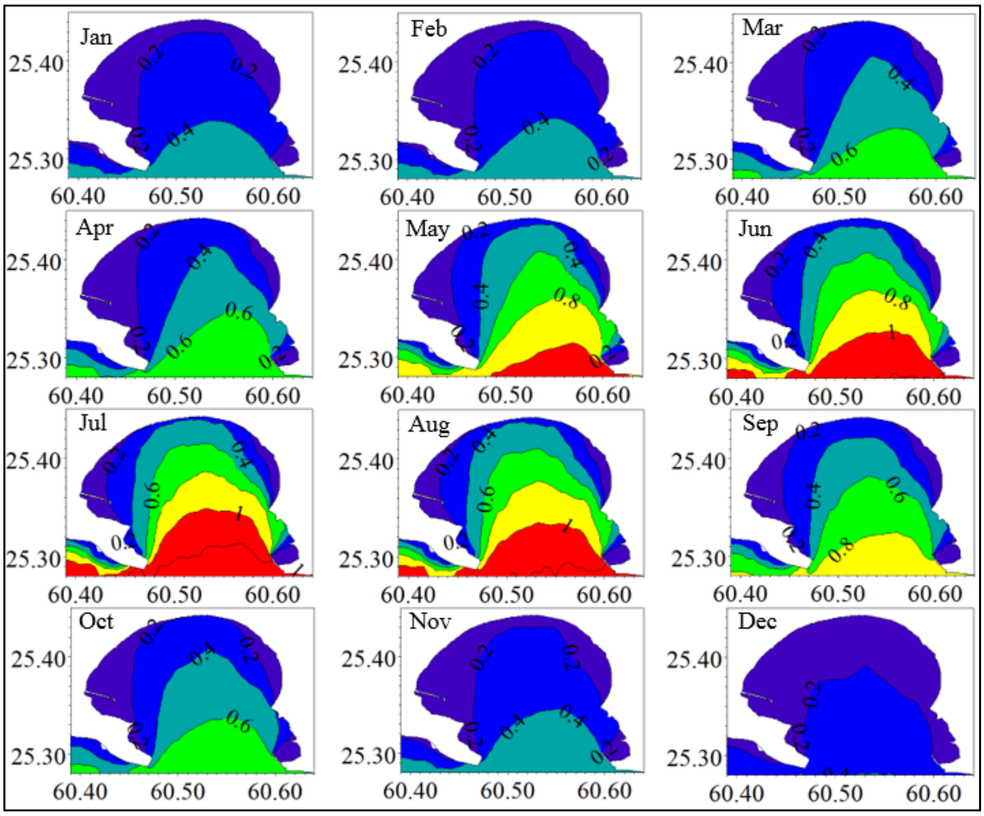

Figure 4. Monthly average pattern of significant wave height (m), MIKE21 model results, 2017

Wave rose corresponds to St. 2 with monthly average and maximum values at this station is shown in Figure 5. In all months except February, March and December there is the dominant southern wave. The predominant wave direction is southwest in February and March and southeast in December.

The frequency of waves with a wave height of more than 1.5 meters (yellow areas of wave rose) in February, May and July is higher than other months. Wave changes in autumn and winter are greater than in spring and summer, although the average of wave height in summer is higher than in other seasons; But the maximum wave height is seen in spring (April) (2.19 meters). Annual trend of wave height changes in three different stations St.1, St. 2 and St. 3 is shown in Figure 6.

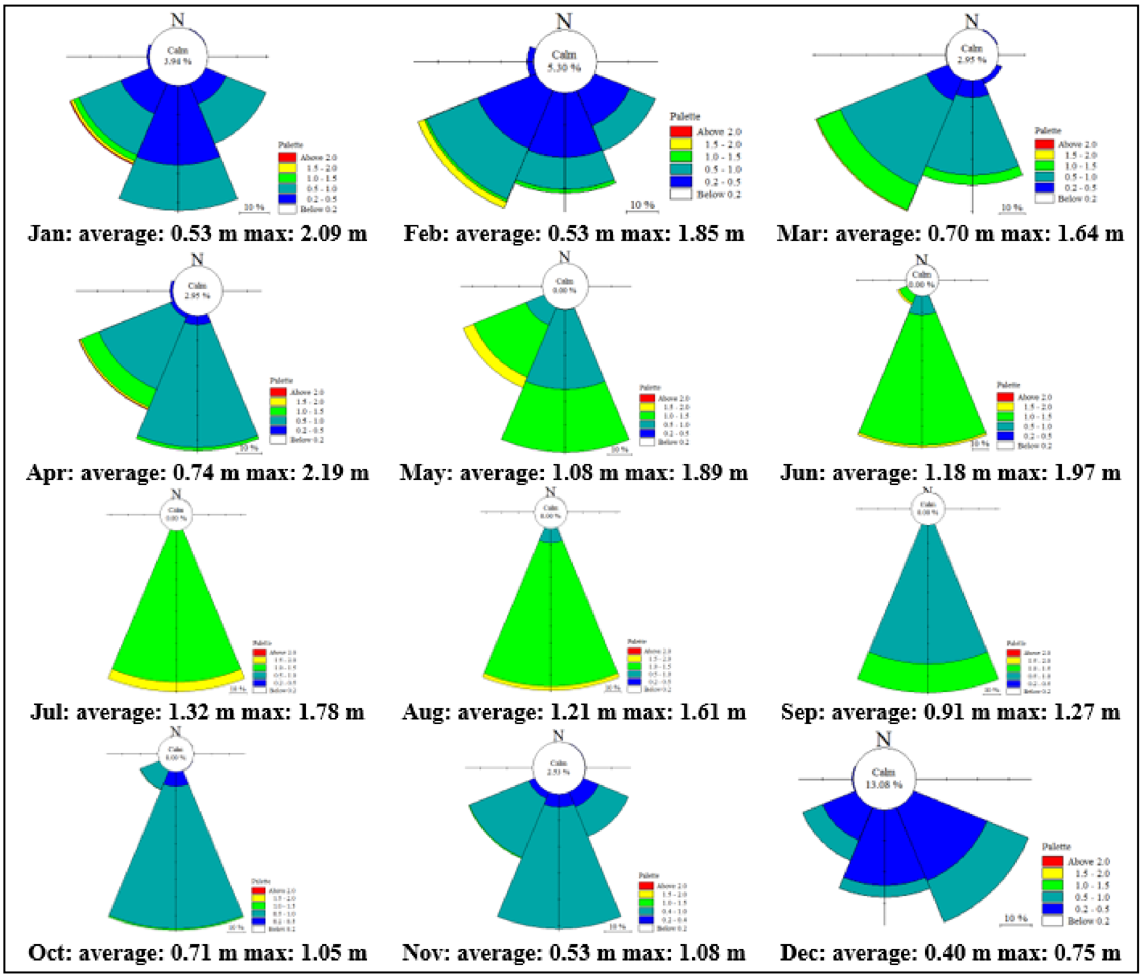

Jan: average: 0.53 m max: 2.09 m **Feb: average: 0.53 m max: 1.85 m** **Mar: average: 0.70 m max: 1.64 m**

Apr: average: 0.74 m max: 2.19 m **May: average: 1.08 m max: 1.89 m** **Jun: average: 1.18 m max: 1.97 m**

Jul: average: 1.32 m max: 1.78 m **Aug: average: 1.21 m max: 1.61 m** **Sep: average: 0.91 m max: 1.27 m**

Oct: average: 0.71 m max: 1.05 m **Nov: average: 0.53 m max: 1.08 m** **Dec: average: 0.40 m max: 0.75 m**

Figure 5. Monthly wave rose related to St. 2 (2017)

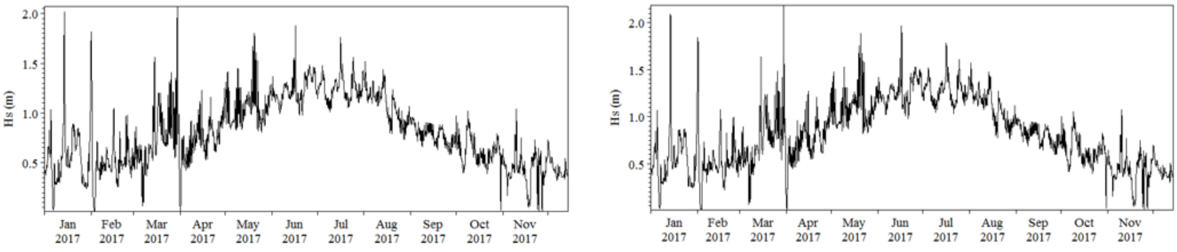

St. 1: max: 2.07 m average: 0.81 m **St. 2: max: 2.19 m average: 0.82 m**

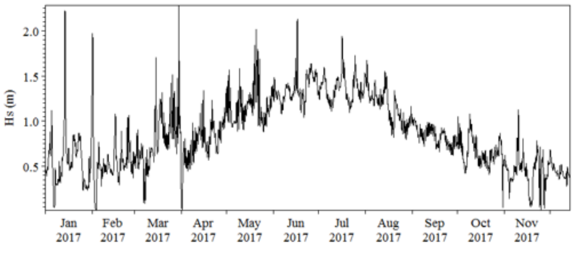

St. 3: max: 2.28 m average: 0.87 m

Figure 6. Annual changes in the significant wave height at three stations St. 1, St. 2 and St. 3

The maximum wave height usually occurs in winter and the first three months of the year, in other words, in winter, despite the fact that the monthly and seasonal average of wave height is lower, but we see the maximum wave height in this season. The maximum wave height of the East Station (St. 3) is 2.28 meters. The average of annual wave height increases from west to east; In general, the wave height in the eastern regions is higher than the western regions. As we expect from the wave height results, the wave power increases from west to east (Figure 7). The maximum of wave energy is related to the eastern station (St. 3) and is equal to 18.5 kW/m. The average wave energy at this station is 3.1 kW/m. The annual direction of the dominant wave is from south (Figure 8) and the dominant waves have a wave period between 4 to 8 seconds and often have a wave height of more than 0.5 meters. The maximum power extractable from the waves is also from south and in 90% of cases the extractable energy is more than 0.5 kW/m. Monthly spectral density (Figure 9) shows that in most months of the year, the highest energy is related to waves with a period of less than 30 seconds (often around 10 seconds). In March and September, the highest share of energy is related to storm waves (long period waves). In some months (April, May, June and December), the energy spectrum shows two peaks with different intensities. One of these peaks is related to ordinary winds, which usually produce waves with a period of less than 30 seconds (smaller peak), and the other is related to storm waves, which often produce waves with a period of more than 30 seconds.

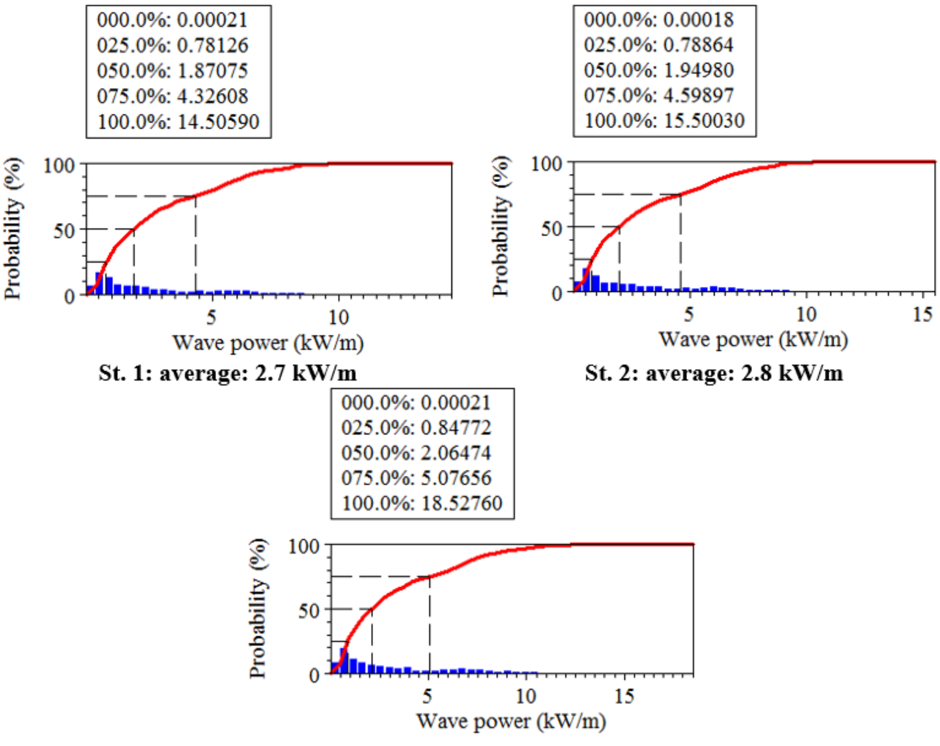

St. 1: average: 2.7 kW/m

St. 2: average: 2.8 kW/m

St. 3: average: 3.1 kW/m

Figure 7. Distribution of wave power probability in different parts of the inlet of the Chabahar Gulf, with mean values (P50%), average and maximum (P100%)

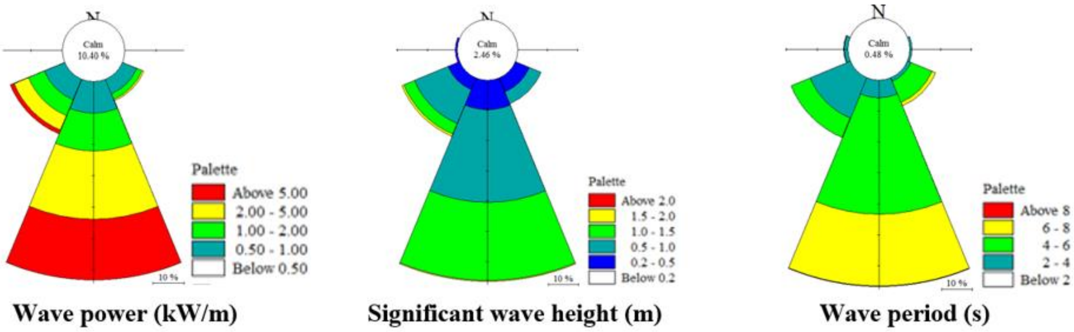

Figure 8. Annual Directional Distribution of wave Period, significant wave height and Wave Power (St. 3_ year 2017)

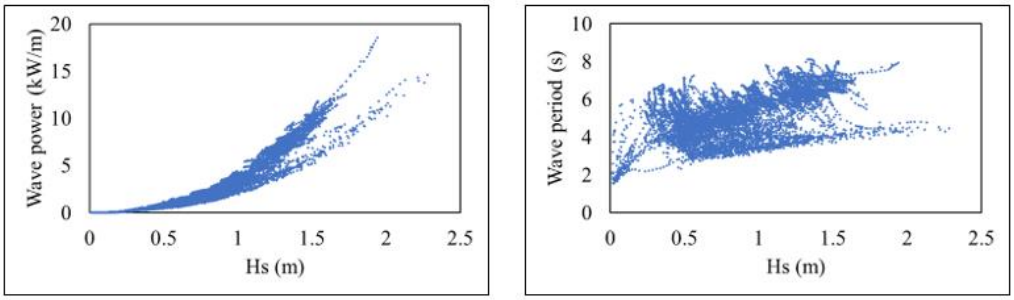

a

b

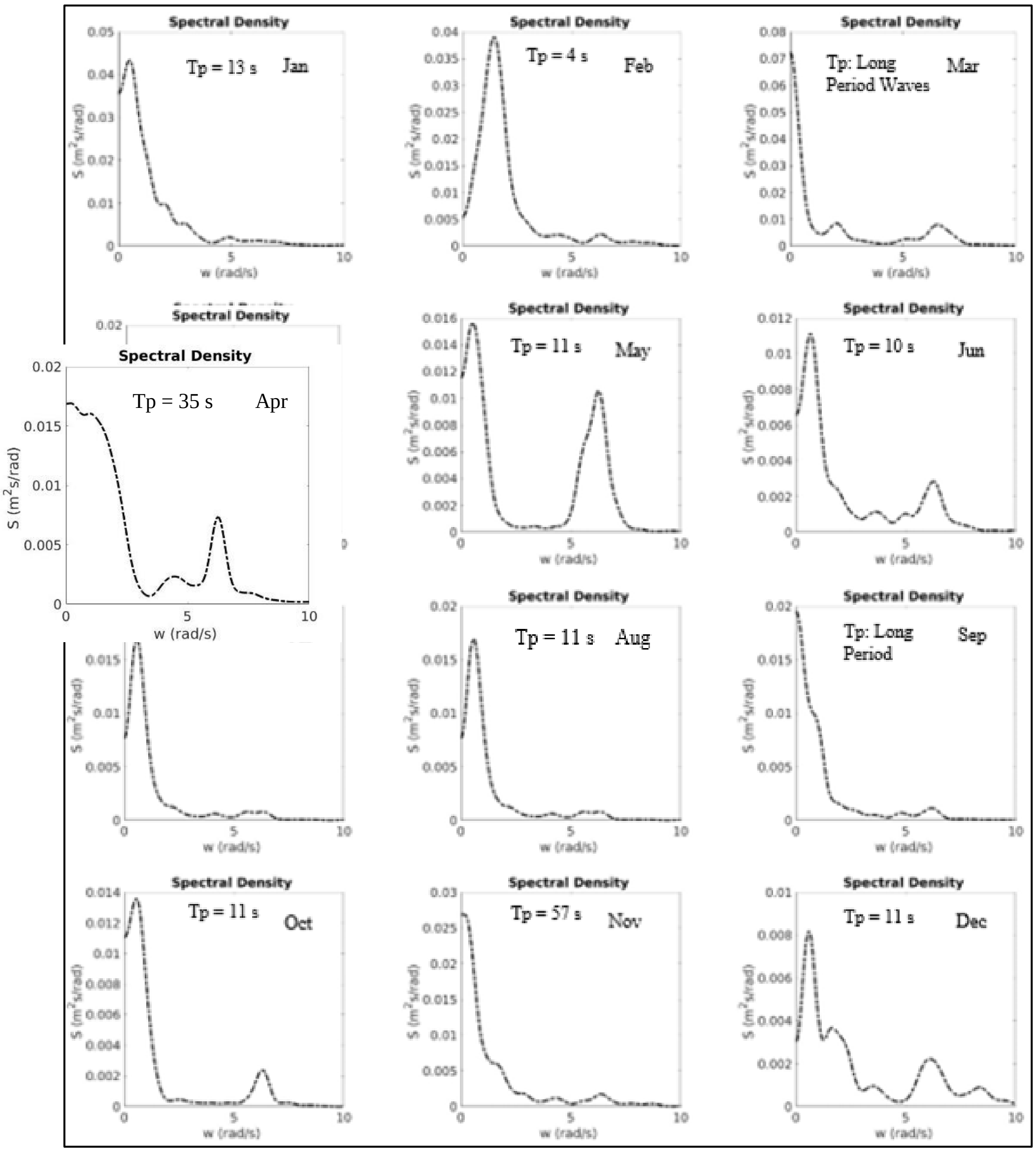

Figure 9. Monthly spectral density (m^{2}s/rad) versus angular frequency (rad/s), related to St. 2

4. Conclusion

The prediction of the wave height resulting from the SW model was acceptable in comparison with the measured data and the correlation coefficient was calculated between 0.69 (for daily averages) to 0.84 (for hourly averages). Chabahar Synoptic Station recorded an average wind speed of 3.1 m/s in the period 2009-2017. Examination of monthly average values of model results and Chabahar Buoy data shows that the wave height has an annual trend, so that during the spring months and with the arrival of summer, the wave height increases and the maximum wave height at the beginning of summer is observed with the intensification of summer monsoon winds. From mid-summer and with the decrease of monsoon winds, the wave height decreases and the lowest values of wave height are related to the end of autumn. In winter, the wave height was relatively low, but in late winter, we see an increase in wave height. The highest wave height occurs at the entrance of the Bay and decreases as it advances to the interior of the Bay. The annual average and maximum of wave height due to wind in the entrance of Chabahar Bay is 0.82 m and 2.19 m, respectively. From west to east the significant wave height increases. The direction of the dominant wave is from south and the period of the dominant waves changes in the range of 4-8 seconds. The average of annual extractable power in the southern parts of Chabahar Bay was calculated from the order of 3 kW/m. Compared to the data of Chabahar buoy which belongs to the Ports and Maritime Organization and on the one hand covers a limited time-space period and on the other hand has a lot of missing data as well as other statistical methods (dependent on Field data, such as Shirinmanesh and Chegini, 2011); Using the MIKE21 numerical model and applying the minimum wind and wave data at the borders, acceptable results were obtained for a full one-year period (2017) in the entire Chabahar Bay area.

5. References

1- Akbarifard, S., Zarei, H., and Zalqi, A., (2017), *Hourly and daily forecast of wave height in Chabahar region,* Ecology Quarterly, Volume 4, Number 4, pp. 1140-1129.

2- Nayebi, R., Bakhtiari, M., Sadri-Nasab, M., Shahni-Karamzadeh, N., (2014), *Investigation of wind wave changes with the help of MIKE21 software,* Bi-Quarterly Journal of Water Science and Engineering, Islamic Azad University, Ahvaz Branch, Fourth Year, No. 10, pp. 49-37.

3- Esmaili, M., A. Kohnepushi, (2013), *Determining the parameters of sea waves in Chabahar region,* The first national conference on the development of Makran beaches and maritime authority of the Islamic Republic of Iran.

4- Mohamad-Mehdizadeh, M., Hassan Tabar, S. H., (2017), *The Impact of MIKE21 and SWAN Models on Wind Changes in Wave Characteristics Simulation in the South Caspian Region,* Iranian journal of marine technology, Imam Khomeini University of Marine Sciences, Noshahr, Volume 4, Number 1, pp. 85-75.

5- Boij, N., Haagsma, I., Hothuijsen, L., Kieftenburg, A., Ris, R., Van der Westhuysen, A., Zijlema, M., (2009), *User Manual of SWAN,* Version 40.72, Delft University of Technology.

6- Group, T.W., (1988), *The WAM model—A third generation ocean wave prediction model,* Journal of Physical Oceanography, V. 18, Issue 12, pp.1775-1810.

7- Tolman, H. L., (2014), *User manual and system documentation of WAVEWATCH III,* Environmental Modeling Center Marine Modeling and Analysis Branch, Technical Note, p. 311.

8- Dezvare Rasani,R., Mohammadi Kale Sar, P., Haji Tabar, M., (2019), *Determination of wind wave characteristics using Wave Watch-III numerical model and comparison of its results with Mike21-SW model,* Journal of Marine Science and Technology, V. 18, N. 2.

9- Salehpour, A., Haji Valiei, F., (2015), *Numerical Simulation of Sediment Transfer Pattern in the East Coast of Rigo Port,* 17th Marine Industries Conference.

10- Tavakoli Oskooi, M., Hakimzadeh, H., (2016), *Numerical simulation of Anzali port waves using MIKE21 numerical model before and after the development of breakwaters,* 20th Marine Industry Conference.

11-Afsharian, S., M. Sadri-Nasab, Chegini, V., A. Ashtari Larki, (2010), *3D modeling of water circulation in Chabahar Bay,* M.Sc. Thesis, Khorramshahr University of Marine Sciences and Technology.

12- Fazeli, N., Zare, R., (2011), *Effect of seasonal monsoons on calanoid copepod in Chabahar bay-Gulf of Oman,* Jordan Journal of Biological Sciences, V. 4, pp. 55-62.

13- Biglari, M., Valipour, M. S., Rahmany, H., (2015), *Technical Feasibility Study of Energy Generation from the Tide in Southern Coasts of Iran Using Helical Turbines,* Journal of Applied Environmental and Biological Sciences, V. 5, pp. 39-48.

14- Soltanpour, M., Dibajnia, M., (2015), *Field measurements and 3D numerical modeling of hydrodynamics in Chabahar Bay,* International journal of maritime technology, V. 3, pp. 49-60.

15- Dehbandi, A., Akbari-Beidakhti, A., Ezam, M., Torabi-Azad, M., (2013), *Study of Surface Flow Patterns in the North Indian Ocean during the Monsoon Seasons,* Master Thesis, Islamic Azad University, Science and Research Branch, Tehran.

16- Shankar, D., Vinayachandran, P. N., Unnikrishnan, A. S., (2002), *The monsoon currents in the north Indian Ocean,* Progress in oceanography, V. 52, pp. 63-120.

17- Shirinmanesh, S., Chegini, V., (2011), *Study and evaluation of extractable energy estimation from tidal wave and current in Chabahar Bay,* Journal of Marine Science and Technology, Volume 10, Number 2, pp. 107-97.

18- Saket, A., Etemad-Shahirdi, A., (2012), *Wave energy potential along the northern coasts of the Gulf of Oman,* Iran, Renewable Energy, V. 40, Issue 1, pp. 90-97.

19- Abbasi, G., (2012), *Investigation and Feasibility Study of Wave Power Extraction in Northern and Southern Waters of Iran,* 10th International Conference on Coasts, Ports and Marine Structures (ICOPMAS).

20- DHI, (2009), *MIKE 21 Spectral Waves FM Module,* User Guide. DHI, Denmark, 116 p.

21- Komen, G. J., Janssen, P.A.E.M., Makin, V., Mastenbroek, K., Oost, W., (1994), *Review: On the sea state dependence of the Charnock parameter,* Journal of Glob Atmos. Ocean System, V. 5, pp. 367-388.

22-Young, I. R., (1999), *Wind Generated ocean waves,* V. 2, 1st edition, 287 p.

23- Abdollahzadeh, Y., Erdik, T., Özger, M., Altunkaynak, A., (2014), *Application of MIKE 21 SW for wave hindcasting in Marmara Sea Basin for the year 2012,* 11th International Congress on Advances in Civil Engineering- ACE 2014.

24- Journee, J., Massie, W., (2001), *Offshore Hydromechanics,* 1st Ed, Delf University of Technology, p. 570.

25- WAFO group, (2011), *A MATLAB Toolbox for Analysis of random waves and loads,* Lund University, p. 185.

26- Shanas, P.R., SanilKumar, V., Hithin, N. K., (2014), *Comparison of gridded multi-mission and along-track mono-mission satellite altimetry wave heights with in situ near-shore buoy data,* Ocean Engineering, V. 84, pp. 24-35.